Development of remote sensing of hydro-environmental attributes using airborne topo-bathymetric LiDAR and their application to hydraulic modeling for river management tasks

2022, September

Md. Touhidul Islam

Graduate School of Environmental and Life Science

(Doctor's Course)

OKAYAMA UNIVERSITY, JAPAN

Development of remote sensing of hydro-environmental attributes using airborne topo-bathymetric LiDAR and their application to hydraulic modeling for river management tasks

A Thesis

Submitted to Graduate School of Environmental and Life Science

Okayama University

In partial fulfillment of the requirement for the degree of

Doctor of Philosophy

Submitted by

Md. Touhidul Islam

Department of Urban Environment Development

Graduate School of Environmental and Life Science

Okayama University, Japan

2022, September

CONTENTS		PAGES

List of Figures

List of Figures (Cont.)

List of Figures (Cont.)

List of Figures (Cont.)

List of Figures (Cont.)

List of Figures (Cont.)

List of Figures (Cont.)

List of Tables

List of Tables (Cont.)

CHAPTER 1

General Introduction

1.1 Remote sensing of riverine environments

Appraising riverine environments, including topo-bathymetric, on-site streamflow, and discharge measurements of stream channels and floodplains, along with their vegetation distribution assessment, is challenging and expensive. Nevertheless, such appraisal is crucially important for proper river channel design and management measures (e.g., Yoshida et al., 2020a), including riparian ecosystems management tasks (e.g., Toda et al., 2005). The importance of gathering this basic information is growing by the day due to recent climate change (Schiermeier, 2011), causing more devastating extreme flood occurrences than predicted. Manually obtaining information related to riverine hydro-environmental attributes is often challenging, time-consuming and restricted by safety concerns. However, as a result of rapid technological advancements, various sophisticated remotely sensed techniques have been demonstrated to overcome such challenges that can hinder traditional river engineering research methods. Although several new remote sensing technologies have been demonstrated over the last few decades, they are still in various stages of development, rely on different computational platforms, and each has unique benefits and challenges. Therefore, their applicability must be validated and improved in light of the uncertainties associated with varying field conditions. The following sections describe the promises and uncertainties of remote sensing technologies in comparison to traditional approaches in riverine studies, particularly for topo-bathymetric, hydraulic quantity, and vegetation attribute assessment.

1.1.1 Topo-bathymetric assessment

High-resolution topo-bathymetric data of both exposed and submerged areas is critical for a wide range of practical applications in river research, management, and rehabilitation, including flow and sediment transport, hydrogeomorphic processes, flood flow modeling, aquatic habitat assessment, and so on. It is also essential to identify the places of disaster risk in the river channel, including the current situation of the submerged artificial infrastructures, which are becoming increasingly important because of their roles to drain heavy rain or flood water safely. However, due to the difficulty of conducting reliable surveys in a variety of fields with extreme situations (e.g., flood-affected areas) or regions that are difficult for researchers to access (e.g., vegetated floodplains), field data are scarce or, if available, are frequently inaccurate or incomplete. Particularly in Japan, after larger-scale flooding events, manual surveys of cross-sectional bed elevations and visual inspections have been conducted at 200 m intervals along the longitudinal direction (Mano et al., 2020). Such traditional in situ surveys necessitate a high level of engineering expertise to identify disaster risk locations between survey lines and suitably digitize via acquiring river shapes and circumstances. To overcome those constraints in traditional methods, remote sensing techniques with potential, including image-based approaches (e.g., Westaway et al., 2020), airborne LiDAR bathymetry (ALB; e.g., Kinzel et al., 2007; Yoshida et al., 2020a), unmanned aerial vehicle (UAV)-integrated LiDAR (e.g., Islam et al., 2022; Kinzel et al., 2021; Mandlburger et al., 2020), and others are commonly used to demonstrate river terrain with emphasis on submerged areas. Because water transparency, riverbed conditions, and bottom reflectivity can all restrict bathymetric LiDAR measurements (e.g., Kinzel et al., 2021), the performance of the emerging remotely sensed techniques must be examined carefully in light of their shortcomings.

1.1.2 Sensing of hydraulic quantities

In addition to assessing topo-bathymetric attributes, obtaining information related to stream velocity and discharge is important because it can have an impact on the surrounding environment, floodplains, riverine habitats, sedimentation, river construction tasks, human needs (agriculture, ecotourism, etc.), and others. A reliable record of such hydraulic quantities, particularly during extreme flooding, can serve as input and validation data for hydrodynamic modeling (Yoshida et al., 2020a). Traditionally, the streamflow rates in Japanese flooded rivers have been gauged by dropping several floats from a bridge. Because of its cost-effectiveness and feasibility, this conventional method has been widely adopted throughout the country. However, the measurement's accuracy becomes questionable when the floats are confined by locally produced vortices and tend to meander near river banks while passing through the sampling sections. Furthermore, conducting fieldwork with many personnel becomes dangerous in extreme weather conditions such as heavy rain and strong winds during rainy seasons and typhoons. Consequently, the conventional method may provide limited information during a significant flood, resulting in uncertain rating curves. Although sophisticated two-dimensional (2-D) or three-dimensional (3-D) flow measurement approaches, such as the Acoustic Doppler Current Profiler (ADCP) (Gordon, 1989), have evolved over the last few decades for simultaneous acquisition of water velocity and depth in wide rivers (Mueller et al., 2013), these technologies cannot always be used economically. Moreover, they are difficult to operate in severe flood conditions.

Given those circumstances, designing remote-sensing-based methodologies for on-site streamflow assessment can lower risks to hydrographers during natural hazards,

economize current streamflow platforms, and broaden networks into ungagged river systems, including remote catchments that are difficult to reach. To elucidate such practical river engineering issues, many academic, public, and commercial entities are launching several remotely sensed analyses using various sensors and platforms: ground-based techniques (e.g., Fujita et al., 2019), aerial vehicles that are crewed (e.g., Barker, 2018) and uncrewed (e.g., Tauro et al., 2016), and satellites (e.g., Bjerklie et al., 2018). These rapidly evolving sets of approaches are expected to be used in applied research in river channel planning and disaster mitigation measures, with great promises. Although several new sensors and algorithms have been proposed, image-based techniques at the hydraulic research level are still in their early stages. More recently, Fujita et al. (2020) proposed commercial software to estimate surface flow velocity along a specific cross-section: artificial intelligence (AI)-automated Hydro- space–time image velocimetry (Hydro-STIV). The technique's main benefit is that it uses moving images captured by the UAV platform in addition to fixed camera images. Furthermore, unlike other image-based methods (e.g., Large Scale Particle Image Velocimetry, Particle Tracking Velocimetry, and so on), the current approach requires no visual tracking of tracers (i.e., floats) on superimposed images. Earlier studies (Fujita et al., 2019; Yoshida et al., 2020b) reasonably validated the conventional STIV (KU-STIV) technique's accuracy using images taken by fixed station cameras. Then the studies compared results to ground-truth observation and traditional ADCP, which gave few erroneous results and little need for manual parameter adjustment. Consequently, as with other imaging systems, when verifying the recently updated STIV technique's applicability to examine on-site streamflow features under varying field conditions, one must particularly consider its uncertainties. Therefore, in this study, I evaluated the promises and drawbacks of

the AI-based STIV approach to the remote analysis of hydraulic quantities under varying field conditions.

1.1.3 Vegetation attributes assessment

With topo-bathymetric and hydraulic information, riparian vegetation attributes are crucially important to developing balanced river management measures, addressing issues such as flood control (Yoshida et al., 2021) and ecosystem management (e.g., Toda et al., 2005). When confronted with environmental system challenges, researchers can benefit from understanding the specific distribution of vegetation, including but not limited to location, quantity, and species. In recent years, researchers have become increasingly interested in changes in the numbers of original dominant species as a result of exotic species invasion (Mooney & Cleland, 2001). In this regard, field inspections have primarily been conducted on limited river sections, requiring personnel to enter the site to conduct measurements with a total station or a real-time dynamic global positioning system. These ground-truth surveys are daunted by several limitations: they are expensive, time-consuming, and non-repeatable. Furthermore, field surveys may encounter extreme situations (e.g., flood-affected areas) that can endanger the investigators, as well as areas that are difficult for the researchers to access (e.g., densely vegetated areas), resulting in ineffective data collection (Anjum and Tanaka, 2020). Nevertheless, it is essential to clarify their distributions to predict and control the flooded river flows, as vegetation is prone to reducing flow capacity during floods, which significantly impacts river management.

To address these shortcomings in assessing vegetation distributions over long river reaches at the reach scale, several leading researchers have demonstrated advanced and effective remote sensing techniques, specifically synthetic aperture radar images

(Mason et al., 2003), airborne laser scanning (Forzieri et al., 2011; Straatsma & Baptist, 2008), airborne LiDAR topo-bathymetry (ALB) (Mandlburger et al., 2015; Wieser et al., 2016; Yoshida et al., 2020a), and others. However, because of non-uniform point cloud density and low-resolution aerial images remotely captured from airborne platforms, most researchers find it difficult to extract detailed features for accurate land cover mapping (e.g., Yoshida et al., 2020a). Consequently, to achieve the ultimate targets in fluvial research (e.g., flood control and ecosystem management), river engineers have recently been drawn to UAV-borne topo-bathymetric LiDARs (Kinzel et al., 2021; Mandlburger et al., 2016) and a novel UAV-based GLS (TDOT GREEN, 2020) with higher and more uniform point density. Despite advancements in remote sensing technologies, more research is required to address their benefits and challenges in varying field conditions.

1.2 Flood flow modeling for vegetated rivers

Water is crucially important for sustaining life, but it is also the root cause of numerous disasters. In recent years, extreme and even record-breaking flood events induced by intensive rainfall, exacerbated by global warming phenomena, have increasingly endangered human lives worldwide (Schiermeier, 2011). For instance, European floods, although they had not been seen in decades, occurred in mid-July 2021 as the latest sign of climate change. Several news outlets reported that at least 188 people had died in a catastrophic flood that inundated parts of Germany, Belgium, and the Netherlands. A flood inundated central China, largely Henan province, in mid-July 2021, following torrential rains that precipitated an average year's moisture in just three days: the most since record-keeping began 60 years ago. In fact, China has remained on high alert since devastating floods struck the region in 2020 (Wei et al., 2020), with regular flood-response and rescue drills. Furthermore, particularly

in Japan, heavy rain frequency has intensified following recent climate change, with heavier than expected flooding occurring each year during the last decade (Ministry of the Environment et al., 2018). For instance, during July 5–7 in 2018, a severe rainfall event occurred in western Japan, causing intense flooding and sediment disasters in many places, especially in Okayama, Hiroshima, and Ehime Prefectures. In Okayama Prefecture, devastating floods occurring in several rivers inundated residential areas (Yoshida et al., 2021). According to field observations after flooding, most rivers were damaged severely. Table 1.1 presents the rivers damaged in Okayama Prefecture during the 2018 rainfall event.

Table 1.1 Damaged rivers in Okayama Prefecture during 2018 flooding

River name	River basin	Major river damage type*	Management authority
Takahashi River	Takahashi River	B and C	National Gov.
Takahashi River		A	Okayama Pref.
Oda River		A and B	National Gov.
Oda River		A	Okayama Pref.
Nariwa River		A	Okayama Pref.
Matani River		A	Okayama Pref.
Takama River		A	Okayama Pref.
Suemasa River		A	Okayama Pref.
Osaka River		A and C	Okayama Pref.
Asahi River	Asahi River	B, C, and D	National Gov.
Asahi River		A	Okayama Pref.
Suna River		A	Okayama Pref.
Yoshii River	Yoshii River	B and D	National Gov.

*Remarks: A, dike breaching; B, water leakage from dike body (sand boiling at a landward area); C, dike protection failure; D, collapse of landward dike slope

Because of the catastrophic water-related disaster, 81 persons were killed in

Okayama Prefecture. Figure 1.1 portrays aerial photographs of the inundation area of Mabi Town and a dike breaching point (3.4 KP) taken a few days after the Oda River flooding. Hereinafter, the kilometer post (KP) value represents the longitudinal distance (kilometer, km) from the river mouth. The inundation area extended throughout approximately 30% of the Mabi Town. The dike breaching caused extensive inundation at several sections of the related rivers: The Oda River and its tributaries (Takama, Matani, and Suemasa rivers). In the Oda River, woody vegetation is established lushly along the river reach. In addition, in 1998, a massive flood (4310 m^3/s peak discharge) occurred in the lower Asahi River, Okayama Prefecture, Japan (Figure 1.2). Then, some residential areas were inundated severely; hydraulic structures were destroyed.

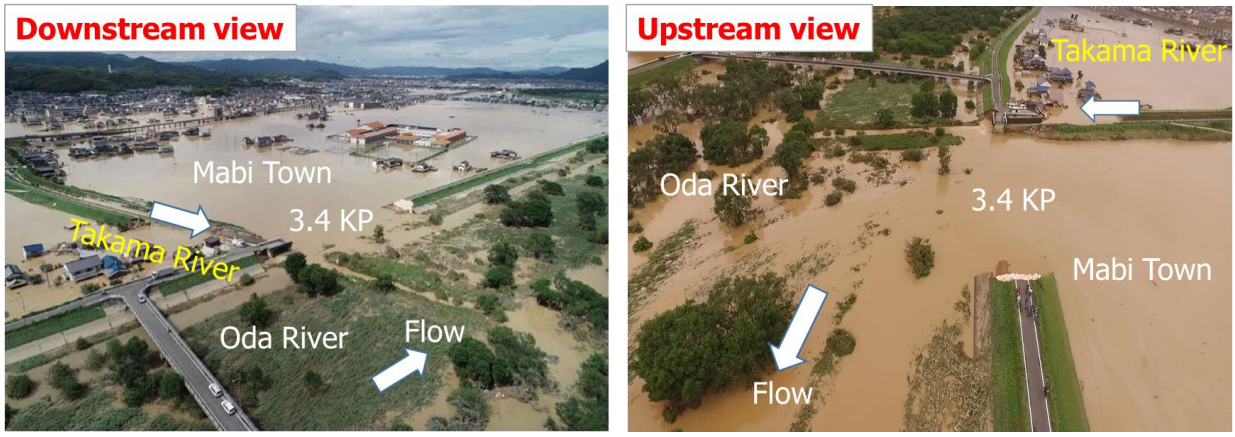

Figure 1.1 Inundation scene at Mabi Town, near the breaching point at the left-side bank of the Oda River (3.4 KP) and thickly established woody vegetation. Kilo post (KP) value denotes the longitudinal distance in km from the respective river mouth.

Figure 1.2 1998 flood scenes of the lower Asahi River, Okayama Prefecture, Japan.

Devastating damage commonly occurs because of overflow during river flooding. The overflow phenomenon is attributable to various factors, including unexpected heavy rainfall, low flow capacity in vegetated rivers with narrowed channel width, and insufficient flood control tasks, whereas vegetation can be managed artificially in a planned manner. Given that background, recent flooding events worldwide highlight the importance of detailed flood flow modeling that incorporates actual complicated flow regimes under real land cover used for preventing devastation through proper river engineering measures. Despite the fact that a considerable amount of research has already been conducted on the modeling of open-channel flow and parameterization of hydraulic resistance attributable to vegetation distributed both

on a laboratory scale and at the reach-scale using various 1-D (Fathi-Moghadam et al., 2011) and 2-D approaches to numerical simulations (Yoshida et al., 2020a), many unknown aspects remain to be explored. Using the yields of conventional numerical approaches developed to date, elucidating the complex flow environment around actual riparian vegetation is a challenging task. Consequently, a detailed 3-D interpretation is required to improve physical insights into flow phenomena, such as aids to river engineering measures. Finally, in this study, I introduced and evaluated a fully 3-D numerical modeling of recent floods in river corridors with complex vegetation.

1.3 Purpose of the study

My PhD research aimed to provide insight into the management of shallow clear-flowing vegetated rivers, as well as remote sensing of streamflow to validate hydrodynamic-numerical methods. Furthermore, the study findings are expected to aid policymakers in developing a balanced and rational scenario for flood control measures that take best vegetation management practices around river corridors into account.

My PhD research focused on the following specific goals.

- To spatially map and compare riverbed deformation to respective field measures and high-resolution aerial images using seasonal GLS datasets acquired before and after recent flooding;
- To confirm positional displacement and severely damaged parts of a river submerged structure with its surrounding area, which is expected to be useful for ongoing river engineering maintenance tasks;
- To assess the performance of the depth-averaged flow model after using GLS-

derived data as input and validation with varying numerical conditions and mesh sizes while accounting for computational costs and stability;

- To compare GLS-based numerical flow estimates with simulated results using ALB data;
- To inform novel approaches for estimating accurate vegetation heights and recommending riparian vegetation growth rates;
- To present multi-seasonal GLS-processed improved algorithms in classifying land covers with proper validation;
- To estimate the overall accuracy of the newly proposed land cover classification method by revealing individual percentages of distributed riparian vegetation (via confusion matrix) versus pixel-based true labels derived from all possible ground-truth evidence;
- To compare finer mesh-based depth-averaged flow model estimates to a non-contact methodology with novel GLS and deep learning-based imaging velocimetry approaches for remote analysis of on-site hydraulic quantities;
- To introduce a fully 3-D river flood simulation model with reach-scale turbulence parameterization using information related to topography, land cover, and vegetation distribution from seamless airborne point cloud data;
- To evaluate the accuracy of the newly constructed 3-D flood flow model in comparison to the conventional 2-D hydrodynamic-numerical model (as a reference), in addition to imaging STIV-derived flow data and field observations; and
- To ascertain the flood flow response (taking into account both major and minor recent flooding events) to the distributed vegetation conditions around the historic diversion weir in the lower Asahi River, Okayama Prefecture, Japan.

CHAPTER 2

Characterizing riverine hydro-environmental attributes using novel approaches to unmanned aerial vehicle-borne LiDAR and imaging velocimetry: Promises and uncertainties

2.1 Abstract

Recent advancements in remotely sensed techniques have markedly expanded data acquisition potential in riverine studies, but the techniques' applicability must be validated and improved because of uncertainties associated with diverse field conditions. This study is the first of a scientific platform that uses a newly designed unmanned aerial vehicle (UAV)-borne green light detection and ranging (LiDAR) system (GLS) and deep learning-based space–time image velocimetry (STIV) for remote investigation of hydraulic and vegetation quantities of the gravel-bed Asahi River in Okayama Prefecture, Japan. Aside from identifying bed deformation in waters shallower than 2 m, the GLS point clouds characterized the submerged infrastructure with block detailing patterns, thereby identifying positional displacement and severely damaged parts. The results were compatible with the corresponding high-resolution aerial images. Seasonal-GLS measures also revealed that LiDAR-derived elevation data, even after minor flooding events with varying conditions (underwater, bare ground, and beneath vegetation canopy), were nearly identical to ground-truth observations, with outperformed accuracy ranging from 2 to 14 cm of root-mean-square-error values. The study also assessed the performance of depth-averaged flow model after using GLS-derived data as input and validation with varying

numerical conditions and mesh sizes while accounting for computational costs and stability. In the case of the referenced 4 m mesh, GLS-based numerical estimates were aligned with evidence gathered using the airborne LiDAR topo-bathymetry (ALB) technique, but for the targeted finer–2 m mesh, the current UAV-based approach produced better simulation than the ALB. Furthermore, this study presents a non-contact method of estimating incremental river discharge. Compared to benchmarked flow model estimates, remotely sensed discharges for three transects covering shallower, deeper, and partially submerged woody vegetation areas were overestimated as 1–11%, with 4% underestimation for another cross-stream. The STIV analysis also showed complicated flow patterns that were reasonably confirmed by flow vectors from depth-averaged modeling. Ultimately, a finer mesh (2 m) based depth-averaged model validated hydraulic quantities derived remotely from GLS and STIV, and vice versa. In addition to approximation of 0.5–1.5 m per year for vegetation growth that varies among species, the study using GLS attributes accurately identified riparian vegetation types as herbaceous (70%), woody (86%), and bamboo groves (65%). That identification can help estimate spatially distributed hydrodynamic roughness and can support the preservation of desirable river ecosystems. Finally, the findings of the study provide insight into the management of shallow clear-flowing vegetated rivers and remote sensing of streamflow to validate hydrodynamic-numerical methods.

2.2 Introduction

Remote sensing of riverine environments, including topo-bathymetric, on-site streamflow, and discharge measurements of stream channels and floodplains, along with their vegetation distribution assessment, are detailed in Chapter 1. Among the

emerging remotely sensed techniques, a cost-effective UAV-borne green LiDAR system (GLS; TDOT GREEN, 2020) comprising a high-resolution lightweight camera, global navigation satellite system (GNSS) receiver, and an inertial measurement unit (IMU) (Mano et al., 2020), have been attracting the attention of river and coastal engineers. From a researcher and practitioner perspective, the salient advantage of the current GLS compared with other LiDAR-based techniques is the capture of laser point clouds and aerial images concurrently. Consequently, it is remarkably well suited for topo-bathymetry and land use mapping at a high spatial resolution as a result of the lower flying altitude above ground level, yielding a higher and homogeneous point density on the ground of about 100–200 points/m^2. However, although airborne techniques are apparently more productive for larger-scale measurements (Yoshida et al., 2020a), they have important shortcomings compared to UAV-based LiDARs, such as higher data acquisition costs and difficulties in balancing mission safety and flight conditions. For that reason, airborne LiDAR makes it challenging to carry out immediate assessments of river management works (e.g., Yoshida et al., 2020a). In contrast, using current GLS, information can be extracted easily, if necessary, particularly for clear and shallower rivers, because of its comparatively lower material and operating costs, drone-based operation, data measurement flexibility, and repeatability. Moreover, most airborne LiDAR approaches have no sufficient point density to capture artificial river structure shape effectively. In comparison, because of homogeneous point density, the novel GLS can be expected to allow individuals to reproduce hydraulic infrastructure and other smaller objects on the riverbed such as rocks, submerged driftwood, with potential applications for the portrayal of stream resistance in numerical hydrodynamic models. Therefore, because hydrodynamic-numerical methods (e.g., Barker et al., 2018; Yoshida et al., 2021) are vitally

important for numerous practical applications in river research and management, it is necessary to evaluate flow model performance after using GLS-derived data as input and validation with varying numerical conditions and mesh sizes while considering computational costs and stability. Furthermore, a vital issue of concern is how LiDAR-based measurements have been influenced by various environmental factors, such as flow and turbidity, depth, water surface waves, riverbed conditions, riparian vegetation, and atmospheric conditions (e.g., Kinzel et al., 2021). Advancing beyond these measurement shortcomings has been a slow process. Therefore, significant attention must be given to the level of accuracy of GLS to help address its promises and limitations, particularly for assessing riverine hydro-environmental attributes. Furthermore, Fujita et al. (2020) recently proposed a deep learning-based STIV technique for remote sensing of surface flow velocity along a specific cross-section, the benefits of which are already mentioned in Chapter 1 in comparison to other imaging approaches.

Because no report of the relevant literature provides a detailed overview of accurate validation of the new advanced GLS and STIV techniques, the current study uses both novel approaches to examine hydraulic and riparian vegetation quantities remotely with precise valuation. These remotely sensed techniques' potential was approximated based on correspondence between ground-truth observations, LiDAR- and STIV-derived information, and hydrodynamic–numerical model estimates. Because of the higher and more uniform point density of GLS data, the current study used GLS data in finer mesh (2 m)-based flow modeling, in addition to the commonly used coarse mesh (e.g., 4 m as referenced herein), while accounting for computational costs and model stability. Subsequently, the results were compared to

those obtained using ALB-based data. Such finer mesh-based numerical findings with positive stimulus are expected to be used in numerous hydro-environmental applications such as flow and sediment transport modeling, and for riverine habitat assessment. This study also used multi-seasonal GLS datasets to depict the deformation of riverbeds and submerged infrastructure caused by recent floods and other natural disasters. Furthermore, this study examines an entirely non-contact methodology for estimating river discharge based on surface velocity and cross-sectional area data, respectively derived from imaging-based and LiDAR-based techniques. Such a remote-sensing approach can be expected to pave the way for rapid and safe estimation of river discharges at ungauged sites, which can particularly help improve the numerical simulation of river-scale flow. In addition to suggesting riparian vegetation growth rates and depicting vertical structures, the current study proposed GLS-based novel land cover classification (LCC) methodologies to accurately identify individual percentages of distributed vegetation over the targeted site (via confusion matrix) in comparison to pixel-based true labels prepared from all possible ground-truth evidence. Quantitative findings for vegetation distributions can aid in the estimation of spatially distributed hydrodynamic roughness parameters and can support the preservation of desirable river ecosystems.

2.3 Study Site and Methods

2.3.1 Outline of the study site

The survey was conducted in the lower reaches of the Asahi River in Okayama Prefecture, Japan (Islam et al., 2022), covering a 1.2 km long channel (14.6–15.8 KP, locally called the "Gion area"), 300 m wide with an average bed slope of about 1:670 (Figure 2.1a). Throughout this study, Kilo Post (KP) numbers are expressed in terms

of longitudinal distance (km) from the river's mouth.

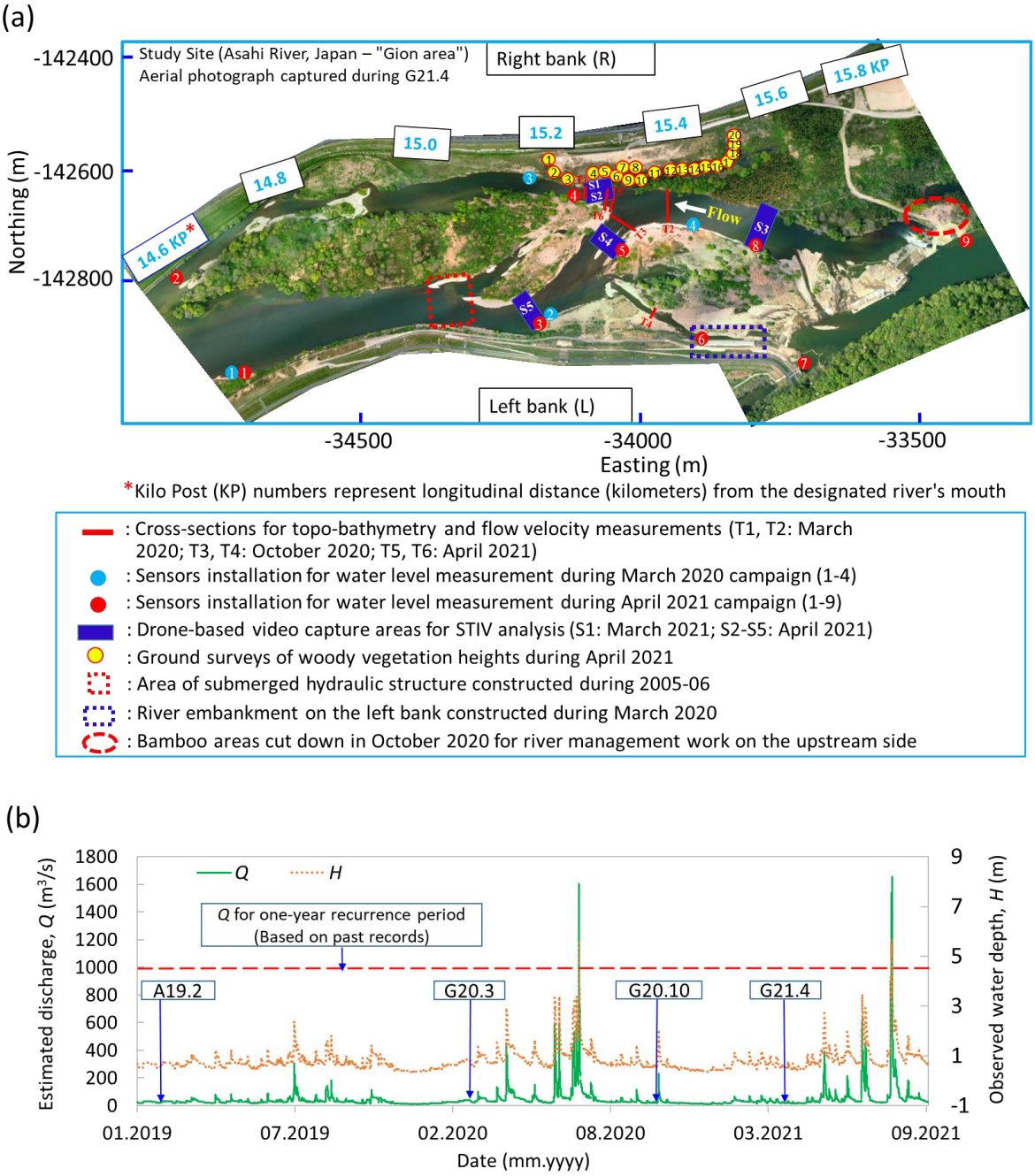

Figure 2.1 (a) Study site with ground-surveyed positions, and (b) overview of the lower Asahi River water level observed and discharge estimated at the nearest observatory station. A19.2, ALB measure on 05 February 2019; G20.3, GLS measure on 03 March 2020; G20.10, GLS measure on 27 October 2020; and G21.4, GLS measure on 09 April 2021.

Figure 2.1b presents the lower Asahi River water level observed and the streamflow rate estimated during 2019–2021 at the nearest hydraulic station, called Makiyama observatory (20 KP), located upstream beyond the domain of interest. It is noteworthy that, from the observatory to the upper end of the targeted field (i.e., 20–15.8 KP), no confluence of large tributaries exists. Figure 2.1b also depicts a minor flooding event in July 2020 with maximum discharge of approximately 1600 m^3/s, which might affect the channel's fluvial topography, including floodplain vegetation conditions. Originally, numerous gravel bars existed in this river reach, but the construction of several multipurpose dams in upstream river areas during the 1980s gave rise to riparian vegetation and lowered bedload transport, as Yoshida et al. (2021) reported. Consequently, research into spatially distributed floodplain vegetation, as well as streamflow features with precise valuation in the targeted reaches, is crucially important for practical flood risk assessment and for ecosystem management measures.

2.3.2 Remotely sensed measures and data processing

2.3.2.1 UAV-borne LiDAR data capture and positional accuracy assessment

A UAV-mounted GLS (TDOT GREEN, 2020) platform with a single green laser, a high-resolution camera, a dual-frequency global navigation satellite system (GNSS) antenna, data storage, and control unit (*i.e.,* inertial measurement unit, IMU) was deployed to conduct both underwater and overland measures (Figure 2.2a). Figure 2.2b elucidates photographic documentation of the instrumentation package and LiDAR mounted on a drone during the G21.4 campaign (09 April 2021), with quadratic gray-and-yellow checkerboard targets used as ground control points (GCPs) in the

foreground for the absolute orientation of laser scans.

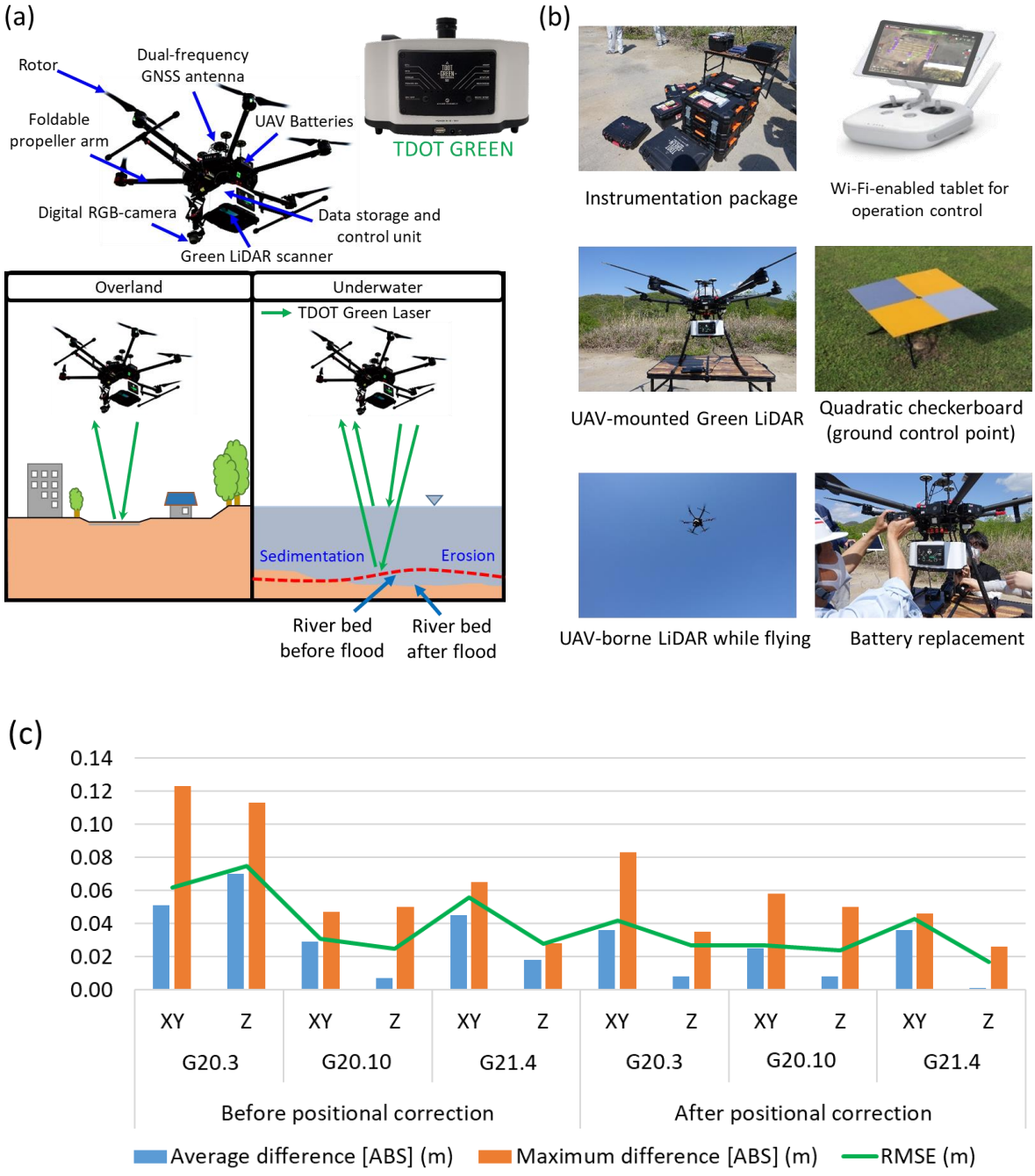

Figure 2.2 (a) Typical view of UAV-borne green LiDAR used for underwater and overland measures, (b) photographic documentation of the instrumentation package and LiDAR mounted on a drone during the G21.4 campaign, and (c) positional accuracy of GLS measures.

Furthermore, to capture data with desired attributes, overlapping coverage of the targeted area was attained by multiple flying operations during the G20.3 (03 March 2020), G20.10 (27 October 2020), and G21.4 deployments. Because of hazardous substances such as riparian vegetation along channel margins and floodplains, the UAV (DJI Matrice 600 Pro)-based LiDAR flew at 50–100 m above ground level (AGL). Table 2.1 presents the specifications of the UAV-LiDAR device used herein, including measurement conditions. The plane position of the UAV was generated following the world geodetic system, such as the Japanese geodetic datum 2011 and the fifth local Cartesian coordinate system. The approach of the measurement system is to obtain the distance from the round trip time of the laser beam irradiated to the ground or reflected from the targeted object. The LiDAR concurrently captures GNSS and IMU data to generate global coordinates-oriented 3-D laser point clouds with continuous connection between land and water bottom. Point clouds result from refraction in the water region, with one portion of the laser irradiation reflecting on the water's surface and the other portion reflecting on the riverbed's bottom. In this study, the water depth required for LiDAR-based river discharge estimation was calculated by distinguishing between the water surface and riverbed returns, retrieving spatial locations where the two types of returns coincided, and subtracting the riverbed height from the water surface elevation.

Besides, the optimal trajectory was assessed with a tightly coupled integration approach (Dorn et al., 2017) using base station- and UAV-based GNSS and IMU data. The trajectory analysis accuracy was within the equipment specifications, with a maximum of 20 mm or less in horizontal and vertical positions, whereas attitude accuracy (*i.e.,* pitch and roll) of 0.01 degrees or less.

Table 2.1 Specifications of the UAV-integrated green LiDAR with survey conditions used for the study

GLS measuremes		**G20.3, G20.10**	**G21.4**
Equipment specifications	Device name	TDOT GREEN	
	Weight (kg)	2.6	
	Dimensions (*L* x *W* x *H*) m	0.26 × 0.22 × 0.15	
	Laser wavelength (nm)	532	
Survey conditions	Pulse rate (kHz/s)	60	
	Scan speed (scans/s)	30	
	Maximum number of echoes per pulse	2	
	Divergence of the laser beam (mrad)	1.0	
	Average point density (points/m^2)	200	100 (underwater) 50 (overland)
	Field of view (°)	90	
	Flying altitude aboveground level (m)	50	50 (underwater) 100 (overland)
	Flying speed (m/s)	2.5	2.5 (underwater) 4.5 (overland)
	Degree of overlapping between flight paths (%)	75	75 (underwater) 60 (overland)
	River water turbidity	FTU[a]	NTU[b]
		0.80 (G20.3) 3.12 (G20.10) 2.45 (G21.4)	- 3.70, 3.70 and 5.50 (G20.10) 1.90, 2.60 and 2.80 (G21.4)

[a] Formazin Turbidity Unit (FTU) values were based on a laboratory analysis of samples collected near the water's surface; [b] Nephelometric Turbidity Unit (NTU) values were recorded respectively for the water surface, intermediate and bottom layers at a depth of about 1.5 m.

Before each LiDAR survey, positions of ten GCPs (six: verification points; four: adjustment points) were conducted using total station (TS)-based ground observation and a virtual reference system to evaluate positional accuracy. Figure 2.2c shows the verification results of the positional accuracy of the GLS measures using the shift correction method (Delefortrie et al., 2016) based on the difference between the coordinate values of the GCPs obtained from the ground-truth survey and the generated point cloud. The findings revealed that the position correction marginally improved the accuracy in the horizontal direction (XY), whereas vertical (Z) accuracy resulted in a remarkable improvement with a maximum of about 5 cm. This variation in accuracy is most likely due to point cloud reading uncertainties by the measurement points' interval of around 10 cm.

2.3.2.2 Laser point cloud processing

The traditional waveform approach used in ALB surveys is not used to record data from UAV-integrated green LiDAR measures. The reflective method is typically used by GLS, with up to four echoes recorded per laser pulse. However, reflection intensity values were recorded with a maximum of two echoes in the current study. However, the raw laser points were confirmed using commercial software (TDOT Pre PROCESSING Ver.1.6; Amuse Oneself Inc., Japan). Subsequently, 3-D point cloud data in (.las) file format were generated by employing software (TDOT PROCESSING Ver.5.9.5; Amuse Oneself Inc., Japan) with optimal trajectory results and raw data captured. In addition, software was used to correct underwater points (UNDERWATER CORRECT Ver.7.1; Amuse Oneself Inc., Japan). Figure 2.3 presents an overview of the main steps used in LiDAR-derived 3-D point cloud processing from the UAV platform.

For use in this study, 3-D laser point cloud data were processed by developing a Cartesian grid of 0.25 m cubic voxels to filter certain point clouds out of portions overlapped by multiple flying operations. Consequently, each voxel included only the datum from the topmost point cloud. A 2-D cell of 1 m by 1 m grid were also established, comprising point clouds in multiples of 16 voxels spread over the horizontal cell (Figure 2.4a).

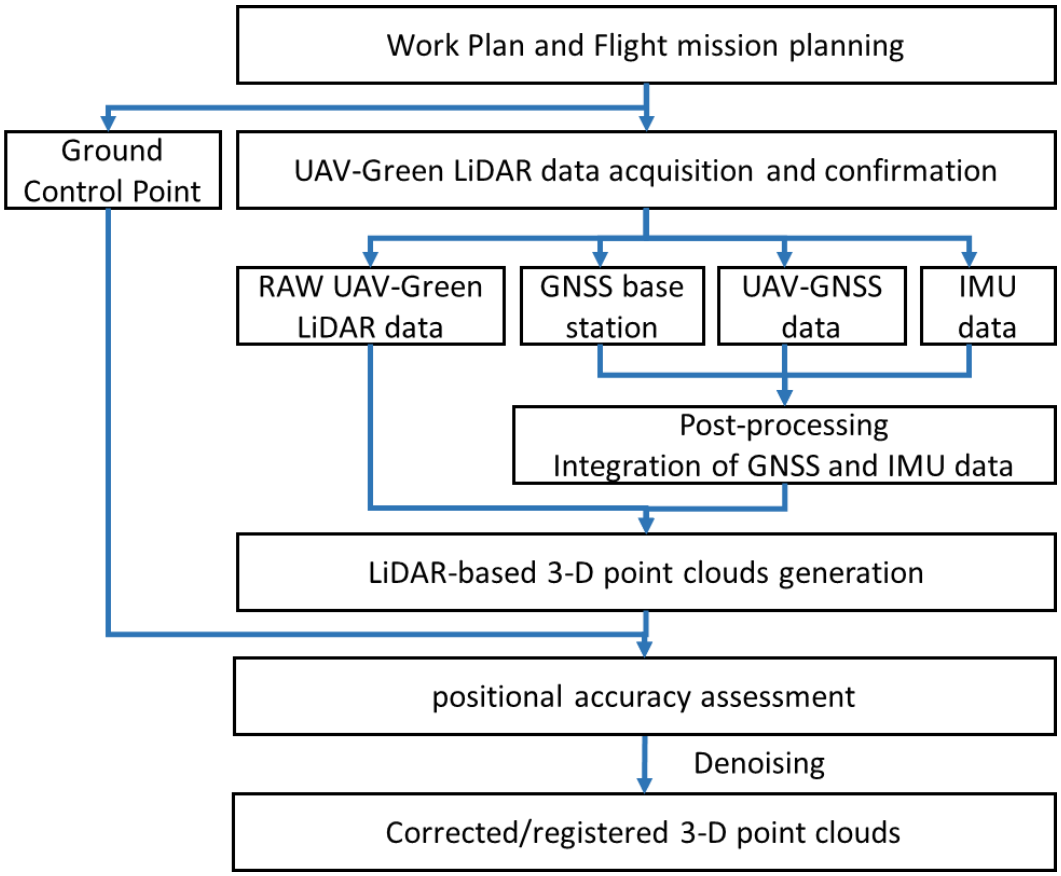

Figure 2.3 Schematic overview of the main steps in GLS data processing.

The homogenized point clouds within voxels on each horizontal cell were also counted (VOX_CNT). After such processing, ground level, called digital terrain model (DTM), data were obtained considering the lowest point of each 2-D cell. Furthermore, digital surface model (DSM) data were obtained by considering the uppermost point in each horizontal cell.

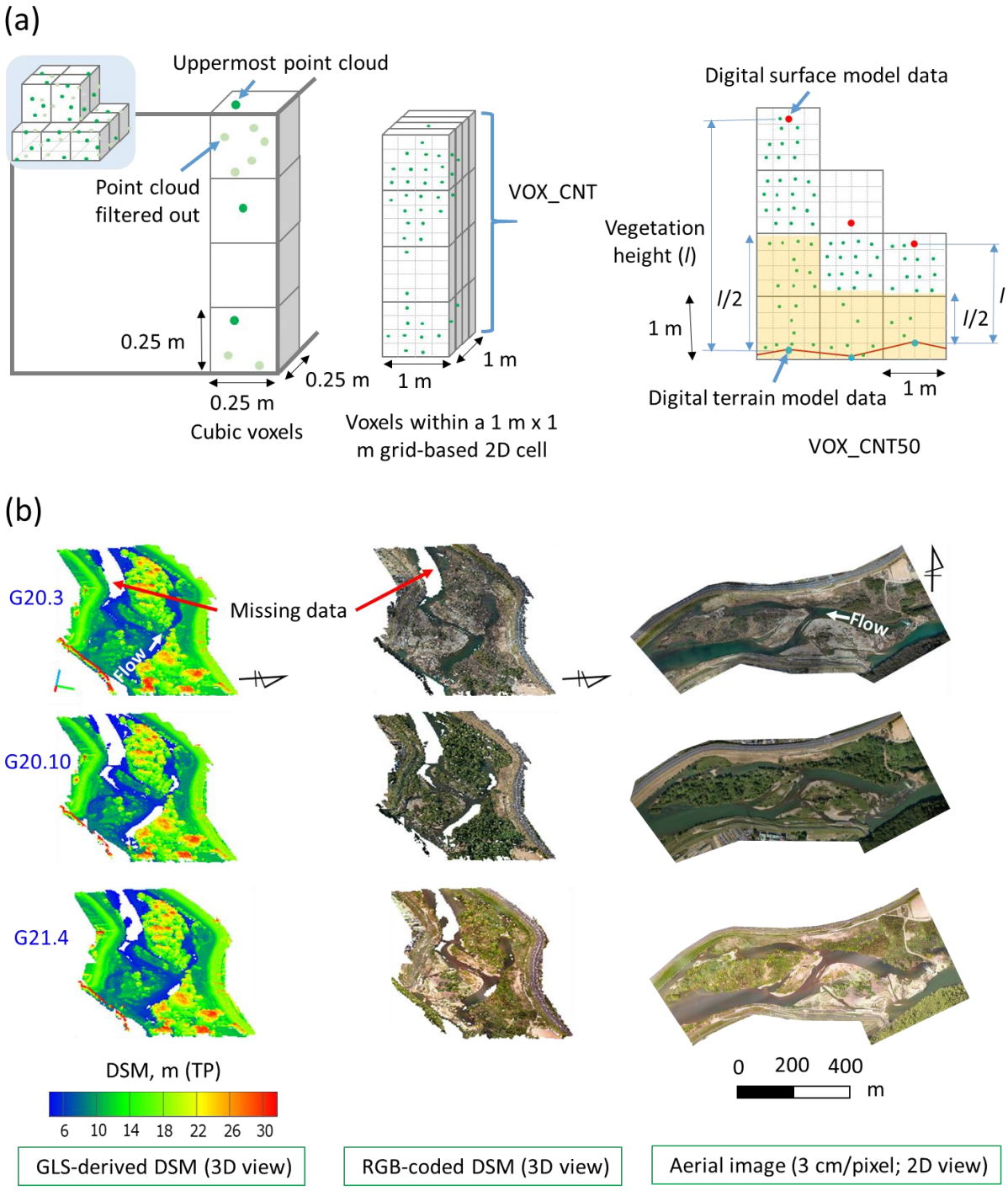

Figure 2.4 (a) Schematic overview of GLS data processing, and (b) spatial distribution of digital surface model-based data retrieved from UAV campaigns. Tokyo Peil (TP) denotes the referenced data level signifying the mean sea level of Tokyo Bay in Japan.

Using the difference between DSM and DTM (*i.e.,* DSM–DTM), designated as digital canopy model (DCM) data, the vegetation height (*l*) was assessed in each 2-D cell. In addition, the number of point clouds on each 2-D cell in the lower half of vegetation height (*i.e.,* VOX_CNT50; yellow-shaded part in Figure 2.4a, right side) was estimated. Finally, the lower layer points percentage (*i.e.,* Under % = (VOX_CNT50/VOX_CNT) × 100) was calculated as a parameter of land cover classification (LCC).

In addition, the red–green–blue (RGB) attribute was extracted from high spatial resolution aerial images captured concurrently during each GLS measurement with ground sampling distance of around 0.03 m/pixel. The elevation data obtained from the LiDAR-based DSM data were then combined with RGB information to produce color-coded DSMs. Figure 2.4b represents the spatial products of each GLS measurement, demonstrating that the color-coded DSM mappings (3-D views) obtained from the GLS correspond closely to the respective aerial photographs (2-D views), and that this mapping ensures consistency of the extracted DSM data. Consequently, the color-coded attribute provides a broad overview to specify the position and elevation of the individual object (*i.e.,* water, bare ground, vegetation, etc.), effectively assisting in LCC to distinguish the unexpected shallower water area from the bare ground. Furthermore, the spatial products revealed missing data in deeper waters during the GLS campaigns. The missing data is most likely due to insufficient laser power, flying height and river transparency metrics.

2.3.2.3 Updating UAV-LiDAR-derived missing data

When performing the depth-averaged numerical simulations described hereinafter, the missing bed elevation data of deeper waters evident during the G20.3 campaign

were revised using already reported February 2019 ALB (A19.2) data (Yoshida et al., 2021) obtained with 1.79 Formazin Turbidity Unit. The ALB data were offered by the Asahi River Office in Okayama Prefecture, Japan. The ALB-derived digital terrain model (DTM) data used to update the missing values in this study can be closest to the G20.3 condition because no major flooding took place in the targeted area during February 2019 – March 2020 (Figure 2.1b). Similarly, missing data for G21.4 measurement were updated using the same ALB data, assuming that bed deformation in deepwater areas during minor flooding in July 2020 was negligible compared to that of shallower regions. Furthermore, it is noteworthy that no recent ALB measurements were taken following the small flooding event in the lower Asahi River. The ALB surveys tend to be conducted generally after larger-scale flooding events, which might be attributable to the enormous expense of data collection, as past overviews have shown (e.g., Yoshida et al., 2020a). In such cases, the UAV-borne GLS is expected to be a promising tool, particularly for the periodic assessment of shallow rivers with vegetated floodplains after each flood event.

2.3.2.4 UAV-based image acquisition and STIV analysis

To capture vertical shooting above the pre-specified sites of the targeted river reach (Figure 2.1a), a mini and low-cost drone (Mavic 2 Pro; DJI Inc., Japan) was chosen. The drone specifications, including the video camera, are presented in Table 2.2. During the campaigns (S1: 08 March 2021; S2–S5: 07 April 2021; see Figure 2.1a), the UAV was connected by Wi-Fi to a tablet; it functioned using a DJI GO 4 application. The study used the "tripod flight mode" option, which helps capture stable and smooth videos while slowing down the drone. The drone hovered at approximately 40–60 m AGL over the selected areas, capturing videos lasting about 1 minute in each case.

Table 2.2 Specifications of a drone-mounted video camera and software used for image velocimetry analysis

Drone specifications	Model name	DJI Mavic 2 Pro
	Takeoff weight (g)	907
	Dimensions (*L* x *W* x *H*) mm	Folded state: 214 × 91 × 84 Unfolded state: 322 × 242 × 84
	Maximum flight time (min)	31
	Satellite positioning	GPS/GLONASS
	Hovering accuracy (m)	Vertical ±0.1 m Horizontal ±0.3 m
	Transmission power (GHz)	2.400–2.483
	Flying height above ground level (m)	40–60
Camera specifications	Sensor	1" CMOS
	Lens	28 mm lens (77° field of view)
	ISO sensitivity	Video: 100–6400
	Video resolution (pixels)	4K: 3840 × 2160; 30 fps
	Video format	MP4 (MPEG-4 AVC/H.264)
	Stabilization	3-axis mechanical (tilt, roll, pan)
Image velocimetry software specifications	Software name	Hydro-STIV
	Searching line length (m)	8.00–28.50
	Analysis period (s)	60

A novel approach, space–time image velocimetry (STIV), may be a quick and effective image analysis tool for evaluation of streamwise velocity distributions using video images. This study used the newly released Hydro-STIV software, which incorporates a deep learning-based convolutional neural network algorithm (Fujita et al., 2020). An important requirement of STIV is that the brightness or color of the water surface must change with the water flow. The streamflow is estimated based

on user-defined parallel search lines to the main flow direction rather than the image's entire field. Table 2.3 compares the accuracy of geometric corrections of video images used in STIV analysis (for section S1 as an example) to pixel-based and benchmarked GCPs coordinates, revealing the plane position and height errors of 0.07–1.020 m, supporting the product developer's recommended limit of 2 m for proper analysis in larger river sections.

Table 2.3 Accuracy valuation of geometric corrections of video images used in space-time image velocimetry analysis (for section S1)

Ground control points (GCPs) number	**RTK-GNSS-based GCPs coordinates**		**Pixel-based coordinates**		**Estimated errors**	
	X (m)	*Y* (m)	*X* (pixel)	*Y* (pixel)	*dX* (m)	*dY* (m)
1	34068.144	142586.271	438.773	1055.545	-0.157	0.485
2	34070.426	142588.282	632.679	1409.678	-0.481	0.801
3	34070.442	142592.289	1108.258	1575.008	-0.632	0.585
4	34066.885	142590.787	1091.929	1112.696	-0.277	0.712
5	34066.280	142588.321	821.481	934.099	-0.190	0.792
6	34062.065	142586.549	781.680	357.485	0.084	0.712
7	34061.903	142588.523	1053.148	449.335	0.151	0.895
8	34068.610	142606.950	2825.853	2011.805	-0.414	-0.823
9	34066.120	142609.401	3215.705	1841.373	-0.184	-1.000
10	34065.231	142606.384	2910.559	1605.624	-0.119	-0.769
11	34063.115	142608.763	3275.918	1472.952	0.070	-0.943
12	34060.835	142609.081	3405.527	1231.367	0.300	-1.010
13	34060.457	142606.173	3092.866	1066.223	0.370	-0.748
14	34057.668	142605.730	3165.233	732.222	0.616	-0.707

2.3.3 Depth-averaged flow modeling

For steady-state streamflow simulation in the targeted domain, the study employed a 2-D hydrodynamic-numerical modeling approach based on the boundary-fitted

coordinate system in a conservative form (Yoshida & Maeno, 2014; Yoshida et al., 2021). In the current shallow-water model, the local water depth and depth-averaged velocities were regarded as dependent flow variables. Hydrodynamic roughness attributable to gravel-bedded conditions was computed using Hey's formula (Rickenmann & Recking, 2011). Employing the finite difference method with the support of the finite volume method's concept, the governing flow equations used in the model were discretized in a staggered mesh. Computation on the time development of the flow variables was performed using an explicit second-order Adams-Bashforth scheme. In contrast, the second-order central difference technique was employed to discretize spatial derivatives, except for advection terms, which were computed based on the first-order upwind approach.

Movements of water edges varying over time were captured considering both continuity and simplified momentum equations. The water level gradient and bed friction were evaluated using two terms of the momentum equations (Yoshida & Maeno, 2014). The numerical mesh was composed of 615 × 167 cells, signifying 615 longitudinal cross-sections and 167 nodes in each cross-section. The mesh size was estimated to be around 2 m on average. Based on computational cost and stability, a referenced mesh size of 4 m on average with 305 × 85 cells was also considered for comparisons with the targeted finer mesh (2 m)-based simulated findings. The boundary conditions were defined as upstream discharge data obtained from the nearest observatory station database and downstream water level information acquired through portable pressure-type sensor (S&DL mini electrical conductivity meter) observation. Based on preliminary simulations, a threshold water depth of 0.01 m was used in the drying state assessment to prevent its uncertainty, which

might be caused by high velocities near the wet–dry boundary. Furthermore, a velocity of zero and the slip-velocity were considered for the computational nodes in the dry bed and water's edge conditions, respectively. The numerical analysis conditions for the depth-averaged hydrodynamic-numerical model applied in this study are presented in Table 2.4. Also, the computational details were demonstrated in the earlier studies report (Yoshida & Maeno, 2014; Yoshida et al., 2021).

Table 2.4 Computation conditions for depth-averaged hydrodynamic-numerical model applied for this study

Parameters	Assigned values
Numerical calculation time (hr)	10
Calculation time interval (s)	0.01
Completion step	360000 × 10
Water level downstream gradient as an initial condition	1.0/750.0
Threshold water depth (m) (Criteria for water/land boundary)	0.01
Gravel bar size via sieve analysis for Hey's formula[a], D_{85} (mm)	57
Computational mesh	305 × 85 cells (Referenced) 615 × 167 cells (Targeted)
Averaged numerical mesh size[b] (m)	4 m (Referenced) 2 m (Targeted)
Upstream boundary condition (Discharge at upstream from observatory station database)	26.16 m^3/s (23 March 2020; G20.3) 19.67 m^3/s (07 April 2021; G21.4)
Downstream boundary condition (Water level at downstream via pressure-type sensor observation)	6.93 m (23 March 2020; G20.3) 6.87 m (07 April 2021; G21.4)
Execution time (i.e., central processing unit, CPU run-time) to perform numerical simulation	21 hrs (For 4 m mesh) 131 hrs (For 2 m mesh)

2.3.4 Ground-truth measurements

To verify UAV-based GLS data and to validate the flow model estimates along with imaging velocimetry analysis results, topo-bathymetric and velocities were locally surveyed during the respective UAV campaign. The locations of all ground-truth surveys were depicted earlier in Figure 2.1a. Using total station (TS) and a measuring rod, benchmark measurements were taken of the riverbed elevation and the water depth along specified cross-sections. Water levels were monitored in real time by installing several portable pressure type sensors at specific positions to validate the model-based simulated findings. The sensor-based data additionally verifies the LiDAR-derived water level data used as input in Hydro-STIV analysis to estimate the incremental river discharge through specified transects. Furthermore, the average flow velocity was calculated by taking three readings with a digital current meter for each specific interval of the local cross-section. Water edge positions were also measured using a TS and a real-time kinematic global navigation satellite system (RTK-GNSS) with a dual-frequency network to validate the GLS-based hydrodynamic model estimates. Furthermore, before the UAV flights, a maximum of 14 GCPs was placed along the banks of the river's specified sites to establish survey control for moving images captured for STIV analysis. Herein, the RTK-GNSS surveying instrument was applied to identify the targeted GCP positions. In recent years, an unprecedented diversity of vegetation has been observed in the study area, dominated by woody plants (*i.e.,* willow) and bamboo trees. In this study, a few willow heights were locally surveyed via TS and measuring rod to validate GLS estimates and to verify vegetation growth rates calculated considering the one-year gap between GLS campaigns.

2.3.5 True label mapping for LCC accuracy assessment

For this study, a pixel-based performance evaluation method of confusion matrices (Story & Congalton, 1986) was applied to assess the overall accuracy (OA) of GLS-based predicted information for LCC mapping versus ground-truth evidence, designated as true label. Based on results of earlier field observations of typical vegetation species in the targeted river presented in a recent report (Yoshida et al., 2021), the land-cover objects were classed in the study area using the following labels: water, bare ground, herbaceous, arborous or woody, bamboo species, and others. Herein, single true-label mapping (Figure 2.5a) was drawn instead of different seasonal cases because the process was expensive, time-consuming, and laborious. Information was gathered from a 0.03 m/pixel orthophoto captured during the G20.3 campaign in a no-leaf condition (Figure 2.4b, right). The targeted region had some high-density bamboo areas combined with some trees. However, in orthophotographs, trees with leaf-on states are challenging to differentiate from bamboo. Consequently, in true label mapping, the study primarily preferred orthophotos from the late winter (G20.3) over the other two seasonal high-resolution orthophotos with leaf-on conditions. Mapping clarified that, in a few cases, herbaceous species under larger trees were visualized and were depicted in the true label, which might be difficult in leaf-on conditions. Furthermore, despite the existence of short or mowed herbaceous species near the river banks (Figure 2.4b, right; Figure 2.5c), these species were labeled as bare ground. This consideration in labeling herbaceous species was attributable to the fact that, in the newly proposed LCC methodology (see section 2.4.2.1), up to 0.3 m of the GLS-derived digital canopy model (DCM) values were regarded as bare ground. Figure 2.5b, for example, shows five sampled true labels along with their corresponding aerial images from the targeted period.

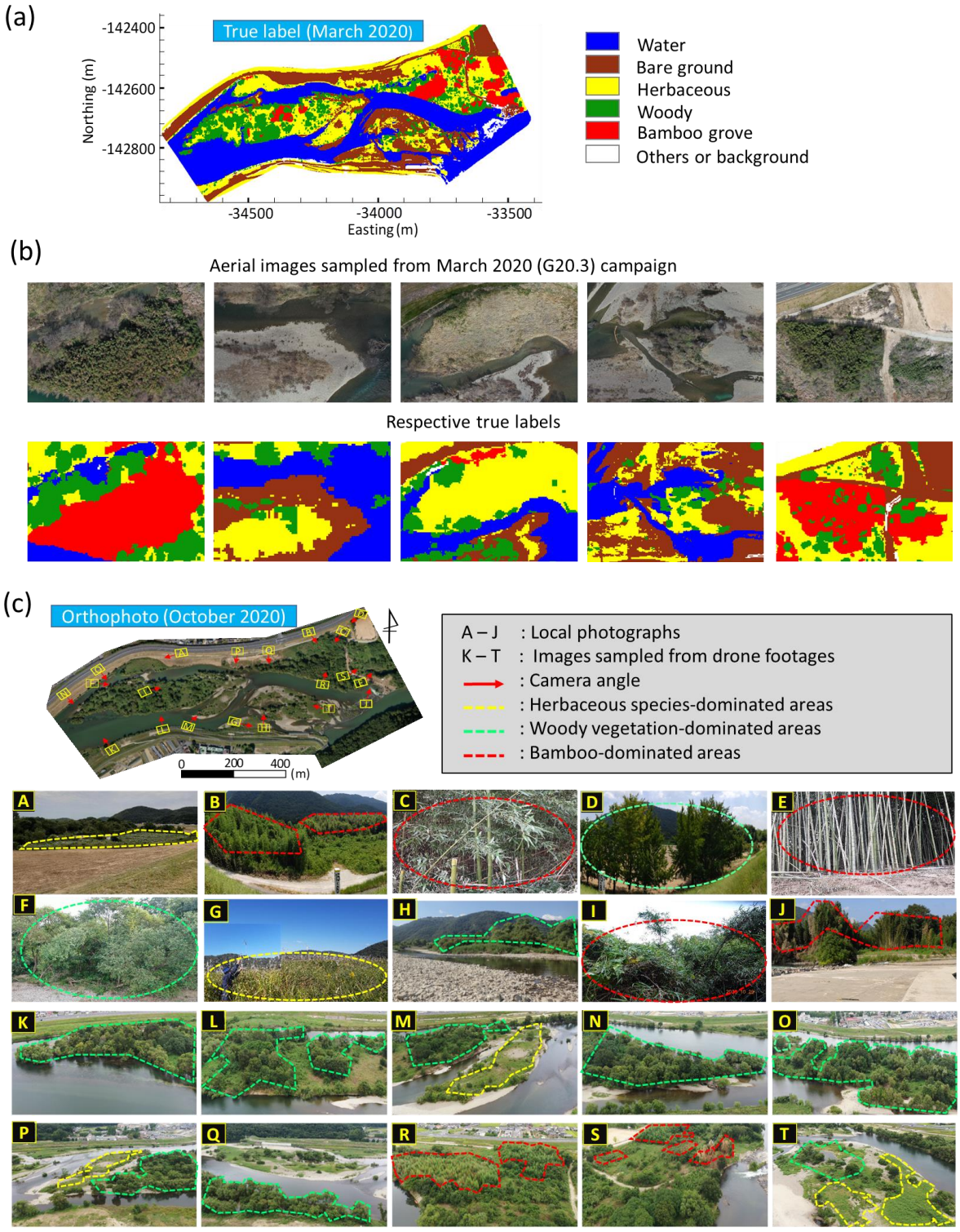

Figure 2.5 (a) True label mapping using ground-truth evidence, (b) sampled high spatial resolution aerial images (from G20.3 campaign) with corresponding true labels, and (c) photographs taken locally and images gathered from aerial footage (September 2020) for true label preparation.

In the referenced mapping, the spatial distributions of the targeted three-set vegetation species, specifically the dominant woody and bamboo varieties, were also confirmed from earlier field observation experience, including local photographs and aerial photographs sampled from UAV-based video footage in September 2020 (Figure 2.5c).

Furthermore, whereas the true label mapping was based primarily on aerial photographs taken in late winter (G20.3), the tree-dominant and bamboo-dominant areas were additionally confirmed and modified as necessary based on other seasonal aerial images (G20.10 and G21.4; leaf-on condition) and field visits, which aided us in distinguishing those species by providing critical information according to texture and color differences. In addition, a few parts of the overland areas were labeled as others or background (white-colored part) because of some machinery, anthropogenic barriers, concrete structures, cars, and so on used for river management works. Although the true label prepared herein was reasonably confirmed based on the ground-truth evidence, a few uncertainties about this benchmarked mapping remain because it was drawn entirely from the perspective of human eyes.

2.4 Applications and Discussion

2.4.1 Evaluation of topo-bathymetric and hydraulic quantities

2.4.1.1 Comparison of topo-bathymetric mapping and field surveys

Figure 2.6a depicts color contour mapping of riverbed deformation, particularly in shallow water regions, using processed DTM data of 2 m squared mesh from the

currently studied multi-seasonal GLS and existing ALB surveys. The plus and minus sign values respectively represent deposition and scouring throughout the deformation mapping. As stated earlier (see section 2.3.2.3), the GLS data was updated with previously available February 2019 ALB (A19.2) (Yoshida et al., 2021) data to account for missing GLS measures in deeper water. To verify the data revision, we assessed the riverbed change between the G20.3 and A19.2 campaigns (Figure 2.6a, left), which revealed no marked variation at the shallower zones, except for the black-dotted areas, because of anthropogenic works confirmed from seasonal orthophotos and field visits. Such an illustration verifies that no flooding occurred during the one-year gap separating the two targeted LiDAR surveys, and also supports the earlier graphical representation of the studied river's flow overview (Figure 2.1b). From this perspective, it can be inferred that bed deformation in deeper waters was negligible during the GLS data updates. Finally, using the difference in updated DTMs of G21.4 and G20.3, considerable deformation of 1.5–2.0 m (Figure 2.6a, right; see red-dotted areas) was identified, except for the black-dotted regions that were deformed because of artificial works for river management measures, despite minor flooding between the survey periods (Figure 2.1b). Figure 2.6a also confirmed the anthropogenic works between the survey periods using aerial photographs captured concurrently during LiDAR campaigns. Figure 2.6b depicts the numerically estimated water depth over the targeted domain, with the maximum being approximately 2.08 and 1.64 m, respectively, using updated data of G20.3 and G21.4 measures, excluding the revised missing data areas. Furthermore, the mappings were spatially superimposed with their respective high-resolution orthoimages to validate the bathymetry maps' water edges. Aside from image validation, the water edge positions were reasonably confirmed after plotting the

field-surveyed data.

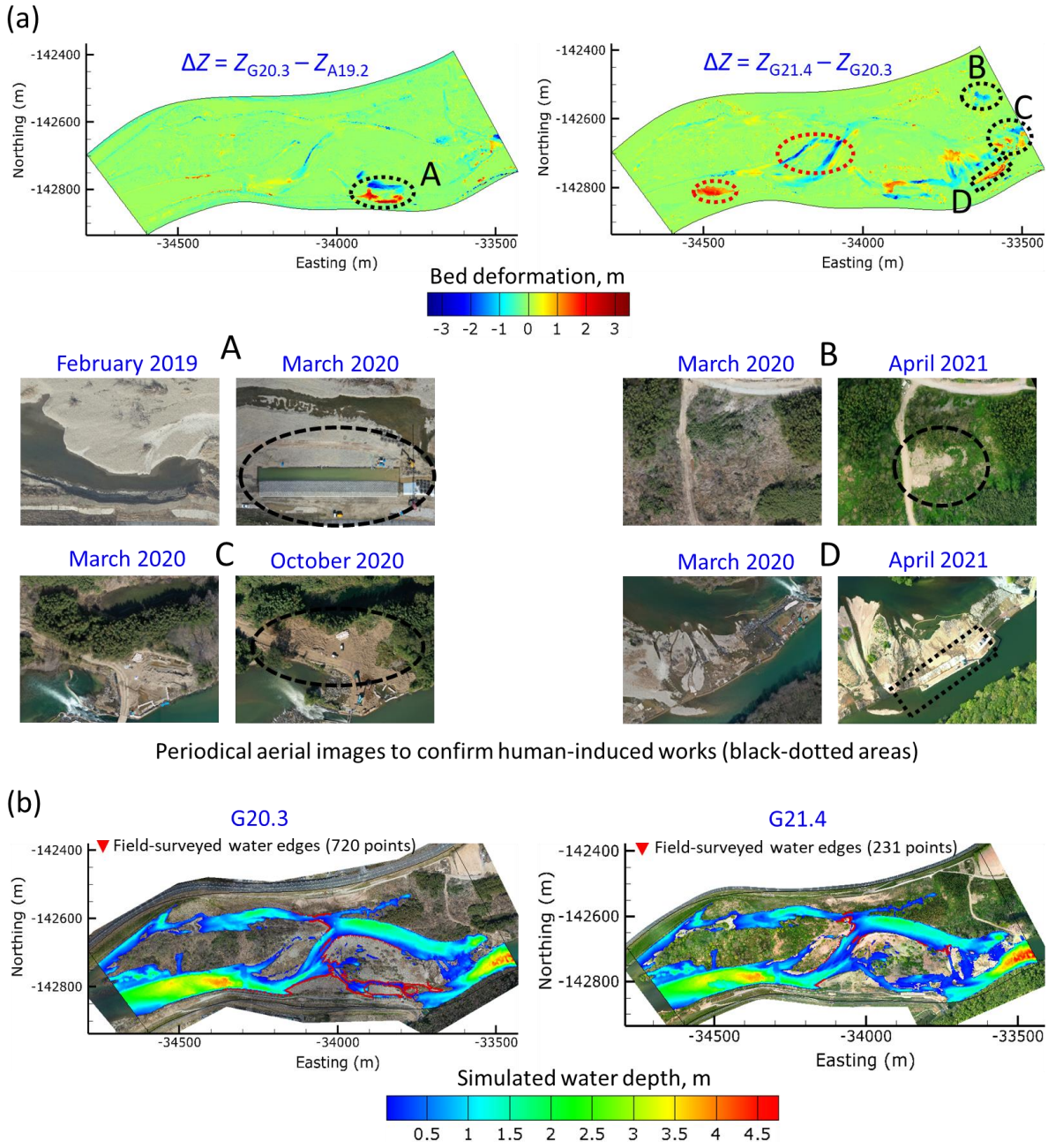

Figure 2.6 (a) Riverbed deformation mapping using digital terrain model (DTM) data (black-dotted, deformation because of artificial works, where red-dotted, substantial riverbed changes because of flooding); and (b) numerically simulated flow depth mapping (2 m squared mesh).

Furthermore, GLS point clouds from various periods over a year aided in identifying

riverbed changes in underwater measures and even in densely vegetated floodplains (Figure 2.7) caused by the recent minor flood in July 2020.

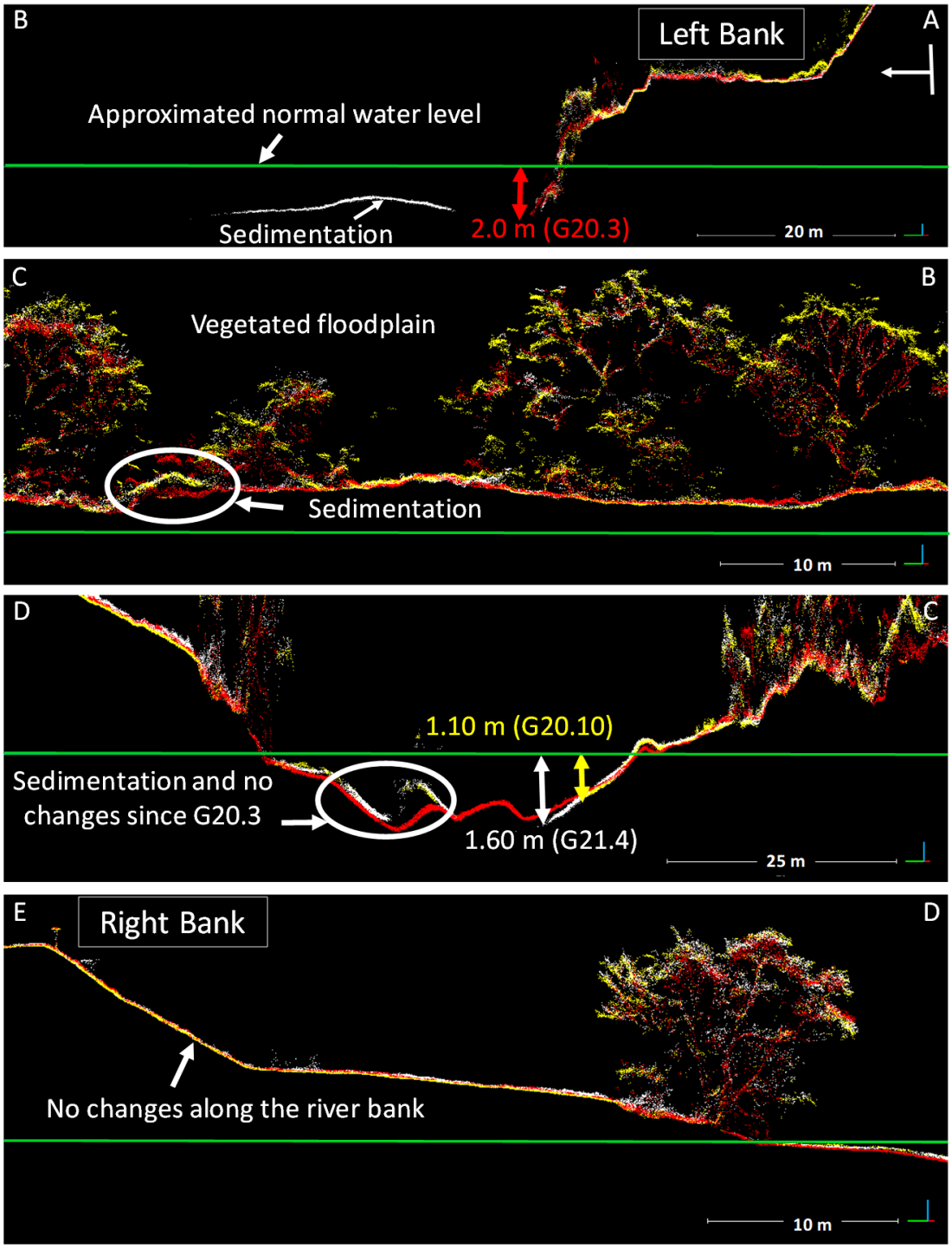

Figure 2.7 Cross-sectional illustration of topo-bathymetric attributes measured across 14.8 KP from left to right bank during three periods using GLS point clouds (Red, G20.3; Yellow, G20.10; and White, G21.4).

Seasonal GLS also approximated shallow bathymetry of less than 2 m by differentiating between LiDAR yields from the water surface and from the riverbed. Those yields varied with turbidity over time. For that reason, the method provides reliable support for flow model estimates.

Consequently, continuous 3-D data connecting the land and shallower water parts were generated, which is typically challenging to obtain using traditional techniques (e.g., sonar) because these systems are intended primarily for use in greater depths, although shallow bathymetry is crucial for diverse fluvial and ecological functions (Kaeser et al., 2013). However, the current bathymetric results were partially consistent with those reported in a recent review by Mandlburger et al. (2020), who stated that the current laser can penetrate up to 2 m in turbid waters. The earlier report highlights the absence of survey periods with detailed measurement conditions and river transparency indices, despite this information being important for various scientific applications. In contrast, the present study showed detailed measurement valuations to address the more recent drawbacks. Additionally, the bathymetric study results revealed that the current GLS outperformed another UAV-borne topo-bathymetric LiDAR reported recently by Kinzel et al. (2021), who observed bed returns of up to 0.95 m of water in a coarser-bedded reach with a 6 Nephelometric Turbidity Unit at 4 m flying height above the water surface. Furthermore, to address the GLS accuracy in elevation measures, the DTM data under varying conditions were compared with the respective field surveys, revealing that the root-mean-square error (RMSE) values for the G20.3, G20.10, and G21.4 campaigns were 0.068, 0.090 and 0.123 m (underwater); 0.020, 0.050 and 0.078 m (bare ground); and 0.121, 0.129 and 0.140 m (under canopy) (Figure 2.8). Despite the presence of turbid water

(Table 2.1), bed materials with diameters in the tens of centimeters (Maeno & Watanabe, 2008; Yoshida et al., 2020a), and densely vegetated floodplains, GLS performance of bed elevation measurements were closer to the respective ground-truth information.

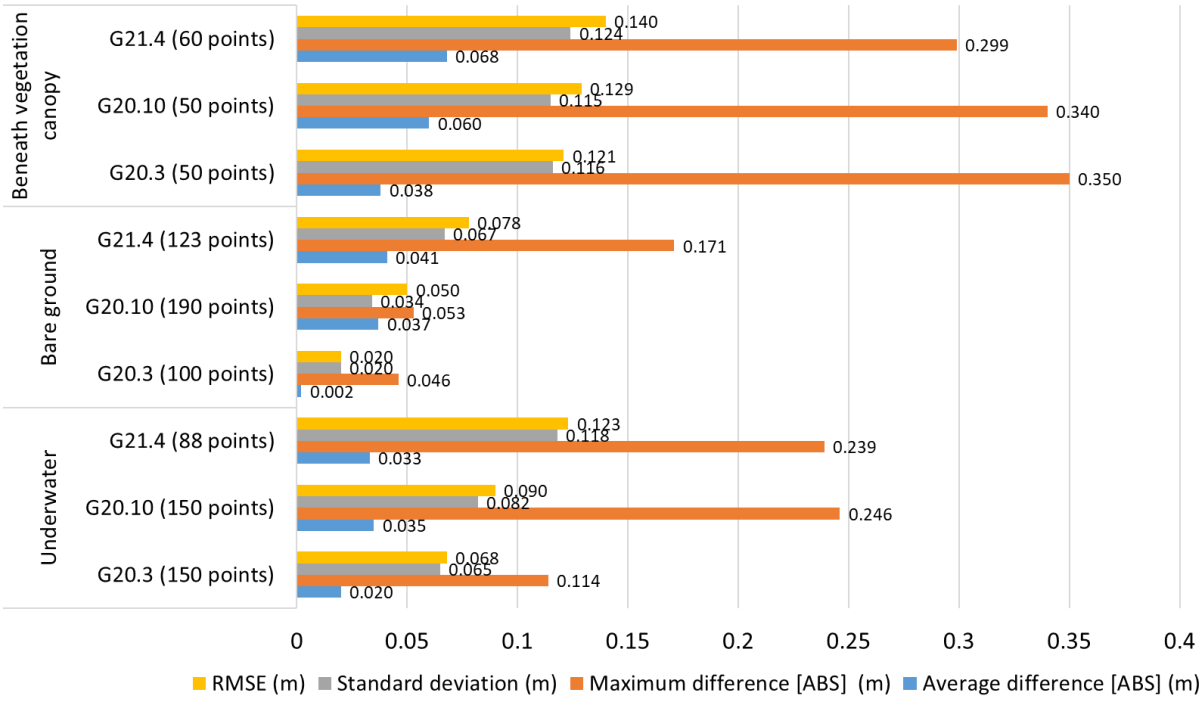

Figure 2.8 GLS accuracy in elevation data captures for various conditions compared to corresponding local measures. ABS, absolute; RMSE, root-mean-square error

To validate the riverbed deformation mapping described above, Figure 2.9a presents comparison of field surveys of bed elevation with the targeted GLS-derived DTMs along the six local transects (Figure 2.1a), addressing both shallow and deep waters. Because ground-truth surveys were conducted at 1–2 m intervals, the study chose a finer mesh size of 2 m for numerical analysis.

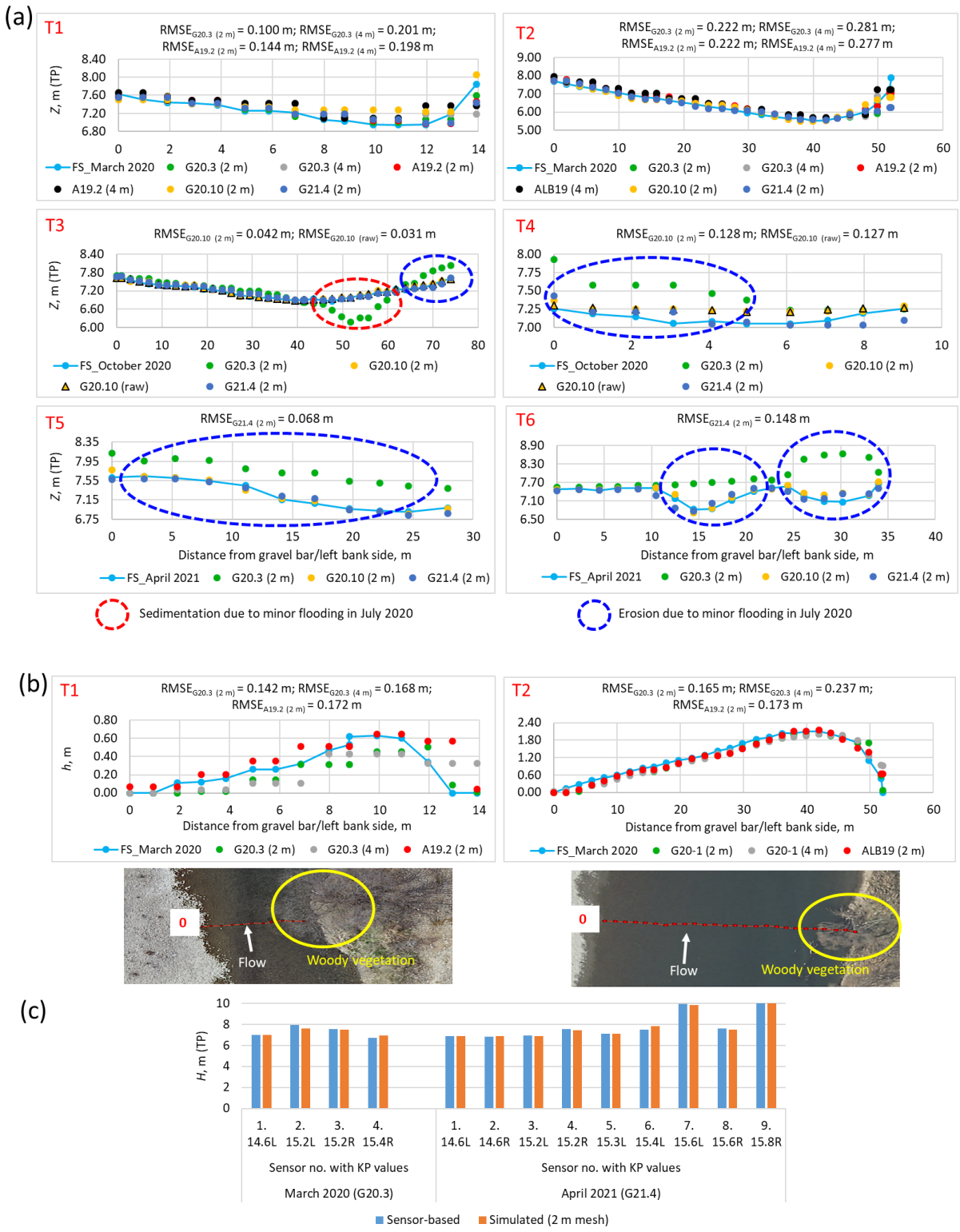

Figure 2.9 Comparison of field-surveyed (a) riverbed elevation (*Z*), (b) flow depth (*h*), and (c) sensor-recorded water level (*H*) with corresponding model estimates using LiDAR-derived DTMs. FS, field survey; L, left bank; R, right bank; RMSE, root-mean-square error; and TP, Tokyo Peil as referenced data level signifying the mean sea level of Tokyo Bay in Japan.

Herein, LiDAR-based DTMs were generated for simulation using the previously processed raw data of mesh size 1 m, considering the nearest grid points. Based on comparisons between before (G20.3) and after (G20.10 and G21.4) flooding datasets, as well as respective field measurements, the significant deposited (red-dotted) and eroded (blue-dotted) areas were identified along the targeted cross-sections, except for the T1 and T2 sections (Figure 2.9a). The findings indicate that seasonal GLS measures reasonably validated the riverbed change, with a maximum of around 1.5 m (T6 section) because of the minor flooding event (Figure 2.1b) between the survey periods. Furthermore, for the T1 and T2 cross-sections, the study compared the targeted 2 m mesh-based elevation data to those from the referenced 4 m mesh, revealing that the current mesh significantly improved the estimated RMSE values compared to the referenced mesh findings. The T1 section also demonstrated that using finer mesh in GLS data improved the elevation accuracy to about two times that of ALB data. This variation is most likely attributable to the ALB measure's lower and non-uniform point density (Yoshida et al., 2021). Additionally, the 2 m mesh-based bed elevations were compared with smoothed DTMs data processed from spatially distributed raw point clouds using locally weighted scatterplot smoothing (lowess) fit technique (Helsel & Hirsch, 2002), revealing no significant difference in the estimated RMSE values (T3 and T4 sections; Figure 2.9a). Therefore, considering the accuracy valuations, streamflow simulation using GLS data of 2 m mesh can be expected to perform better than using the referenced 4 m, even though computational costs are higher in the current setting. Furthermore, to validate the spatial mapping of simulated water depths presented earlier, Figure 2.9b presents a comparison between GLS-based numerical estimates and field-surveyed values along the two local sections (T1 and T2), demonstrating that the simulated depths were

closer to the field observations, except for a few points at the right end, because of both steep sloppy and woody vegetated areas. In terms of estimated RMSEs, a comparison of findings of depth elucidation revealed that 2 m mesh-based simulation was more effective than the 4 m estimates. In addition, Figure 2.9c reasonably confirmed the model estimates of water levels using seasonal GLS data in comparison to the corresponding pressure-type, sensor-based information at various KP positions (Figure 2.1a). However, in a more recent report (Yoshida et al., 2020a), pilot-operated ALB was used for topo-bathymetric measurements in fluvial environments, demonstrating that the LiDAR performance was nearly identical to that of local observations. The study reported herein compared G20.3-based findings with those from previously available A19.2 data (T1 and T2 sections; Figures 2.9a,b) because no significant flooding event occurred between the two targeted measures. Comparative results revealed that GLS-based estimates were aligned with evidence gathered using the airborne technique in the case of 4 m mesh, but for 2 m mesh, the current UAV-based approach produced better simulation than the ALB. The findings also validated ALB data that had been used previously to revise the missing GLS data as input in numerical modeling. Therefore, the current GLS would be deemed a practical option for the more common airborne (e.g., Yoshida et al., 2020a) and other remotely sensed (e.g., Legleiter & Kinzel, 2021) approaches for shallow and clear-flowing river bathymetric measurements.

2.4.1.2 Reproduction of hydraulic infrastructure with surrounding deformation

Figure 2.10a depicts elevation step mapping of a submerged infrastructure using GLS returns obtained at around 15.0 KP on the left bank. It was possible to reproduce its block-shaped patterns and mark the locations where some blocks were collapsed

using the G20.3 point clouds. The G20.3-based reproduction was validated by comparing its orthophoto, captured concurrently during the LiDAR survey. Furthermore, the shape and patterns were ensured from a photographic view of the hydraulic structure during construction work in 2006.

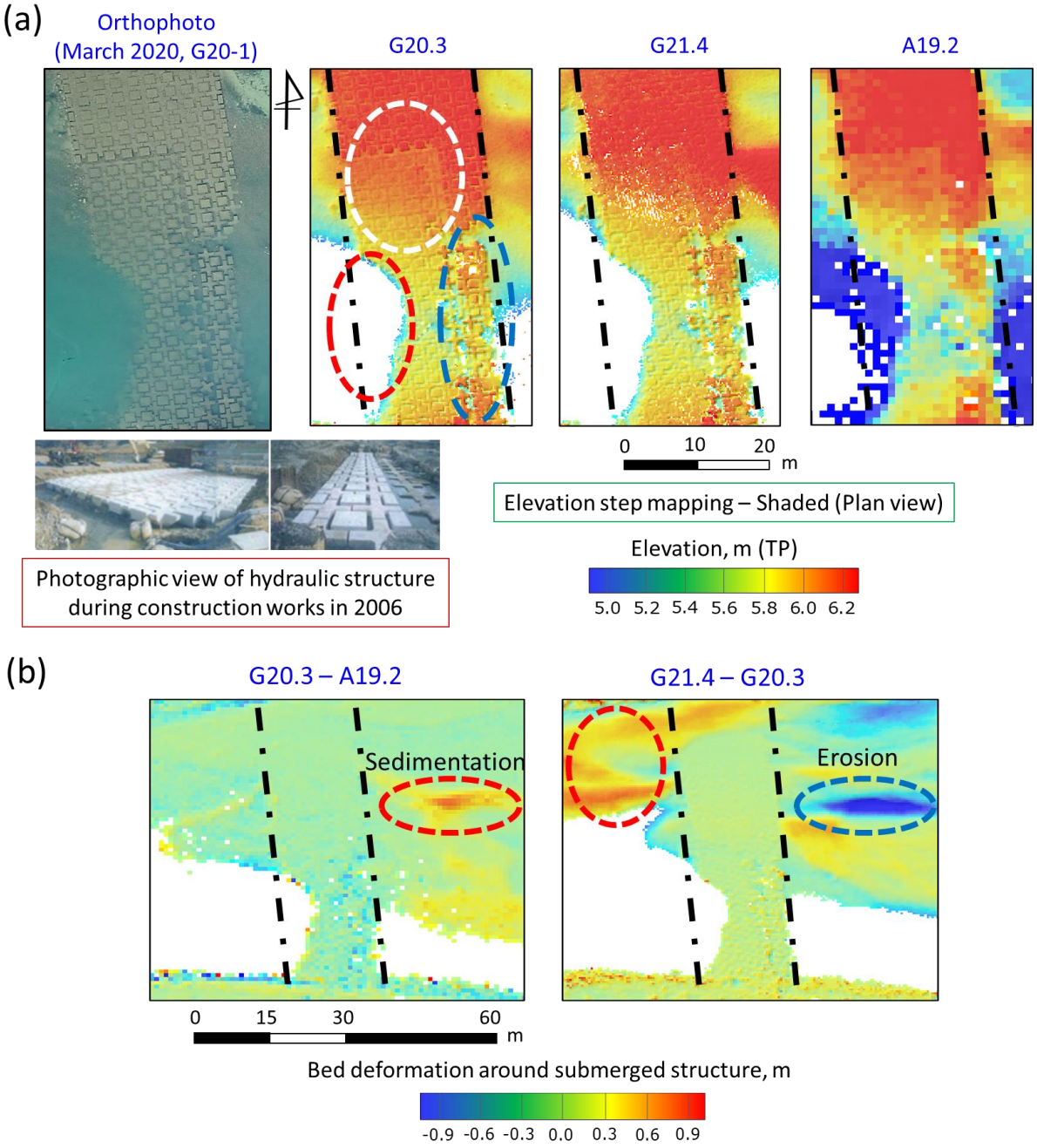

Figure 2.10 (a) Elevation mapping of hydraulic infrastructure and (b) deformation of its surrounding riverbed using LiDAR returns. The black-dotted enclosure represents the original area of the artificial object during construction.

The study also observed the following three structural consequences based on step mapping (G20.3) and aerial image analyses (Figure 2.10a). First, although the structure might have had a usual sloppy pattern during construction, the white-dotted area demonstrates such a unique phenomenon indicating that the object has begun to move or displace from its original position, most likely because of landslides. Then the blue-dotted areas represent a few blocks that have already fallen randomly. Finally, the red-dotted regions indicate that the hydraulic structure has been damaged severely (i.e., white areas showing missing data of deeper waters inside the black-dotted enclosure). Such structural damage might also be attributed to the recent catastrophic flood in July 2018, which recorded a peak flow rate of around 4500 m^3/s (Yoshida et al., 2021). Furthermore, despite the higher water turbidity in the G21.4 measure, the current infrastructure patterns were reasonably confirmed, indicating that the more recent minor flood in July 2020 induced no significant failure to the targeted object. For comparison with GLS findings, the study presented the hydraulic structure using A19.2 point clouds, revealing that the current status of the target was not visualized because of the airborne technique's non-uniform point density. Furthermore, Figure 2.10b captures riverbed changes around the targeted structure using the LiDAR point clouds. Using the differences in G20.3 and A19.2 returns, the results ascertained that the surrounding areas were nearly identical between the two campaigns, except for a few sections deposited (red-dotted) with bed materials at the upper end of the structure (Figure 2.10b, left). In contrast, using the differences between the G21.4 and G20.3 point clouds, the severe scouring at the upper back (blue-dotted) and deposition at the lower end (red-dotted) were shown to result from minor flooding between the targeted surveys (Figure 2.10b, right). Based on the findings, the new advanced GLS was functional in identifying the specifics of river

submerged structure and its surrounding deformation, which will be useful for ongoing river engineering maintenance tasks intended for preventing hydraulic structural failure.

2.4.1.3 Comparison of STIV-derived velocities with flow model estimates

Figure 2.11a depicts contour mapping of model estimates of depth-averaged resultant flow velocity (left) and flow vectors (right) using processed DTMs from the G20.3 and G21.4 measures.

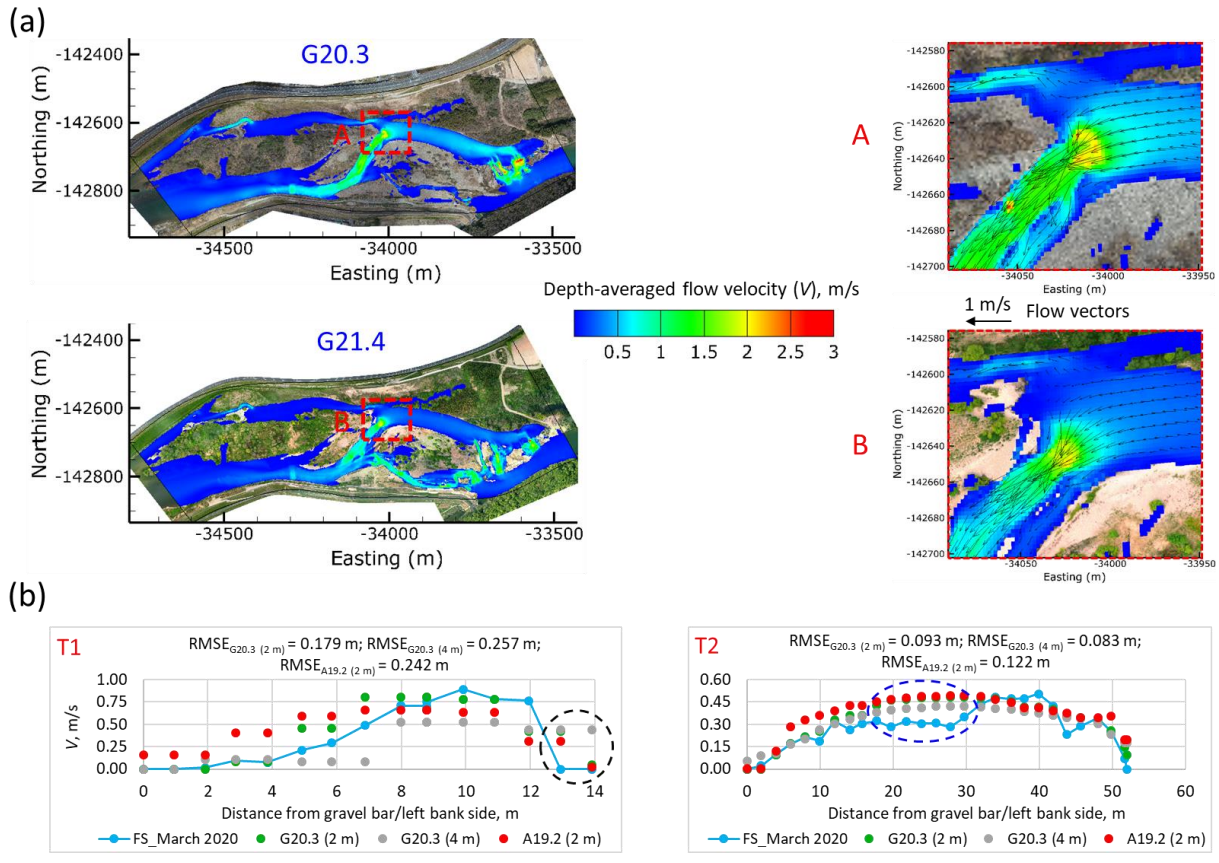

Figure 2.11 (a) Depth-averaged flow velocity distribution using GLS-derived DTMs in finer mesh (2 m)-based hydrodynamic modeling, and (b) comparison of observed flow velocities (*V*) with the respective modeled data along the two cross-streams locally surveyed.

Such spatial representations using seasonal GLS data can have important implications for elucidating how streamflow velocities are distributed in larger cross-sections over changing periods. Furthermore, to validate the spatial distributions of simulated velocities, Figure 2.11b compares numerical estimates and field measures, demonstrating that the modeled data were closer to the benchmarked observations, except for a few points at the right end (i.e., black-dotted areas in T1 section) because of the mislabeled DTMs in steep sloppy and vegetated areas described earlier and also at the central part (i.e., blue-dotted areas in T2 section), which might be attributable to field survey errors caused by the use of digital current meters in deeper water. In terms of estimated RMSEs, comparison of the results of depth-averaged velocities verified that the 2 m mesh-based simulation was more effective than the 4 m estimates, especially when using GLS data versus the referenced ALB data.

Furthermore, the present study estimated surface flow velocities for areas with shallower (S1 and S2 sections), deeper (S3 and S5), and higher flows with partially submerged vegetation (S4) using aerial vertical shooting with deep-learning automated STIV analysis (Figure 2.12a). Figure 2.12b presents comparison of STIV-converted depth-averaged estimates (i.e., STIV*0.85) to a digital current meter (S1 section) and model (S2–S5 sections)-derived velocities for the specific cross-streams. As described herein, considering convenience and safety concerns, field observations were merely conducted along a local cross-section in shallower water (S1) to validate STIV analysis results because surveying in deeper and higher streamflow areas is always dangerous.

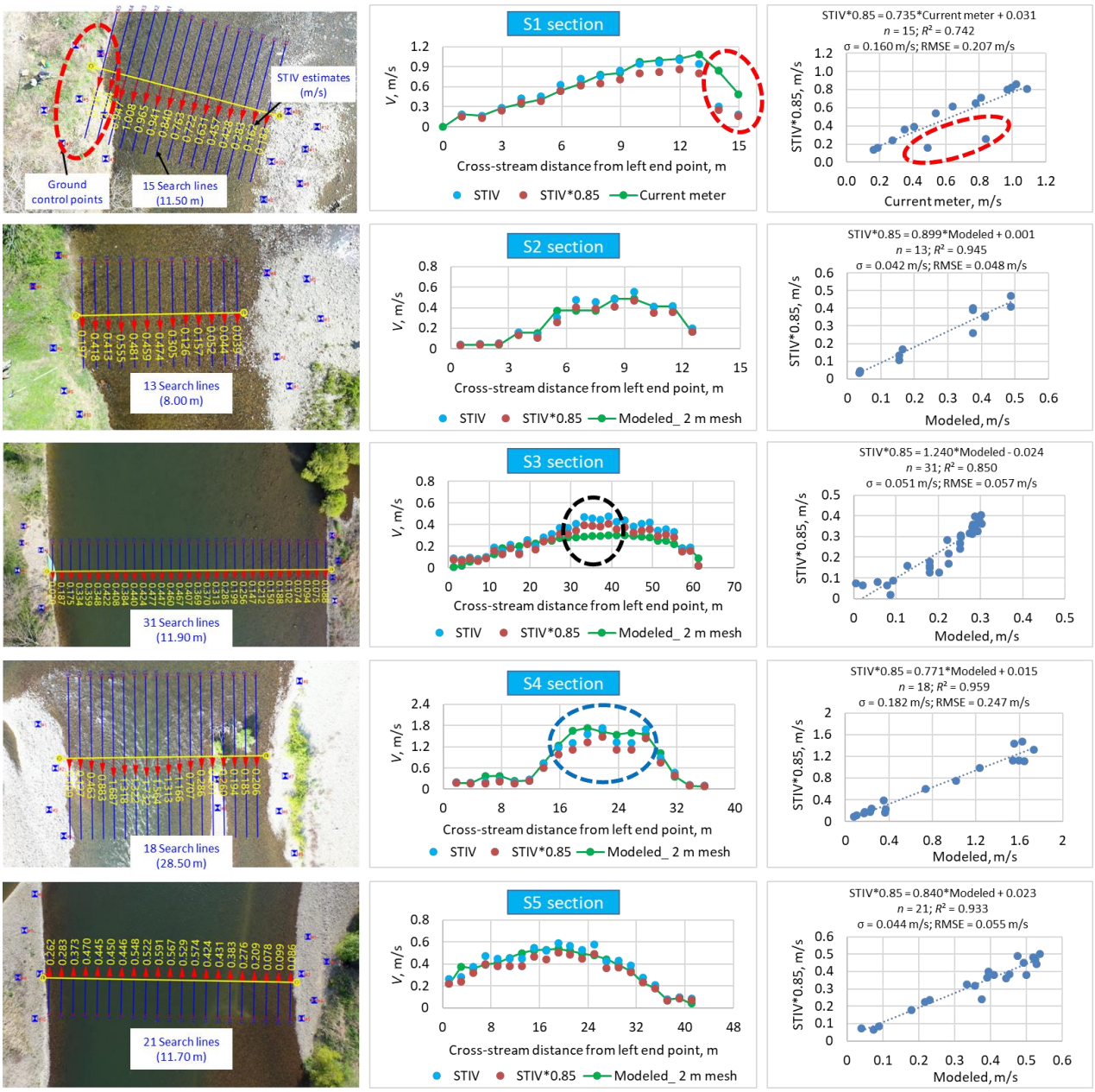

Figure 2.12 (a) Velocity vectors (red arrows) with estimated surface flow velocities (m/s; yellow) over the specified search lines (blue lines) parallel to the main flow direction generated by deep learning-based STIV within captured frames, (b) comparison of STIV estimates with local measurements and flow modeled data along the targeted cross-streams from left to right, and (c) accuracy valuation of STIV-derived flow velocities inferred from results of linear regression.

Furthermore, the study did not perform hydrodynamic-numerical simulation for the specific section of S1 because it was shot one month earlier than the other four targeted sections, and there was no downstream boundary condition (water level) data for numerical modeling during that period. Moreover, STIV analysis revealed a complicated flow pattern for the S4 section at approximately 22–26 m (blue-dotted part; Figure 2.12b), as confirmed by the earlier illustration of flow velocity vectors from 2-D modeling using the G21.4 dataset (Figure 2.11a; B section).

The accuracy of depth-averaged estimates from STIV*0.85 was assessed using linear regression (Figure 2.12c). STIV-analyzed results compared to modeled data revealed strong agreement (R^2 = 0.850–0.959) and regression lines with slopes of approximately one for the most-targeted cross-stream sections. The model comparisons also revealed that the estimated RMSEs were 0.048–0.057 m/s, except for section S4 (0.247 m/s), although this specific section demonstrated better goodness-of-fit (R^2 = 0.959) than other sections. The higher RMSE is probably attributable to the imaging approach considering the partially submerged vegetation condition during flow estimation, whereas the flow model only used the riverbed elevation as input despite the presence of vegetation. Furthermore, comparison to the current meter measures showed that imaging analysis for the S1 section greatly underestimated the velocities for the last two searching lines 14 and 15 (red-dotted part), leading to poor agreement (R^2 = 0.742) with an estimated RMSE value of 0.160 m/s. Such an underestimation in the S1 section resulted from the fact that significant portions of the specific searching lines (14 and 15) of 11.50 m length were marked on the ground surface during STIV analysis. In addition to the S1 transect, the S3 yielded poorer goodness-of-fit (R^2 = 0.850; Figure 2.12c) for a few points when

compared to the other three sections (S2, S4 and S5) findings because STIV overestimated the model values at a distance of approximately 30–40 m for the specific section (black-dotted part; Figure 2.12b). This variation is most likely because STIV estimates velocities based on user-defined parallel search lines to the main flow direction, whereas the hydrodynamic model simulates depth-averaged values using actual flow vectors. Figure 2.13 shows, using the S4 section as an example, how the current imaging technique estimates surface velocities for defined searching lines while taking the average slope of line patterns into account (i.e., yellow lines towards the lower right corner).

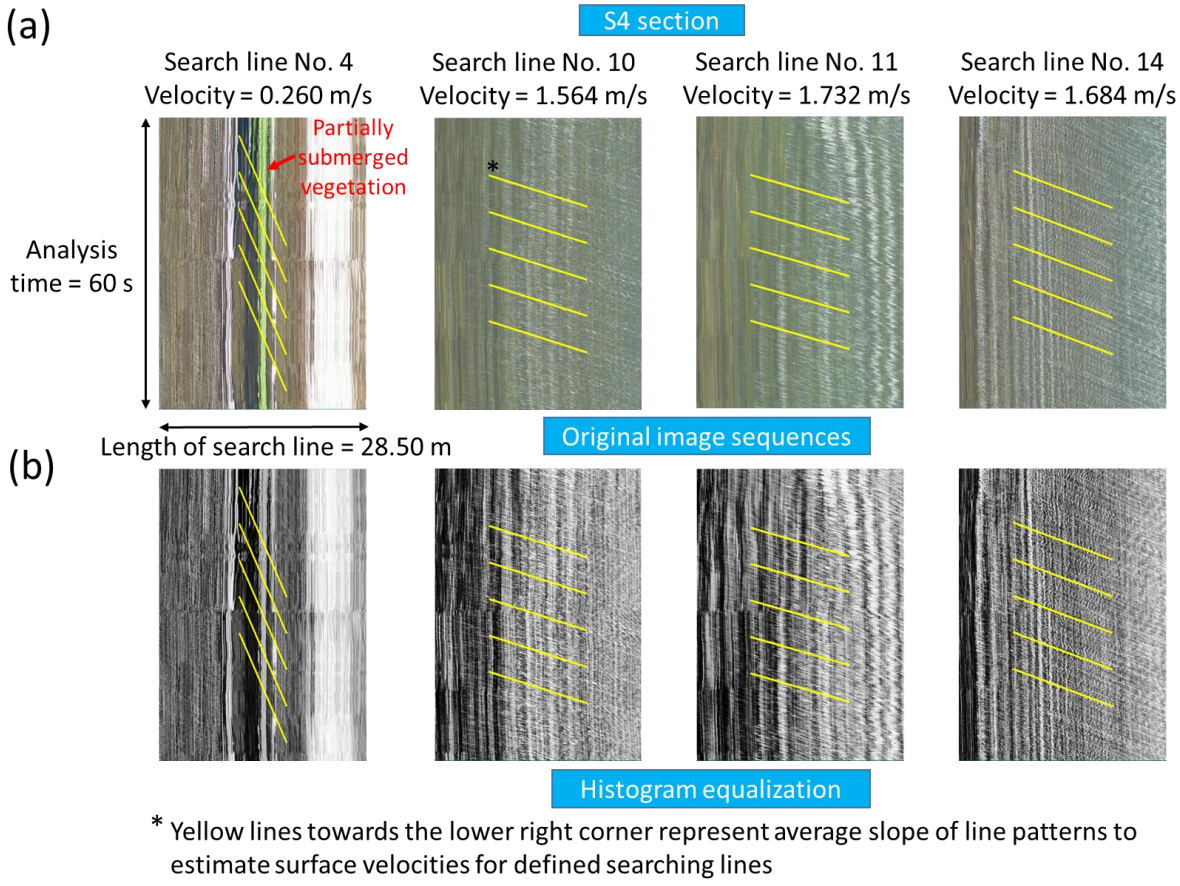

Figure 2.13 Space-time images (STIs) obtained (a) from original image sequences and (b) with histogram equalization for defined searching lines in S4 section as an example.

Furthermore, the searching line lengths were 8.00 to 11.90 m, except for the S4 (28.50 m) because of the presence of partially submerged woody vegetation. Because of the obstacles in the targeted area, such a long length was necessary for imaging analysis, which would serve as a reference for future research. Overall, it was inferred that the current STIV method can produce good results, except for a few points that produced overestimations or underestimations, which could then be adjusted by application of manual correction after varying the length of searching lines. In addition, the deep-learning-based estimations reasonably validate depth-averaged hydrodynamic-numerical model-based findings (and vice versa) without the need for any manual adjustment of a line pattern gradient for a specific cross-section, whereas other conventional imaging techniques (Fujita et al., 2019; Yoshida et al., 2020b) might yield anomalous values and might require frequent manual corrections. Finally, because the deep learning approach provides faster calculations than the traditional imaging method while maintaining higher accuracy, the current STIV can be used for real-time river flow measurements.

2.4.1.4 Remotely sensed river discharges versus model estimates

The study used STIV-estimated velocities and LiDAR-derived water depths to estimate the incremental discharges in the targeted sites at the time these UAV-based datasets were collected. The remotely sensed water depths were calculated by distinguishing between the water surface and riverbed returns, retrieving spatial information where the two sorts of returns coincided, and subtracting the riverbed height from the constant water level. The workflows of the methodology used to estimate non-contact river discharges for this study are depicted in Figure 2.14.

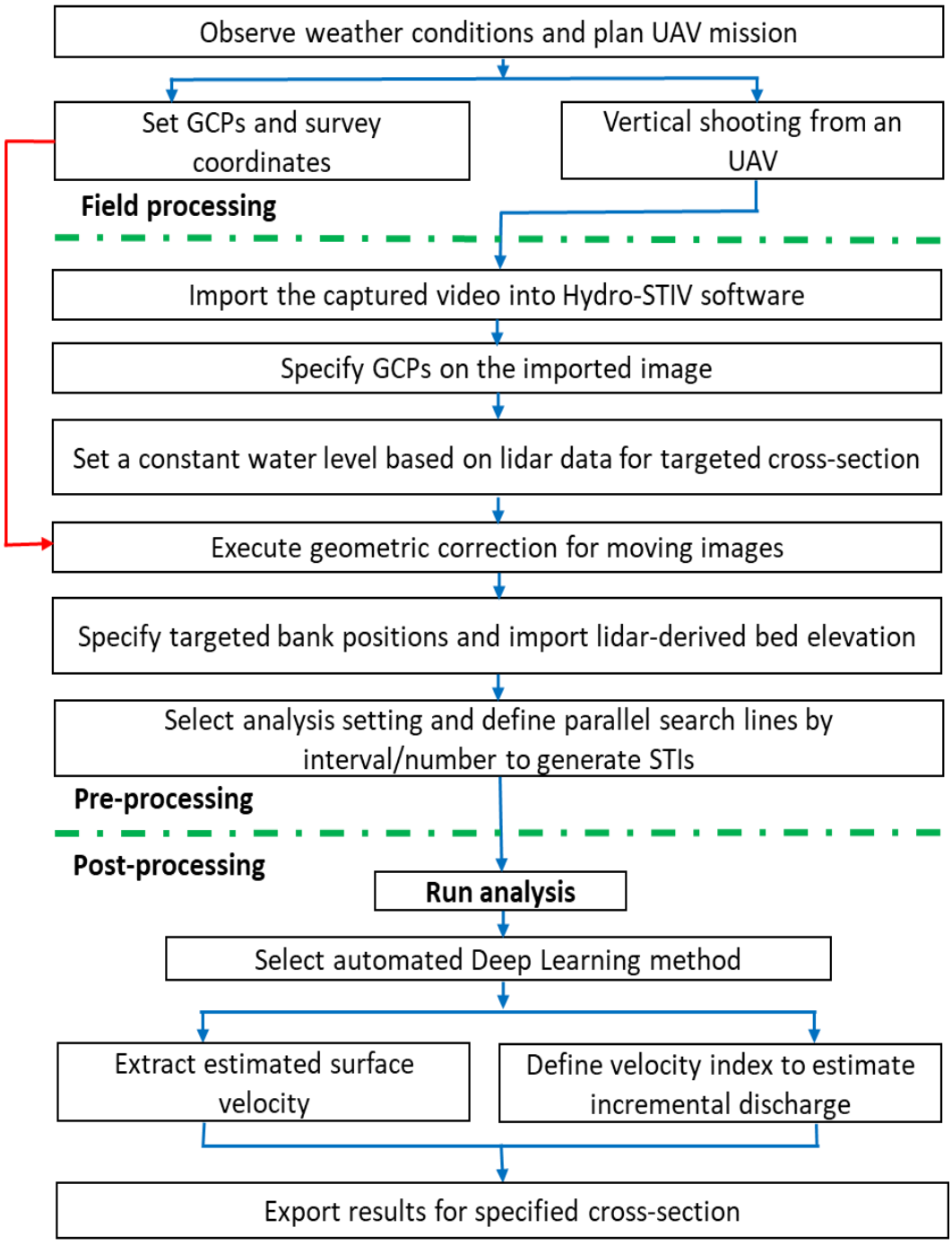

Figure 2.14 Schematic overview of the methodology used to estimate non-contact incremental river discharges (GCPs, ground control points; STIs, space–time images).

Figure 2.15 shows how STIV estimates of surface flow velocities and GLS-derived depths varied from left to right end across the specific channels. The dotted line in

the figure also represents the left and right corners of each vertical as estimated discharge increments. Results from the figure showing surface flow velocities were converted to depth-averaged values (STIV*0.85) using the typical conversion factor of 0.85 (*e.g.,* Rantz et al., 1982) to calculate incremental discharge. Furthermore, the illustrations showed clearly that, because both the water depth and flow velocity increase with distance from the left end, a large proportion of the streamflow volume inside the channels was nearer to the right bank, except for section S5.

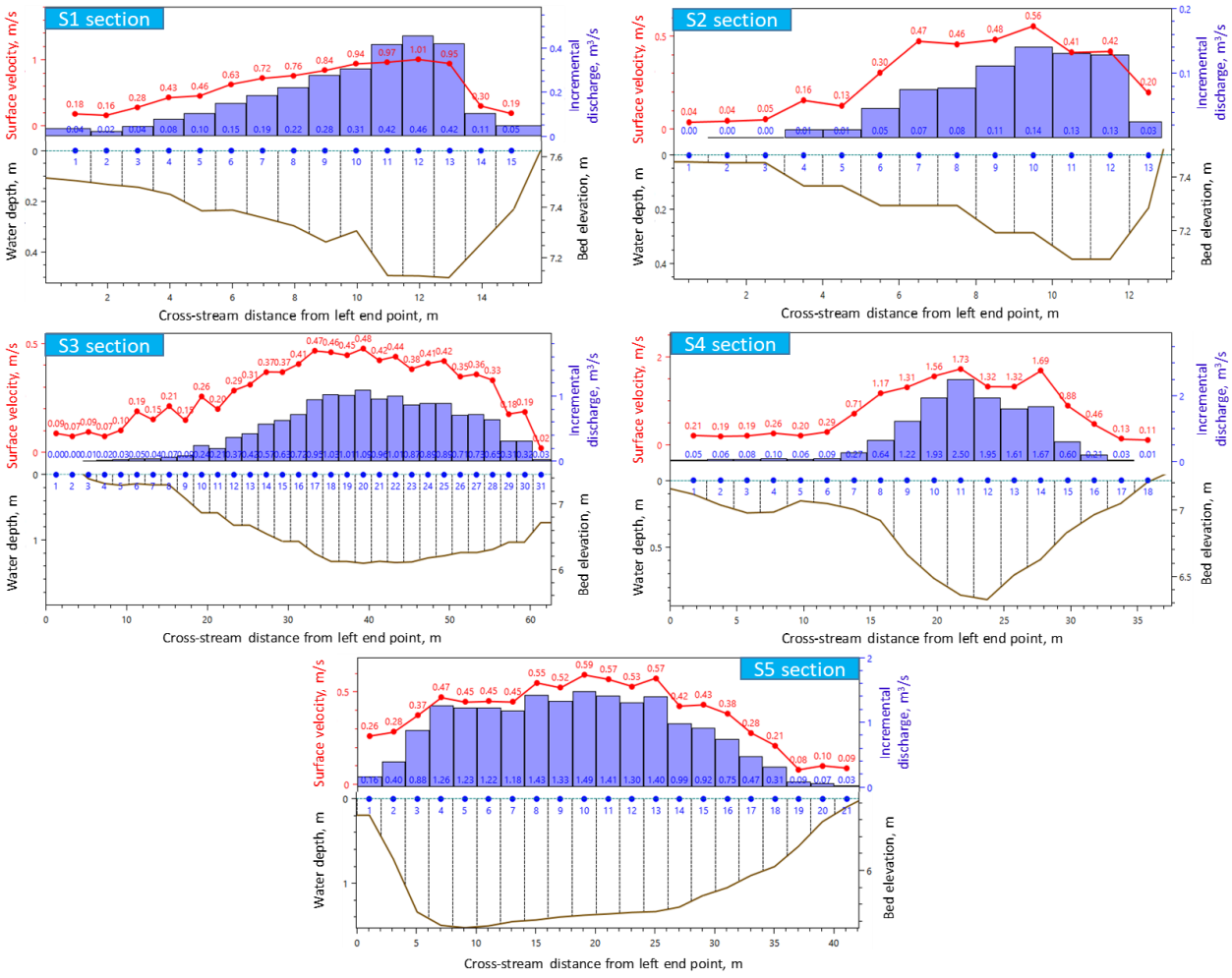

Figure 2.15 Depiction of STIV estimates, GLS-derived bed elevation and water depths used to calculate incremental discharge for targeted cross-streams.

The total discharge for each transect was calculated by adding the discharge increments which occurred laterally across the particular channel, as presented in Table 2.5. In section S1, it was described that the remotely sensed approach underestimated the discharge by around 15% relative to the ground-truth estimates. The disparity in all discharges for the shallower first section was partly attributable to the imaging analyses' marked underestimation of surface flow velocities along the last two searching lines, as described earlier in section 2.4.1.3. It might also be attributable to errors in local surveys. In contrast, compared to flow model estimates, the remotely sensed discharges were overestimated by approximately 1–11%, except for section S5, which was underestimated by about 4%.

Table 2.5 Hydraulic quantities estimated using remotely sensed data in space–time image velocimetry (STIV), corresponding field measures, and flow model estimates for specified cross-streams on the lower Asahi River in Japan

Hydraulic quantities		**Cross-streams**				
		S1	**S2**	**S3**	**S4**	**S5**
Mean depth-averaged velocity (m/s)	STIV*0.85	0.50	0.24	0.23	0.68	0.33
	Field	0.56	-	-	-	-
	Modeled (2 m mesh)	-	0.26	0.21	0.82	0.36
Total discharge (m^3/s)	STIV*0.85	2.88	0.76	14.91	13.06	18.31
	Field	3.38	-	-	-	-
	Modeled (2 m mesh)	-	0.72	13.42	13.03	19.02

Furthermore, because the total cross-sectional flow volume passing through the S3 channel was divided into two paths (S2 and S4), summing the remotely sensed discharge increments laterally across those two distributaries caused a total discharge

of 13.82 m^3/s, which reasonably supports the main channel estimate (14.91 m^3/s). In addition, combining the discharges passing through the cross-streams of S2 and S5 yields a total of 19.07 m^3/s (Table 2.5) flowing through the entire targeted domain, which was closer to the upstream boundary discharge (19.67 m^3/s) of numerical modeling (Table 2.4). Therefore, the incremental discharges calculated from entirely remotely sensed datasets were reasonably consistent with field measures and model estimates, except for a few points that were overestimated or underestimated because a referenced value was used for the velocity conversion index and for considering the constant water level from GLS data. That referred value affected the cross-sectional flow volume considerably. Table 2.5 also shows that the STIV-derived mean depth-averaged velocity for the S4 transect was 17% lower than the model estimate, whereas the imaging technique showed excellent performance for the other studied sections. This variation resulted from a longer searching length for all the lines considered in STIV analysis for the specific cross-stream with partially submerged woody vegetation at the left end. The finding of underestimation implies that longer search lengths should be designated for obstacle parts, except for other lines of remaining common areas where a shorter length can be considered for more reasonable estimation. Overall, comparisons of river discharge estimates demonstrate that the hydraulic quantities derived by GLS and STIV approaches can be reliable as input and validation in hydrodynamic models.

2.4.1.5 Uncertainties in remotely sensed hydraulic quantities

The STIV findings are typically based on a uniform grid of velocity vectors with spacing determined using step size parameters set by the user. Such consistent sampling might result in a spatially varying profile of flow velocities. Despite such apparent benefit, one important shortcoming of the recent approach is that it only

generates surface flow velocities, which must be transformed to depth-averaged values before streamflow rate calculation. However, this limitation applies to any image-based or surface-based velocity appraisal approach. This conversion is usually accomplished by multiplying the STIV estimates by a factor of less than one. In such a way, it yielded imaging-based velocities for the Asahi River targeted cross-sections within an acceptable range of the reference measurements (*i.e.,* current meter-based) and flow modeled data gathered along specified transects (Figure 2.12). The present study used the foremost typical velocity index of 0.85 (*e.g.,* Rantz et al., 1982), but a slightly higher value would have offered better correspondence between the STIV and benchmarked estimates. Using a constant factor of 0.85 underestimation for most depth-averaged velocities led to findings of positive intercepts for the regression equations in Figure 2.12c, indicating that the STIV-derived estimates were biased relative to the other reference quantities. Although the present findings were nearly identical to the standards, underestimating depth-averaged velocities might engender uncertainty in remotely sensed incremental river discharge calculation. In general, the conversion index is affected by the flow field's vertical structure. The index differs between rivers and even spatially within a single reach. For instance, in a recent survey, Legleiter et al. (2017) used velocity conversion factors of 0.82–0.93 to estimate reliable discharge using multiple image sequences within five rivers. Therefore, any hydraulic quantity estimates derived from remotely sensed information might contain multiplicative uncertainty because of the index's variability.

Furthermore, bias in LiDAR bathymetry or a constant water level used as an input in the STIV software might also cause the remotely sensed river discharge to be

overstated or understated. When comparing GLS bathymetry to benchmarked measures, one source of uncertainty was the riverbed characteristics. Although the channel bed was mainly sand with numerous gravel bars, there were some submerged and lodged plants and dense floodplain vegetation. In such a case, some laser pulses might be bounced off the surface of the substrate (gravel bars, vegetation canopies, etc.). In addition, in local surveys, measuring rods are more likely to be placed at possible lower elevations within the bed materials or any plants' base. Consequently, unfiltered LiDAR data might be expected to underestimate river bathymetry in comparison to results obtained from local surveys. Furthermore, rather than directly capturing water depth, GLS computes it by comparing the distance between the water surface and the riverbed, as defined by the distance of the laser pulses back to the scanner. Any deviation in determining the water surface's position can be expected to influence the depth estimate. However, the current GLS can reasonably distinguish between the water surface and riverbed returns, which is usually complicated for traditional bathymetric LiDARs (*e.g.,* Kinzel et al., 2007), particularly in shallow areas. Overall, such practical issues must be considered when remotely estimating hydraulic quantities.

2.4.2 Floodplain vegetation attribute appraisal

2.4.2.1 LiDAR-based LCC mapping and normalized confusion matrices

Figure 2.16a portrays the LCC for the targeted domain, specifically the spatial distribution of riparian vegetation species, using GLS-based processed attributes. Such LiDAR-derived features from no-leaf (G20.3) and leaf-on (G20.10 and G21.4) campaigns particularly include positional data (X, Y, and Z), DCM values, reflection

intensity counted from DTM (INT_DTM), voxel-based criterion (*i.e.,* Under % = (VOX_CNT50/VOX_CNT) x 100; see Figure 2.4a), and slope of the vegetation canopy surface (Figure 2.17).

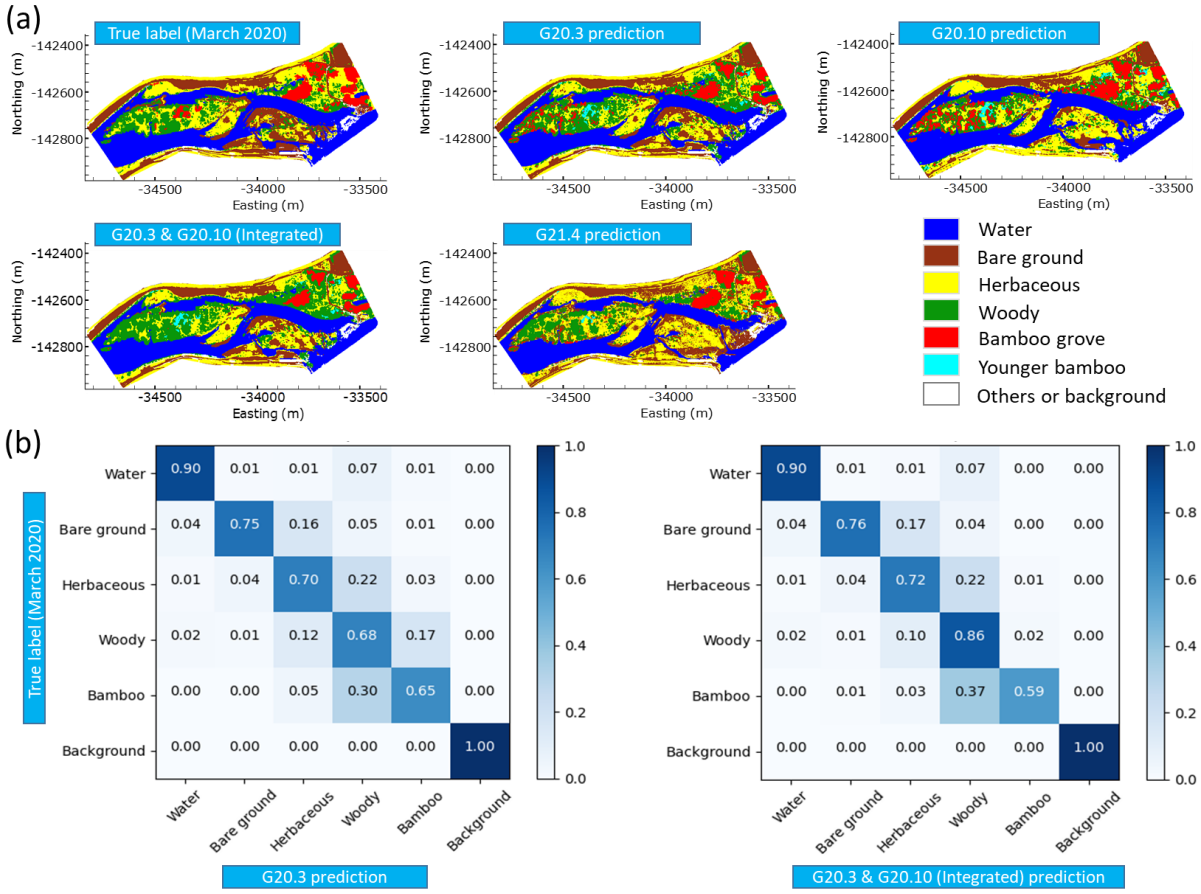

Figure 2.16 (a) Land cover classification (LCC) using data-filtered elements from UAV-borne GLS measures, and (b) normalized confusion matrix of GLS-based LCC prediction versus the respective ground-truth evidence-based true label.

Aside from LiDAR data, the study considered color-coded attributes (red–green–blue), particularly for GLS-derived missing data in deeper waters and distinguishing water regions from bare ground areas precisely. The LCC mapping derived from a single G20.3 campaign (Figure 2.16a) was validated using pixel-based normalized confusion

matrix (Figure 2.16b, left) calculated by comparing GLS-based prediction to referenced true label mapping, as shown in Figure 2.16a.

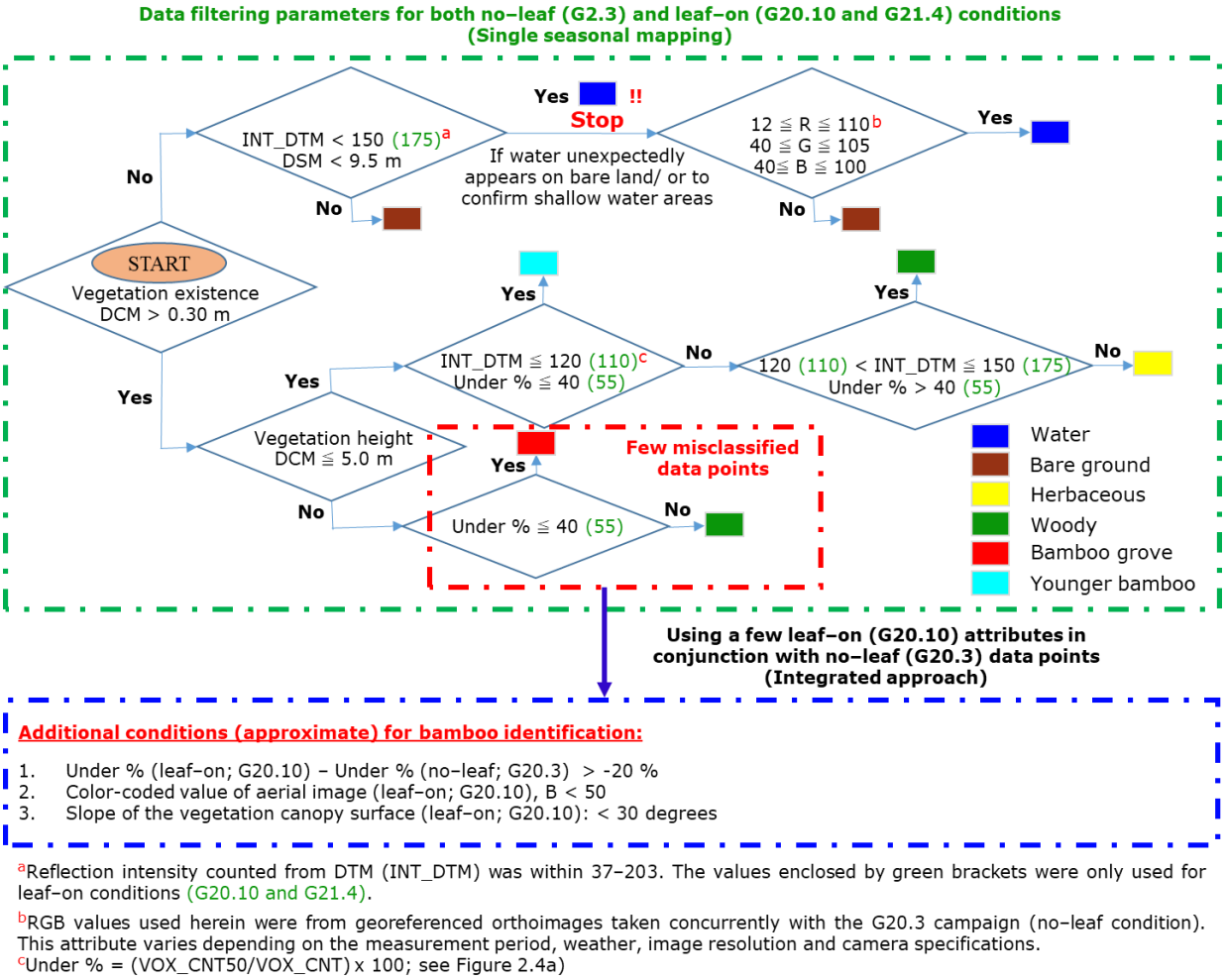

[a]Reflection intensity counted from DTM (INT_DTM) was within 37–203. The values enclosed by green brackets were only used for leaf–on conditions (G20.10 and G21.4).

[b]RGB values used herein were from georeferenced orthoimages taken concurrently with the G20.3 campaign (no–leaf condition). This attribute varies depending on the measurement period, weather, image resolution and camera specifications.

[c]Under % = (VOX_CNT50/VOX_CNT) x 100; see Figure 2.4a)

Figure 2.17 Proposed algorithms for GLS-based LCC mapping.

Furthermore, the other two individual LCC mapping for different seasonal leaf–dressed (G20.10 and G21.4) campaigns were evaluated qualitatively based on their orthophotos and field observations. During qualitative assessment, it was revealed that the dominant areas of woody and bamboo species on the leaf-on LCC mappings were reasonably matched with standard, although the true label was prepared using other different seasonal (no-leaf) information. By contrast, other attributes, such as

water, bare ground, and herbaceous species, differed slightly from the referenced mapping, although those labels were compatible with their respective high spatial resolution aerial images captured concurrently during GLS surveys. This marginal variation can be attributed to different water flow conditions, vegetation wash-out caused by minor flooding between targeted GLS measures, herbaceous species growth and decay over time, and the removal of a few sections of the bamboo grove upstream for river management tasks.

Findings from the G20.3 prediction revealed that the dominant bamboo trees in the targeted domain were classified as reasonably accurate (65%), whereas 30% got to the class of woody species (Figure 2.16b, left). It is worth noting that, although the proposed methodology identified the younger bamboo trees, the study merged that type of vegetation with the bamboo groves for the accuracy evaluation compared to true label mapping. Furthermore, the classification demonstrated that most dominant woody species were labeled with accuracy of 68%, whereas some of their patches were classified by bamboo (17%) and 12% by herbaceous species. This bamboo-misclassified area can be attributed to new woody vegetation species coexisting with older patches that appear to be bamboo species. It was also noticed during the ground-truth survey that the woody vegetation in the targeted floodplain did not always stand straight with a single main stem, with larger branches growing low and isolated from the tree's main stem. In addition, overhanging woody vegetation parts were misjudged as bamboo trees. Consequently, in such cases, the behavior of voxel-based parameters for woody species might be nearly identical to that of bamboo trees. Furthermore, woody species mislabeled 22% of herbaceous species (Figure 2.16b, left). Regarding the differentiation between younger woody vegetation and

herbs, the present study proposed a methodology with up to 5.0 m of DCM values (Figure 2.17). In this case, the voxel criteria for both species were identical. It was challenging to differentiate between those species with such a particular condition during true label mapping. In addition, 16% of bare ground areas were attributed to the class of herbaceous species (Figure 2.16b, left). From the LCC workflows (Figure 2.17), it was noticed that a DCM value of 0.3 m was set to distinguish bare ground from herbs, whereas, in true label mapping, it is more difficult to distinguish bare ground from these species using only human vision and field visits. Therefore, because of such uncertainty, mislabeling of bare ground as herbaceous is a common occurrence in true label mapping. However, minor misclassified data points might have a negligible effect on estimation of spatially distributed vegetation roughness coefficients in hydrodynamics or flood modeling. Additionally, it was strongly evident that OA of around 77% was obtained for the individual G20.3 measure, except for background parts, which might be attributed to good LiDAR returns in no-leaf conditions.

Ultimately, this study proposed a novel integrated approach (Figure 2.17) to minimize the misclassified data points in the G20.3 measure between woody and bamboo species. The new combined method primarily considered data filtering parameters used for the individual earlier G20.3-based classification (winter, no-leaf condition), as well as a few processed attributes of the G20.10 measure (autumn, leaf-on condition). Because the integrated method's water, bare ground, and herbaceous labels were nearly identical to those of the G20.3-based classification, the OA of the new technique was compared to the true label prepared for the G20.3 campaign. Finally, the accuracy of the woody class was improved by 18%, with areas mislabeled

as bamboo species reduced from 17% to 2%. By contrast, the bamboo-labeled accuracy was slightly lower than in the previous no-leaf-based approach (Figure 2.16b, right). This decrease in accuracy after combination with the G20.10 dataset can be attributed to the difficulty in identifying a few bamboo trees visualized in woody-dominant areas by the earlier no-leaf campaign. Consequently, the winter survey would be preferred over the other seasonal datasets for distinguishing bamboo from densely wooded vegetation. Compared to the earlier single seasonal measure, the integrated method's overall performance was improved by 3% (Figure 2.16b). Although the OA of the proposed methodologies might be affected because of a few uncertainties in the true label considered herein, single-seasonal or multi-seasonal GLS-based attributes with such a consistent trend can be practical for floodplain vegetation classification.

A report of an earlier study (Geerling et al., 2007) labeled riparian vegetation species into five classes using airborne LiDAR data, demonstrating that the OA was inadequate at 41%, although their performance was improved to 81% by combining compact airborne spectrographic imager information and LiDAR data. Furthermore, researchers in a recent study (Yoshida et al., 2020a) used ALB-derived characters (e.g., voxel-based laser points and estimated vegetation heights) to perform LCCs for the river explored here. Their results qualitatively revealed that some terrestrial areas were misclassified as water bodies, thus contradicting their respective high-resolution aerial images. They also had difficulty distinguishing between the dominant bamboo forests and woody species, which could impact their hydrodynamic-numerical simulations that consider the effects of floodplain vegetation conditions. Under such perspectives, the proposed method of relying solely on current GLS-based attributes

has primarily overcome the challenges identified in previous studies. Therefore, the workflows proposed herein, particularly for vegetated rivers in Japan, are expected to be an efficient method of classifying vegetation species that are important in predicting hydraulic roughness, namely, woody and bamboo groves. Furthermore, this novel measure can be used globally after varying the weights of the suggested parameters based on GLS-based measurement conditions and existing vegetation species for a specific floodplain.

2.4.2.2 Riparian vegetation structural changes assessment

Multi-seasonal GLS-based LCC mappings (Figure 2.16a) revealed that bamboo and woody (i.e., willow) species dominate the vegetation upstream and downstream of the study site, respectively. Therefore, proper assessment and management of such species are significant in governing river flows during potential floods. Consequently, in addition to LCC mappings, accurately evaluating the vertical structure and estimating the heights of riparian vegetation is of crucial importance not only for ecological studies but also for hydrodynamic modeling of vegetated rivers, as it is one of the critical characteristics from which roughness (flow resistance) parameters in hydrodynamic models are derived (Straatsma & Middelkoop, 2006). Because vegetation attributes vary spatially and change over time, detailed and up-to-date information is required to define the roughness of hydrodynamic modeling and implement practical river management actions. Based on these perspectives, the current study identifies structural changes and the rate of riparian vegetation growth between the targeted GLS campaigns.

Figure 2.18a characterizes the vertical structures of woody vegetation at around 15.2 KP (right bank) using different seasonal GLS point clouds.

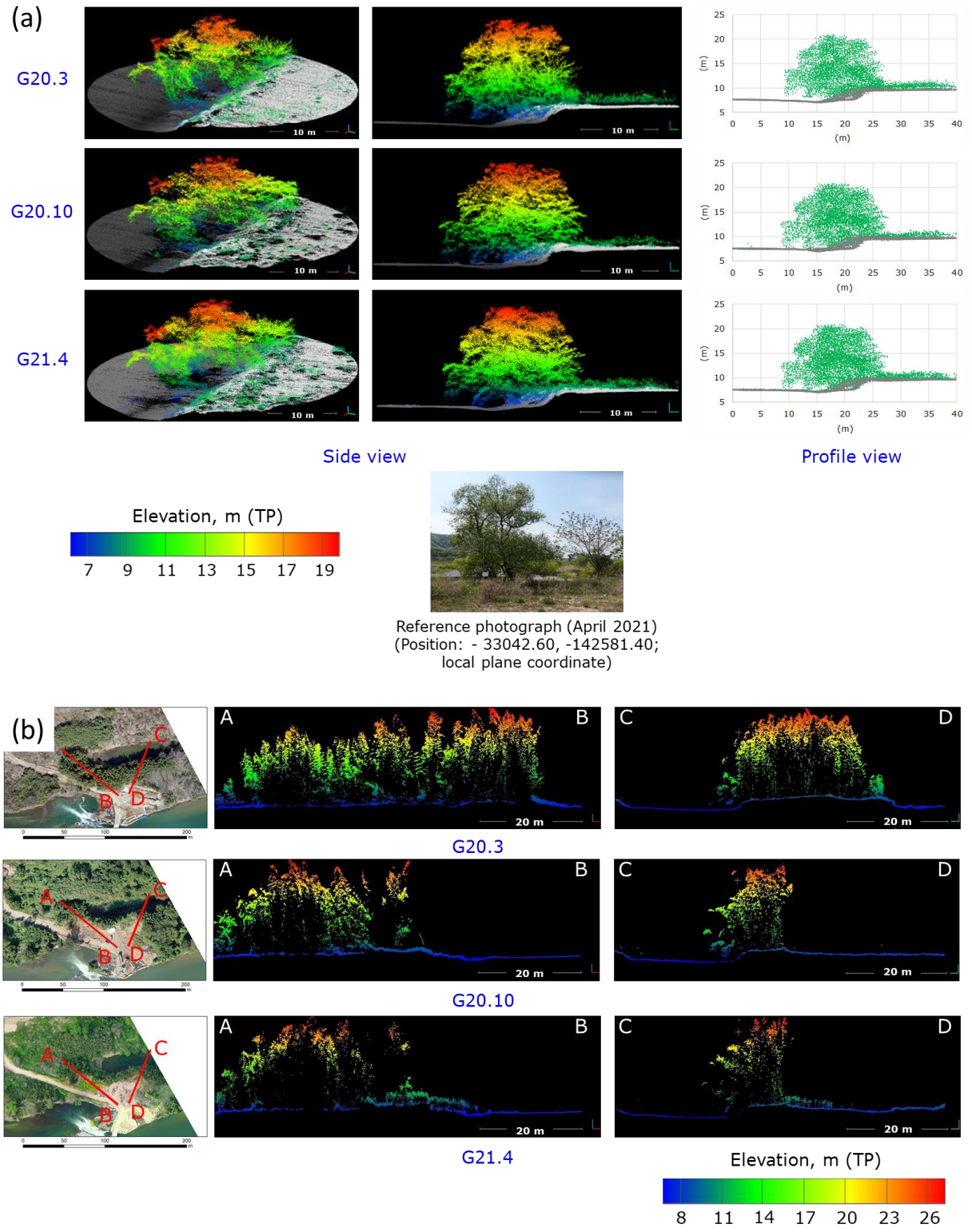

Figure 2.18 (a) Side and profile views of individual woody vegetation using GLS returns; (b) confirmation of vegetation overgrowth and artificial cut-down for river management work.

The side and profile views were reasonably confirmed using a local photograph taken during the most recent GLS campaign in April 2021. Such an illustration represents the structural changes in the tree canopy during no–leaf (G20.3) and leaf–on (G20.10 and G21.4) states, which may be used to derive changes in floodplain roughness for hydrodynamic–numerical modeling. Furthermore, the aerial photograph taken during the G20.3 survey shows that the bamboo forest was thriving on the right bank around 15.8 KP (Figure 2.18b, top), whereas the image from the G20.10 campaign presents that part of the bamboo grove had been cut down between the first two LiDAR surveys (Figure 2.18b, middle). Because the point clouds were influential not only on the top surface of the tree canopy, but also on the mid-level and the ground surface underneath the foliage, overgrowth and human-induced cut-down areas could be represented using different LiDAR returns (Figure 2.18b).

Since vegetation overgrowth near riverbanks affects water levels during floods, such findings from the GLS return will provide crucial information on the current status and challenges, especially in inaccessible areas of heavily vegetated rivers, and will be useful for flood management and favorable riverine ecosystems. However, a recent study by Mandlburger et al. (2016) evaluated a UAV-mounted green laser profiler on riparian understory trees structure, presenting that the sensor partially probed the vegetative layers and returned fewer echoes from the floor beneath the canopies. In addition, Yoshida et al. (2020a) used ALB point clouds to show the vertical structure of bamboo groves in the same river studied here, demonstrating that the laser characterized the canopy edge, with little return from the vertical stratum and almost none from the grounds below the tree canopy, even when the leaves were off.

2.4.2.3 Vegetation growth rate approximation

Figure 2.19a presents spatial mappings of vegetation growth variation over the floodplain studied herein using raster differences of processed DCMs with QGIS Ver.3.16.1 software. The study approximated a variation rate of approximately 1.0–1.5 m per year from vegetation growth mappings that included both no-leaf (G20.3 and A19.2) and leaf-on (G20.10 and G21.4) conditions, particularly for the dominant woody and bamboo species at the study site.

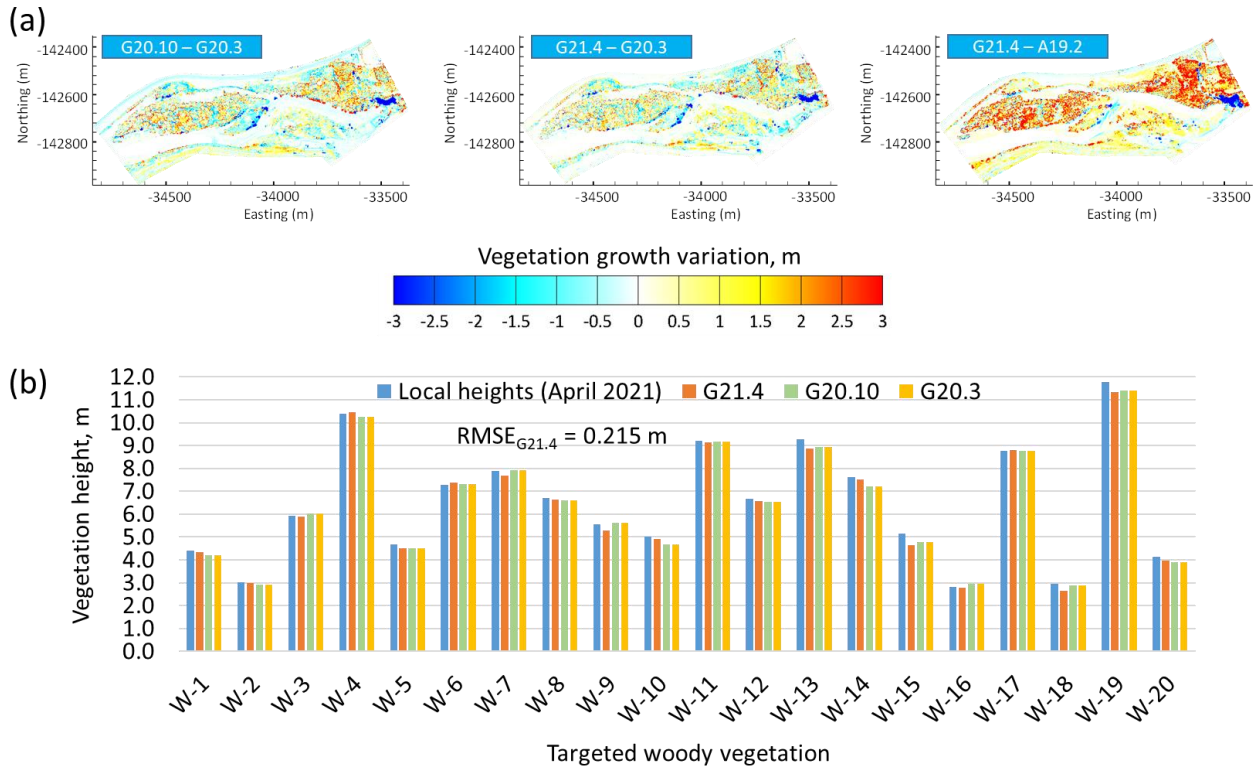

Figure 2.19 (a) Spatial mapping of vegetation growth variation between targeted LiDAR campaigns, and (b) verification of GLS-estimated vegetation heights (color-shaded values from Table 2.6) versus corresponding field measures. TS herein stands for the total station.

In addition to identifying the decay of herbaceous species (light blue parts) over

seasonal changes caused by various environmental factors, their annual growth rates of approximately 0.5–1.0 m were mapped. Because growth variation can be limited by various factors, including soil types, nutrients, bed materials, climatic conditions, flooding events, etc., selecting a single growth rate value for the respective species is complex. Furthermore, negative values in growth mappings (dark blue parts) show the removal of riparian vegetation between targeted surveys, which might be attributable to wash-out conditions during flooding events and for areas that are cut down (as also shown in Figure 2.6a) for river management purposes. The recommended values for vegetation growth rate in this study are expected to be useful for future vegetated riverine research, particularly for the river under consideration here.

Furthermore, Table 2.6 compares the woody vegetation heights surveyed in April 2021 at around 15.2–15.5 KP (Figure 2.1a) with GLS datasets-based estimates. The respective vegetation heights were approximated using buffered approaches (Table 2.6), in addition to the usual technique via TS-based information, because the surveying rod could be inclined during field measurements. Finally, estimations revealed that GLS-based heights were reasonably accurate concerning the TS-surveyed points, whereas the buffered approach of 1 m rather than 10 cm could also be considered due to a few uncertainties in the ground-truth surveys. Furthermore, Figure 2.19b compares locally-surveyed vegetation heights to GLS-estimated reasonable values from the various approaches (Table 2.6; color-shaded estimations), presenting good correspondence between ground-truth measures and GLS estimates with outperforming accuracy. Although this graphical comparison validates the GLS projections, it was unable to verify the growth variation mapping because the estimated heights via multi-seasonal LiDAR measures were compared with only a

single period of field-surveyed data, and the vegetation heights were locally observed at specific canopy points rather than the usual top ends of vegetation for convenience considering comparatively larger sizes.

Table 2.6 Comparison of GLS-based estimates to the local or total station (TS)-surveyed vegetation height. Colored values denote reasonable estimates from particular GLS measure compared to field surveys

No.	Local heights (m) (April 2021)	GLS-based estimates, m								
		TS-based information			Buffered approach					
					10 cm			1 m		
		G20.3	G20.10	G21.4	G20.3	G20.10	G21.4	G20.3	G20.10	G21.4
W-1	4.39	4.16	4.13	4.33	0.02	4.13	0.07	4.16	4.20	4.50
W-2	3.02	2.85	2.93	2.99	1.80	1.13	2.40	2.21	3.52	3.06
W-3	5.94	5.89	6.03	5.91	0.04	0.03	3.74	6.05	6.17	6.32
W-4	10.40	10.43	10.25	10.27	9.99	10.16	10.46	10.76	10.76	11.02
W-5	4.67	4.57	4.50	4.51	0.13	5.34	2.75	5.44	5.34	5.62
W-6	7.29	7.10	7.05	7.03	7.51	7.31	6.74	7.76	7.31	7.37
W-7	7.89	6.78	7.92	7.69	0.08	7.31	6.95	6.80	9.01	8.93
W-8	6.71	6.51	6.56	6.49	6.30	0.04	5.49	6.62	6.59	6.65
W-9	5.55	4.89	5.23	5.17	4.72	5.14	4.16	5.00	5.64	5.27
W-10	5.00	4.60	4.66	4.70	4.16	0.14	4.91	4.73	4.69	4.91
W-11	9.19	9.16	9.01	8.94	8.94	0.12	8.74	9.28	9.16	9.14
W-12	6.67	6.66	6.55	6.57	2.86	9.30	0.10	8.71	9.50	9.48
W-13	9.29	9.00	8.94	8.88	8.84	8.15	8.58	9.18	9.72	10.45
W-14	7.61	7.68	7.20	7.51	6.31	6.02	6.69	7.11	8.22	7.51
W-15	5.15	4.62	4.78	4.65	2.95	3.69	0.09	4.01	4.05	4.41
W-16	2.80	1.24	2.62	2.66	0.13	2.48	0.00	0.65	2.94	2.78
W-17	8.78	8.81	8.77	8.80	6.90	10.41	9.82	9.16	9.57	9.82
W-18	2.96	1.88	2.89	2.63	0.63	3.33	0.67	1.88	4.80	4.32
W-19	11.76	10.11	11.40	11.34	9.90	11.40	10.28	10.11	11.40	10.93
W-20	4.13	3.60	3.91	3.94	3.68	6.38	3.97	3.68	7.80	7.50

However, the G21.4 estimates were, on average, 0.142 m lower than the ground-surveyed data, with an estimated RMSE of 0.215 m. The marginal variation could be attributed to field survey error, most likely due to the irregular pattern of the canopy edges. An earlier report (Yoshida et al., 2020a) compared woody vegetation heights surveyed locally at the same river studied here with those estimated by ALB data (no–leaf condition), presenting that the LiDAR findings were on average about 0.60 m lower than the ground-truth measures, with a maximum error of 1.11 m. Finally, taking into account the shortcomings of earlier studies, it can be revealed that the current GLS would be a viable platform for the characterization of riparian vegetation attributes because it performs almost consistently in all seasons.

2.5 Conclusions and Future Research Directions

This study served as a pilot survey of the feasibility of remotely sensing riverbed deformation, submerged infrastructure, hydraulic quantities (depth, velocities and discharge), and riparian vegetation attributes (types, heights, growth rates and vertical structures) via recent advanced UAV-based LiDAR and imaging velocimetry technologies and also highlighted some key facts for further research. The efficacy of these methodologies was determined by comparing remotely sensed estimates to ground-truth measurements and hydrodynamic model-based results. The experimental GLS confirmed the current state of the hydraulic structure, although the sensor approximated shallow bathymetry of fewer than 2 m attributable to turbid river environments and insufficient laser power. Furthermore, when surface flow velocity estimates from AI-assisted STIV analysis were multiplied by the typical conversion factor of 0.85, they agreed reasonably (R^2 = 0.742–0.959) with estimated RMSEs of 0.048–0.247 m/s in comparison to both current meter measurements and

depth-averaged model-derived calculations. The STIV analysis also showed a complicated flow pattern for one cross-section, which was reasonably confirmed by flow vectors from depth-averaged modeling. The river discharges calculated using remotely sensed velocities and depths at multiple cross-sections were compared to benchmarked field and model estimates, demonstrating that the UAV-based approach produced reasonable quantity to verify upstream boundary discharge required in depth-averaged flow modeling. Therefore, using remotely sensed information to extract river flow as verification data in hydrodynamic–numerical modeling would be a distinctive technique. Using GLS-based data filtering algorithms, the study also classified land cover features with OA of 80%, and approximation of 0.5–1.5 m per year for vegetation growth that varies among species. To conclude, currently used remote sensing techniques can be deemed as cost-effective and well-proven tools for characterizing hydraulic and floodplain vegetation attributes, which will be useful for streamflow simulation and desirable ecosystem management tasks.

Although the LiDAR and imaging systems used in this study fulfilled their primary purpose, further development and testing of both sensors are required before these approaches can be widely applied. For example, to ascertain the potential penetration depth limit via the green LiDAR, it is recommended to hover the UAV at the lowest possible altitude in relatively clear flowing water. Also, the study recommends increasing the LiDAR power and testing its practicability in deeper areas, specifically the missing parts evident herein. Furthermore, because the present research used the image velocimetry approach to monitor on-site streamflow features in normal flow conditions, it is necessary to apply this new technique during flooding events with varying different conditions (*e.g.,* surface waves, obstacles, background shadow

projected on the water surface, light, rain, wind effects, etc.) for widespread use in scientific platforms. Besides, it is essential to examine its accuracy compared with the traditional ADCP and other image velocimetry approaches reported in previous studies to benchmark its performance.

Furthermore, in the current field evaluation, the camera to capture multiple moving image sequences for STIV analysis and the green LiDAR were mounted separately on different UAVs, but this instrumentation setup could be implemented from a common platform in further studies. Such integration would increase the payload's weight and shorten the flight duration, making it only worthwhile if both systems could extract useful information from the same flying altitude. Another common concern that needs to be addressed further is identifying a more reasonable conversion coefficient than the one used here to transform STIV estimates to depth-averaged values before estimating discharge. It is also suggested that the current STIV algorithms be improved to add another distinguishing feature that generates continuous coverage of velocity estimates across the targeted portions of an image rather than a single specific cross-stream. Such improvement may provide users with more functionality when combining velocity findings with other attributes (e.g., bathymetry). Furthermore, the study deployed GCPs in the field to scale the moving images captured for the STIV analysis; however, employing positional and orientation data logged on-board the UAV to instantly georeference would be a more viable approach. Consequently, such an alternative framework might eliminate the need to set GCPs along the river's banks or at specified areas' left and right ends. If in situ geometric coordinates are not required for a specific application, the image-based analysis can be undertaken using only the pixel scale factor. Such a factor can be

defined by employing a laser range finder to detect the length from the UAV to the water's surface and estimating the GSD using the camera's focal length. Ultimately, this option would eliminate the need for hydrographers to collect data in the field, offering them more flexibility. In addition, further advancements in GLS processing algorithms may enable users to visualize the laser point cloud on the ground. Such real-time feedback would confirm that remotely sensed velocity and depth measurements are accurate enough. Furthermore, although the novel frameworks proposed herein to elucidate floodplain vegetation features were successful in their intended purpose, they are suggested to be validated across various vegetated reaches in future studies to become benchmarked methodologies in the relevant fields.

CHAPTER 3

Porous model-based 3-D numerical simulation of floods in river corridor with complex vegetation quantified using airborne LiDAR imagery

3.1 Abstract

Excessive flood flow over the historic diversion weir in the vegetated Asahi River in Okayama Prefecture, Japan, was recently recorded for the first time after its renovation as part of a river improvement project. Fluvial researchers analyzed the diversion discharge for flood mitigation measures through laboratory studies and conventional two-dimensional (2-D) depth-averaged simulations. The existing model was insufficient for simulation of certain phenomena such as flow resistance caused by vegetation branches and leaves and vertical flow distribution the river corridor. Therefore, the present study developed a three-dimensional (3-D) vegetation resistance porous model by estimating topography, land cover, and vegetation distribution from airborne light detection and ranging (LiDAR) topo-bathymetry (ALB) data of the river channel. Afterward, for recent flooding events in 2020 (minor) and 2018 (major), numerical simulations of the 3-D flow around the diversion area were conducted. Findings confirmed that the water level and flow regime at low discharge (2020 flood) agreed well with the referenced 2-D calculations, STIV data, and field measurements. Results show that the flow regime at high discharge (2018 flood) was more reproducible than by 2-D simulations. Furthermore, the proposed model showed a significant advantage over the traditional one by revealing the vertical flow distribution, as well as free surface and near-bed flow fields around the targeted

structure. The 3-D model also demonstrated that changing vegetation distribution had a significant impact on streamlines at both the free-surface and near-bed levels. In contrast, such flow patterns with highlighted vegetation distribution cannot be apparent in 2-D modeling. In addition, the diversion discharge designed using the proposed model is feasible with the current riverbed and vegetation conditions. To summarize, the current results can assist policymakers in developing a balanced and rational scenario for flood control measures that take best vegetation management practices into account around river corridors.

3.2 Introduction

Recent flooding events around the world, as mentioned in Chapter 1, highlight the importance of detailed flood flow modeling that incorporates actual complicated flow regimes under real land cover and is used to prevent devastation through proper river engineering measures. The main river targeted in this study is the vegetated lower Asahi River, Okayama Prefecture, Japan, details of which are described hereinafter, which has had a plan of flood control measures since the 1970s to defend Okayama city through a project of river improvement (Fujikane et al., 2016). The renovation works included strengthening of river dikes, developing a river mouth barrier of a distributary channel, the Hyakken River, and reconstruction of a fixed historic diversion weir (known locally as *'Ichinoarate* weir') at the bifurcation point. Because the project was nearly completed in early 2018, Okayama city was spared damage during the 2018 flood. However, some fixed weirs, sandbars, and thick trees exist around the diversion weir in the lower reaches of the Asahi River, causing a complicated flow regime. Furthermore, the diversion discharge over the fixed weir might depend on the vegetation distribution and topographical changes that occur

around the river corridor. Therefore, study of how the riverbed deformation and vegetation changes during flooding affects actual diversion discharges in the river channel are necessary. In earlier works, flood flow conditions, including the water level and distributary discharge around the corridor were examined using a conventional unsteady two-dimensional (2-D) depth-averaged numerical approach, but their reproducibility has been confirmed only qualitatively (e.g., Yoshida et al., 2020a). However, when using the existing 2-D model, quantifying the flood flow across the diversion area, including its vertical flow distribution, is difficult. In addition, because of the densely vegetated floodplain near the diversion site, local scouring from turbulent flow at near-bed might occur, which is impossible to depict using 2-D modeling. Therefore, a new three-dimensional (3-D) flow model was constructed for the comprehensive study of both free surface and near-bed flow regimes, including the vertical flow field around the diversion weir, by estimating topography, land cover, and 3-D vegetation distribution within the study reach.

To date, hydraulic phenomena attributable to riparian vegetation have attracted a remarkable amount of attention from fluvial scientists for river management purposes (Corenblit et al., 2007; Gurnell, 2014; Nepf, 2012a). Furthermore, a considerable amount of research has already examined the modeling of open-channel flow and parameterization of hydraulic resistance attributable to vegetation distributed both on a laboratory scale and reach scale using various one-dimensional (1-D) (Fathi-Moghadam et al., 2011) and 2-D approaches (Yoshida et al., 2020a) to numerical simulations; however, many unclear aspects remain to be explored. Elucidating the complex flow environment around actual riparian vegetation is a challenging task using the yields of the 1-D and 2-D numerical approaches which have been developed

to date. Therefore, a detailed 3-D interpretation is necessary to enhance physical insights into flow phenomena, including aids to river engineering measures. However, although higher-dimensional approaches are appropriate for replicating laboratory experiment results, recalibration for each flow condition, considering vegetation effects, is an important impediment that hinders field applications. Some leading researchers have recently validated 3-D numerical approaches to simulate open-channel flow characteristics, considering vegetation attributes and distribution or arrangement, compared to physical models in laboratory studies where vegetation is idealised with a high degree of abstraction (Brito et al., 2016; Fischer-Antze et al., 2001; Li & Zeng, 2009). For instance, as described in an earlier report (Brito et al., 2016), researchers validated a 3-D turbulence model to simulate compound horizontal and rectangular open-channel flows in laboratory flume experiments, whereas submerged vegetation was arranged vertically (*i.e.,* column-based) with a given simple geometry and rigid conditions. Their findings related to flow field analysis might not meet practical demands at the river channel under such idealised conditions. By contrast, only minimal research has been conducted at a reach-scale (Stoesser et al., 2003; Wilson et al., 2006) to verify natural river flow attributes, considering the footprint of distributed riparian vegetation. However, related to the reach-scale vegetation turbulence modeling related to stream resistance (Nepf, 2012b), the marked shortcomings include reproduction of vegetation distribution over widely various rivers and difficulties in observing flood flow as verification data.

Related to the limitations described above, recent river survey technologies using ground-based or terrestrial laser scanning (TLS) (Manners et al., 2013; Straatsma et al., 2008), airborne laser scanning or airborne light detection and ranging (LiDAR)

method (Straatsma & Baptist, 2008), airborne LiDAR topo-bathymetry (ALB) (Yoshida et al., 2020a), unmanned aerial vehicle (UAV)-borne LiDAR (Islam et al., 2022), and others have been improved considerably for rapid reproduction of 3-D topographical information. Although these techniques are still under development, one can estimate the ground cover and vegetation species at an approximate order of several meters. For instance, Manners et al. (2013) used LiDAR-based TLS data to parameterise riparian vegetation patch-scale-based (submeter) hydraulic roughness patterns for 2-D flow field simulations. Also, Yoshida et al. (2020a) estimated flow resistance parameters in vegetated rivers using ALB data with extracting spatially explicit vegetation conditions, including 2-D land cover classification (LCC) data, vegetation vertical structures, and heights. Therefore, the application of LiDAR-based approaches is not limited to improving the accuracy of river flow analysis when considering distributed vegetation conditions.

Despite the advancement in remote sensing techniques for extracting distributed hydrodynamic parameters, the uncertainty of parameter estimation in flood flow simulation has been highlighted in earlier reports (e.g., Yoshida et al., 2020a) due to the long time lag between the acquisition of measurement data and flood occurrence, as well as a lack of observation data for model verification. Based on such a context, the current study applied the ALB approach (Yoshida et al., 2020a) to field-scale investigations before and after targeted flooding occurred in the vegetated lower Asahi River of Okayama Prefecture in Japan. Furthermore, no report of the relevant literature describes comprehensive research that numerically simulates flood flows in a vegetated river channel/floodplain using standard turbulence modeling, with specific examination of the reach-scale-based 3-D distribution of vegetation elements.

Given that background, this research is the first of a study that constructed and evaluated a fully 3-D flood simulation model with k–ε parameterization of turbulence by obtaining information related to topography, ground cover, and vegetation distribution from seamless ALB data. Subsequently, flood flow conditions, including longitudinal profile of water levels, depth-averaged flow velocity distribution, and vertical and horizontal flow fields around the targeted river's diversion weir were quantitatively confirmed. It is noteworthy that this study includes examination of the recent 2020 (low discharge) and 2018 (high discharge) floods in the river under study. Furthermore, accuracy of the 3-D simulation was evaluated in comparison to 2-D hydrodynamic-numerical model reported earlier (Yoshida et al., 2020a), in addition to space-time image velocimetry (STIV)-derived (Fujita et al., 2007; Yoshida et al., 2020b) flood flow data, and field observations. Specifically, the overarching goal of the current study was to ascertain the flood flow response to the distributed vegetation conditions around the diversion area. Findings of this study are expected to provide useful information related to management tasks for such hydraulic structures, which are designed to drain heavy rains or flood waters in vegetated rivers safely. Results of the current study can help policymakers develop a balanced and rational scenario for flood control measures that incorporates consideration of best vegetation management practices around river corridors.

3.3 Numerical Methodology

3.3.1 Governing equations

The proposed 3-D flood flow model used the concept of a porous model described by the volumetric-average of 3-D Reynolds-averaged Navier–Stokes (RANS) equations with the Cartesian coordinate system (Brito et al., 2016). Herein, the fractional area and volume obstacle representation (FAVOR) approach (Hirt & Sicilian,

1985) was incorporated into governing equations such that the model can be applied to flow fields with complex topography to estimate the fractional area ratios used for this study (Figure 3.1).

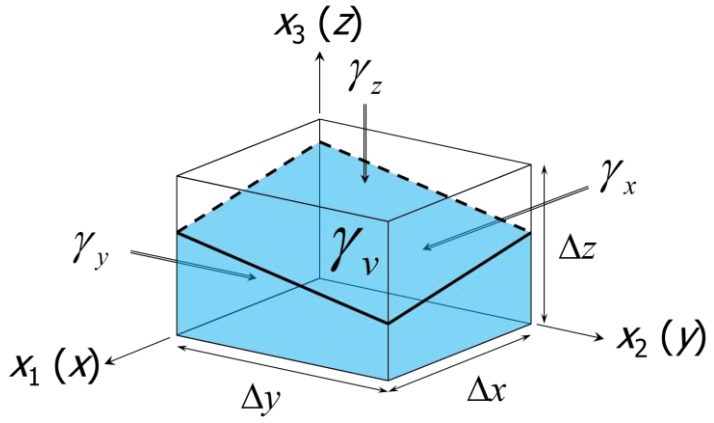

Figure 3.1 Specified directions for each fractional area ratio (γ_x, γ_y, γ_z) of 3-D flow. Δx, Δy, and Δz respectively denote the grid sizes in the x, y, and z directions.

The following basic governing equations introduced by the FAVOR method explicitly were used in the currently proposed flow model.

[Continuity equation]

$$\frac{\partial}{\partial x_i}\left\{\gamma_{(i)} u_i\right\} = 0 \qquad (1)$$

[Momentum equation]

$$\frac{\partial u_i}{\partial t} + \frac{1}{\gamma_v}\left\{\frac{\partial \gamma_{(j)} u_j u_i}{\partial x_j}\right\} = -g\delta_{3i} - \frac{1}{\rho}\frac{\partial P}{\partial x_i} + \frac{1}{\gamma_v}\frac{\partial}{\partial x_j}\left\{\gamma_{(j)}(\nu + \nu_t)\left(\frac{\partial u_i}{\partial x_j} + \frac{\partial u_j}{\partial x_i}\right)\right\} - \frac{F_i}{\gamma_v} \qquad (2)$$

Therein, the following variables are used: t represents time; subscripts i = 1, 2, 3; dummy indices j = 1, 2, 3; (x_1, x_2, x_3) = (x, y, z) in Cartesian coordinates (x, y, and z respectively represent the longitudinal, cross-sectional, and vertical directions for a

main river flow); u_i stands for the flow velocity component in the x_i direction [(u_1, u_2, u_3) = (u, v, w)]; γ_V denotes the fractional volume ratio or the vegetation porosity in a calculation grid; $\gamma_{(i)}$ expresses the fractional area ratio in the x_i direction elucidated in Figure 3.1 [($\gamma_{(1)}$, $\gamma_{(2)}$, $\gamma_{(3)}$) = (γ_x, γ_y, γ_z)]; g signifies the acceleration of gravity; δ is Kronecker's delta; $P = p + 2/3\rho k$; p signifies the pressure; ρ stands for the fluid density; k denotes the turbulent kinetic energy; ν is the coefficient of kinematic viscosity; ν_t is the coefficient of eddy viscosity; and F_i expresses the component of vegetation resistance in the i direction.

3.3.2 Physical modeling and parameters

As earlier works have demonstrated, to clarify the vegetation's resistance behaviour, one must define its spatial distribution (e.g., Nepf, 2012b) considering different natural conditions of vegetation: flexural rigidity (e.g., Aberle & Järvelä, 2013), vegetation density (e.g., Stone & Shen, 2002), porosity (e.g., Brito et al., 2016), emergence and submergence (e.g., Wu et al., 1999), local turbulence (e.g., Stoesser et al., 2010), and so on. Accordingly, for this study, by employing the respective ALB data of distributed vegetation characteristics, the local drag force was incorporated into the proposed model for 3-D flow computations. The following equation was used to estimate vegetation resistance in this study.

$$F_i = \frac{1}{2} C_D \lambda u_i \sqrt{u_j u_j} \quad (3)$$

In which, C_D is the drag coefficient; λ denotes the vegetation density.

In addition to estimation of the eddy viscosity coefficient, the standard k–ε turbulence model proposed by the principle of renormalisation group theory (Yakhot et al., 1992) was used, with the effect of vegetation resistance also considered (López & García,

1998).

[k equation]

$$\frac{\partial k}{\partial t}+\frac{1}{\gamma_v}\left\{\frac{\partial \gamma_{(j)} u_j k}{\partial x_j}\right\}=\frac{1}{\gamma_v}\frac{\partial}{\partial x_j}\left\{\gamma_{(j)}\nu_k\frac{\partial k}{\partial x_j}\right\}+\nu_t\frac{\partial u_i}{\partial x_j}\left(\frac{\partial u_i}{\partial x_j}+\frac{\partial u_j}{\partial x_i}\right)+C_{fk}\frac{F_j}{\gamma_v}u_j-\varepsilon \quad (4)$$

[ε equation]

$$\frac{\partial \varepsilon}{\partial t}+\frac{1}{\gamma_v}\left\{\frac{\partial \gamma_{(j)} u_j \varepsilon}{\partial x_j}\right\}=\frac{1}{\gamma_v}\frac{\partial}{\partial x_j}\left\{\gamma_{(j)}\nu_k\frac{\partial \varepsilon}{\partial x_j}\right\}+\frac{\varepsilon}{k}\left[C_{\varepsilon 1}\left\{\nu_t\frac{\partial u_i}{\partial x_j}\left(\frac{\partial u_i}{\partial x_j}+\frac{\partial u_j}{\partial x_i}\right)+C_{f\varepsilon}\frac{F_j}{\gamma_v}u_j\right\}-C_{\varepsilon 2}\varepsilon\right] \quad (5)$$

$$\nu_t=C_\mu\left(k^2/\varepsilon\right)$$
$$\nu_k=\nu+\nu_t/\sigma_k;\quad \nu_\varepsilon=\nu+\nu_t/\sigma_\varepsilon \quad (6)$$

Therein, the following variables are used: ε signifies the turbulent energy dissipation rate; F_j denotes the component of vegetation resistance in the j direction; C_μ, σ_k, σ_ε, $C_{\varepsilon 1}$ and $C_{\varepsilon 2}$ stand for the turbulent constants; and C_{fk} and $C_{f\varepsilon}$ are coefficients related to the vegetation resistance.

Furthermore, in the k–ε model used herein, the following standard values were assigned to the respective constants: C_μ = 0.09, σ_k = 1.0, σ_ε = 1.3, $C_{\varepsilon 1}$ = 1.44, $C_{\varepsilon 2}$ = 1.92 (Yakhot et al., 1992). The following conditions were applied for coefficients related to vegetation resistance: C_{fk} = 1.0 and $C_{f\varepsilon}$ = $C_{fk}C_{\varepsilon 2}/C_{\varepsilon 1}$ (López & García, 1998).

3.3.3 Numerical scheme

The governing equations were discretised using finite-volume method on a collocated grid system. In this model, the highly simplified mark-and-cell (HSMAC) method in the collocated grid arrangement proposed by Ushijima and Nezu (2002) was adopted to satisfy the local continuity equation and to solve pressure. The definition of flow variables located on the x–z plane is presented in Figure 3.2.

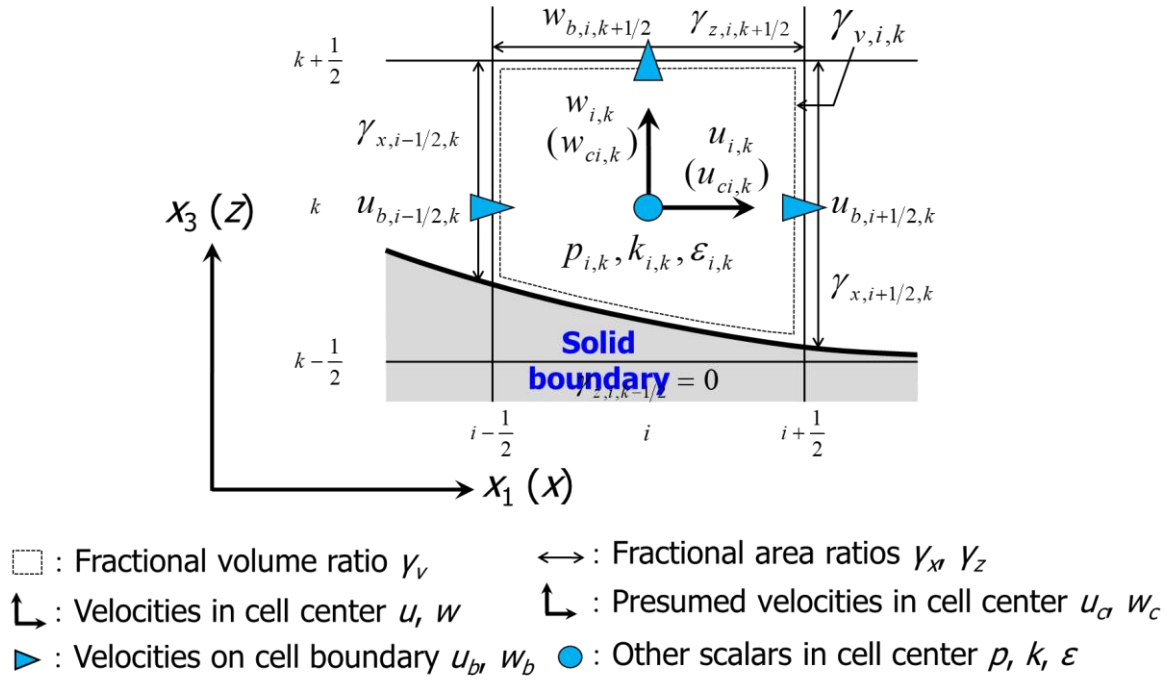

Figure 3.2 Definitions of computation points of flow variables on the *x*–*z* plane.

Furthermore, Figure 3.3 presents an outline of the main steps followed herein for 3-D flow calculation. In the numerical procedure, first, the known pressure p^n defined in the cell center was split into static pressure $p_0{}^n$ and anomaly pressure p^{hn}. The momentum equations used herein are regarded as an estimate of presumed velocities $u_c(w_c)$ in the cell center using the known velocities $u^n(w^n)$, which were exempted from the anomaly pressure expression; where n is the number of the time steps. To achieve high-order accuracy and to estimate discontinuous flows stably, the advection terms of the momentum equation were discretised using the fifth-order weighted non-oscillatory (WENO) scheme (Shu, 2003). Furthermore, time integration was performed using the second-order Adams–Bashforth approach. Second, by linear interpolation, the presumed velocity on the cell boundary $u_b(w_b)$ was calculated using the presumed velocity in the cell center $u_c(w_c)$, whereas the HSMAC technique solved both the new anomaly pressure p^{hn+1} and the new velocity on the cell boundary

$u_b^{n+1}(w_b^{n+1})$. Afterwards, using the central difference value of the new anomaly pressure p'^{n+1}, the new velocity in the cell center $u^{n+1}(w^{n+1})$ was ascertained from the presumed velocity in the cell center $u_c(w_c)$. Ultimately, the water surface position was updated using the new velocity on the cell boundary u_b^{n+1}, after integrating the continuity equation in the vertical direction. In addition, the advection terms of the k–ε model were discretised by application of the WENO scheme.

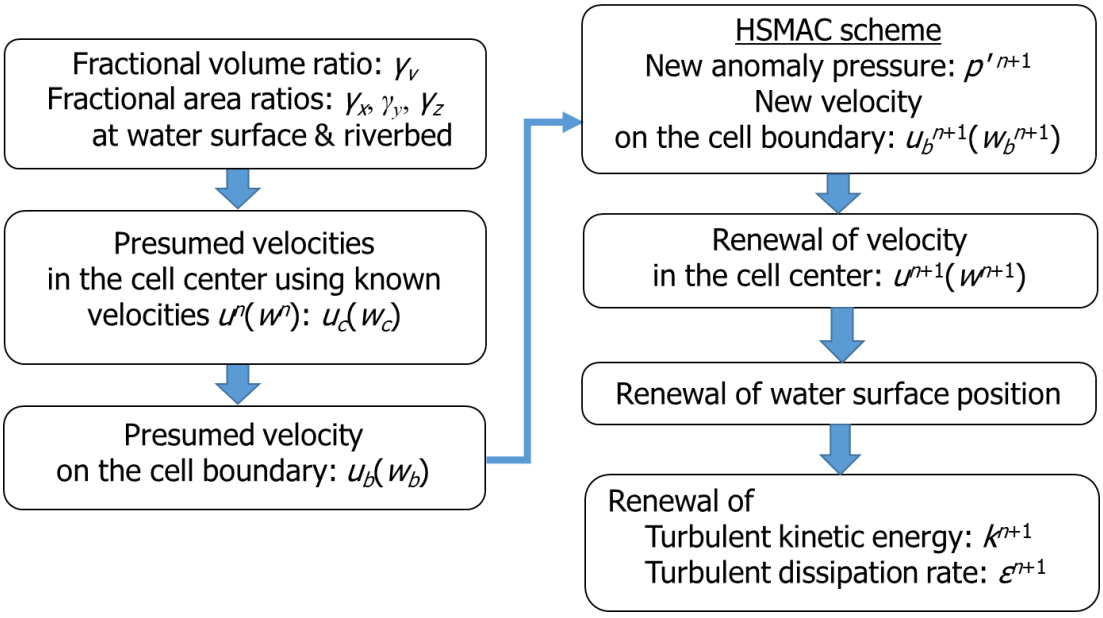

Figure 3.3 Schematic overview of the main steps in the 3-D flow calculation.

3.3.4 Boundary conditions

Based on flow records, the discharge and water level data obtained at the study reach ends were adopted as the numerical computation boundary conditions. As the upstream boundary conditions, the velocity distribution according to the log law in the vertical direction was used to achieve the prescribed flood flow discharge. The turbulent values were assigned using some equations proposed by Kuhnle et al. (2008).

$$k = 4.78u_*^2 \exp\left(-2\frac{z'}{h}\right) \qquad (7)$$

$$\varepsilon = k^2 C_\mu \Big/ \left\{ \kappa u_* z' \left(1 - z'/h\right) \right\} \qquad (8)$$

In those equations, the following are used: u_* denotes the shear velocity; z' represents the distance from the riverbed in the vertical upward direction; h stands for the flow depth; and κ is the von Karman constant (= 0.41).

The prescribed water level and the condition of zero gradient in the flow direction for the velocities and the turbulent values were given at the downstream boundary. Moreover, at the wall boundary, the shear resistance according to the log law was inferred for the flow velocities. Turbulent values were estimated using the following wall functions (Rodi, 2000).

$$k = \frac{u_*^2}{\sqrt{C_\mu}} \qquad (9)$$

$$\varepsilon = \frac{u_*^3}{\kappa \cdot \Delta} \qquad (10)$$

Therein, Δ represents the distance from the solid wall boundary to the nearest calculation point.

Furthermore, the free-slip condition was applied to the velocities and to water surface turbulence. For the numerical simulation, in addition to the free surface condition, a fixed riverbed was considered for simplicity. In the context of drying situation assessment, a water threshold depth of 0.1 m was considered, based on approximate numerical estimates, to prevent uncertainty that might arise from high velocities close to the wet–dry boundary. Furthermore, a velocity of zero was assumed for computation nodes in the dry bed state, whereas the slip-velocity was used near the water edge.

3.4 Study Site and Data Acquisition and Processing

3.4.1 Asahi River Basin

The Asahi River, a first-grade river in Japan due to its economic or other significance,

flows down through the Okayama prefecture into the Seto Inland Sea (Figure 3.4a).

(a)

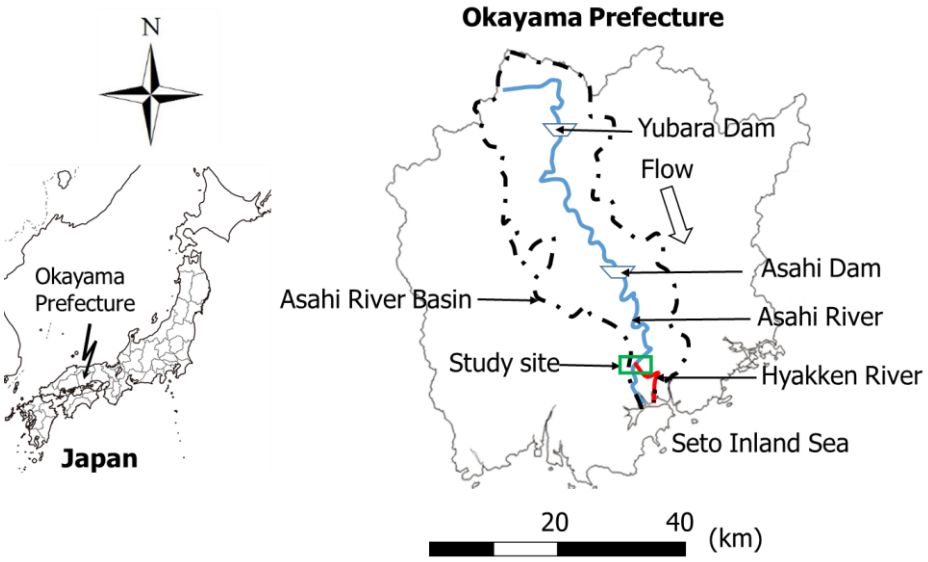

(b)

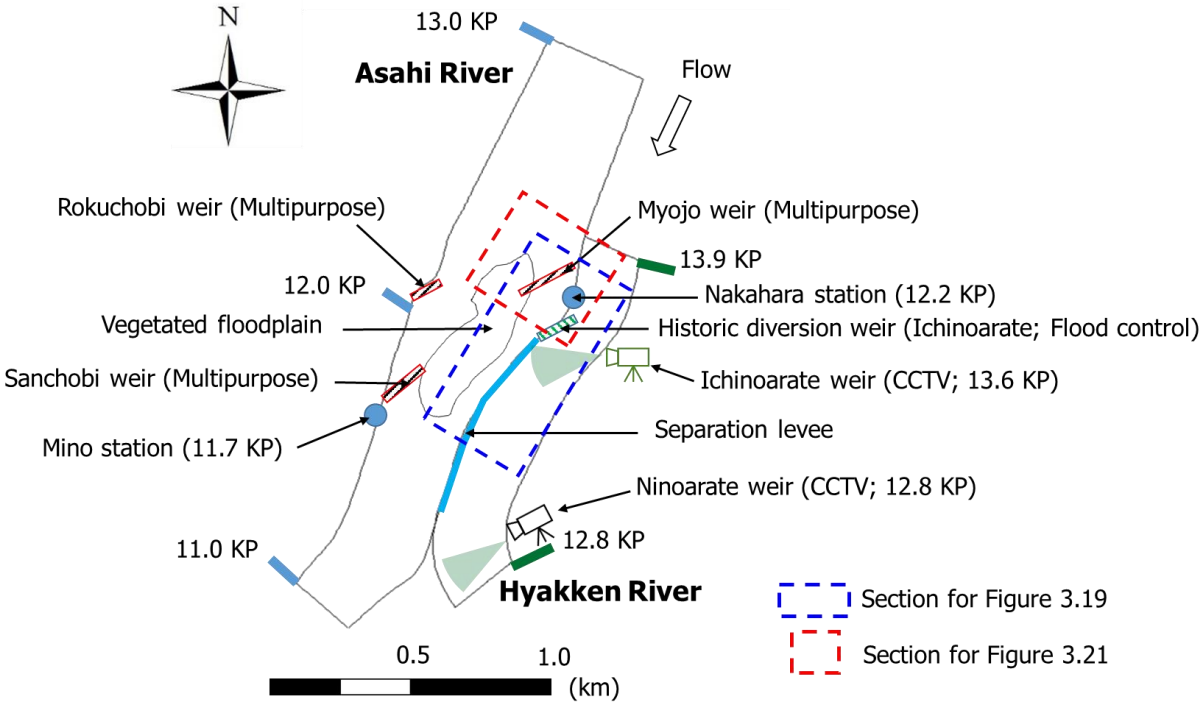

Figure 3.4 (a) Asahi River Basin in Okayama, Japan and (b) location of various hydraulic structures and stations around the targeted bifurcation point in the studied domain, with kilo post (KP) values signifying the longitudinal distance (km) from the river mouth.

Figure 3.4b depicts the study reach, including various hydraulic structures and stations around the fixed diversion weir, specifically examined for this study. The study reach comprises two channels; herein, the main channel is a 2.0 km long, approximately 300 m wide compound open channel (lower Asahi River, 11.0 KP to 13.0 KP) with a mean bed slope of 1:670. The other distributary channel is 1.1 km long, with an average width of approximately 200 m (Hyakken River, 12.8 KP to 13.9 KP) and a bed slope of about 1:1000. Hereinafter, the kilo post (KP) signifies the longitudinal distance from the respective river mouth in kilometers (km). However, within the investigated main channel, the annual mean maximum flow rate is around 1400 m^3/s; the representative grain diameter of the bed is 40–70 mm (Maeno & Watanabe, 2008). The river channels originally had numerous gravel bars. Watanabe et al. (2006) reported that establishment of multipurpose dams in upstream areas led to river forestation, with limited gravel bars. Because the river forestation might create several difficulties, the distributed vegetation in the targeted reach has recently drawn significant concern for flooding risks and ecosystem management tasks.

3.4.2 ALB data

3.4.2.1 Data acquisition and processing

In the targeted river reaches, both river topo-bathymetry and vegetation attribute measurements were conducted in November 2017 (before the 2018 flood) and February 2019 (after the 2018 flood), with a normal water level using an ALB device (Leica Chiroptera II; Leica Corp.) with near-infrared and green lasers, mounted on the aircraft. A typical view of ALB measurement is portrayed in Figure 3.5.

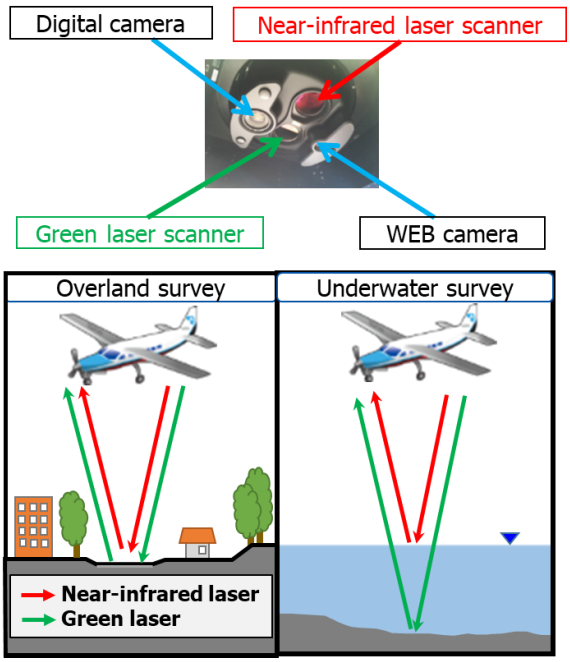

Figure 3.5 Typical view of airborne LiDAR topo-bathymetry (ALB) measurement for overland and underwater surveys.

Such measures are usually conducted under no-leaf vegetation and under low-turbidity water conditions, providing good penetration through deciduous woody vegetation (*e.g.*, willows) and underwater areas. To collect data with the desired properties (*i.e.*, data density, uniform distribution, spacing, and accuracy), overlapping coverage was achieved through several flight operations during each LiDAR measurement. Table 3.1 presents the main specifications of the airborne LiDAR device with the measurement conditions used for this study. ALB point clouds were analyzed using a full-waveform approach (Zhu et al., 2015), enabling us to distinguish bare earth from objects (*e.g.,* vegetation) on the ground.

For initial data processing, first, a Cartesian grid consisting of 3-D voxels, each with 0.5 m side length, was established within the targeted region to filter out noise from

the laser point clouds. Then, because of inhomogeneous laser point density caused by overlapping flight operations, only the highest point data from the ALB measurement were kept rather than all points in each voxel (Yoshida et al., 2017). Second, a horizontal 2-D cell with 2 m width, comprising 3-D point clouds, was developed.

Table 3.1 Specifications of the current ALB device with measurement conditions used in this study

Measurement time (yyyy.mm)			**2017.11**	**2019.02**
Equipment Specifications	Laser wavelength (nm)	near-infrared	1,064	
		green	515	
Measurement Specifications	Number of laser pulses per second	near-infrared	200,000	148,000
		green	35,000	
	Flight altitude (m)		500	
	Flight speed (km/h)		220	110
	Density of laser points ($1/m^2$)	near-infrared	8.0	64.0
		green	2.0	4.5
Water Quality	Turbidity*		3.2	1.7

* Kaolin suspension, Hydrological Water Quality Database (Asahi River, Otoizezeki Water Quality Observatory)

Subsequently the ground level was found by filtering the laser points near the lower portion of the 2-D cell (*i.e.,* digital terrain model, DTM). The vegetation height was assessed further by considering the highest data point in each 2-D cell (*i.e.,* digital surface model, DSM). Voxel-based initial data processing for the 3-D laser point clouds is depicted schematically in Figure 3.6.

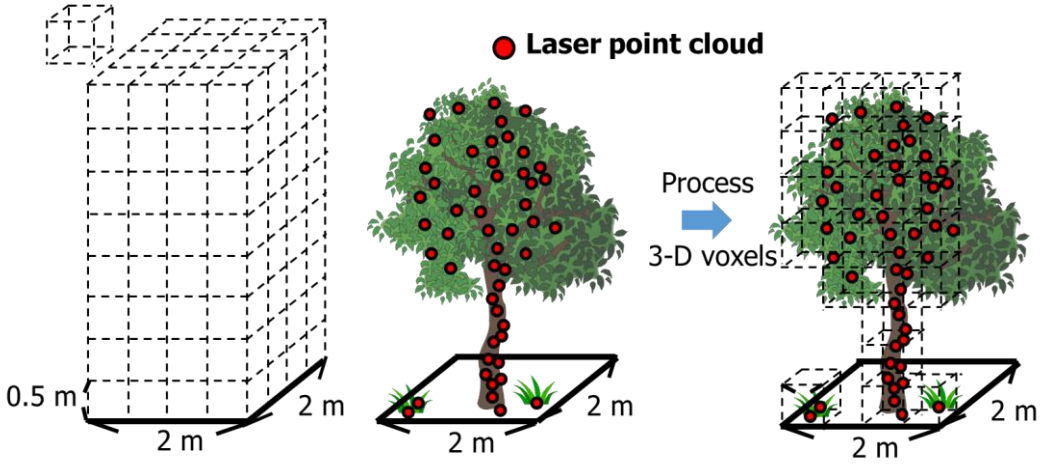

Figure 3.6 Initial data processing for 3-D laser point cloud using voxels.

3.4.2.2 Topo-bathymetric data

The present study extracted river terrain data, particularly addressing both overland and underwater areas before and after the targeted floods, particularly for the event in 2018. No recent ALB measurement was taken following the small flooding event of July 2020. It was reported from a past overview that ALB measurements are typically conducted after larger-scale flooding events. Furthermore, after minor floods such as the one in 2020, riverbed deformation might not be so great compared to the more destructive event. However, a more recent report by Yoshida et al. (2020a) described comparisons of ALB with ground-truth observations in the river studied herein, revealing that the LiDAR-derived DTM values were almost identical to the field-observed bed elevations with accuracy of about 10 cm. In addition, the root-mean-square-error values of the LiDAR measurements (i.e., vertical errors) compared with findings of field surveys were approximately 0.08, 0.10, and 0.2 m, respectively, for the gravel riverbed, the vegetated bed, and the underwater bed. Therefore, based on earlier findings, the ALB datasets used in this study can be expected to be valid for the 2020 and 2018 flood simulations.

3.4.2.3 Vegetation attributes

A remarkable variety of vegetation species has been recorded at the targeted site. That reality notwithstanding, the riparian vegetation comprises three groups based on stream resistance: herbaceous species, arborous or woody species, and bamboo grove. An earlier report by Yoshida et al. (2020a) evaluated ALB data for comparison with the woody vegetation (*i.e.*, willow) heights observed around the historic diversion site examined in this study, demonstrating that estimates made using ALB data were almost consistent with the results obtained from ground surveys, although the LiDAR-based measurements were around 60 cm smaller, on average, than the field observations. Such a trend was also reported by Straatsma & Baptist (2008), who attributed it to the fact that willow branch ends are so thin that the laser cannot identify the trees' top edge precisely. Therefore, the ALB datasets can reasonably, but not precisely, show the vegetation attributes to estimate the flow resistance for flood simulations.

Figure 3.7a depicts the concept of a horizontal 2-D vegetation distribution model using pre-processed data of voxel-based laser points and vegetation height, where the model can only consider one plant height at a single point on the horizontal plane. In the area surrounded by the red-dotted frame in the figure, the laser hits the branches and leaves to provide data for determination of whether the vegetation is herbaceous or woody based on the criteria presented in Table 3.2.

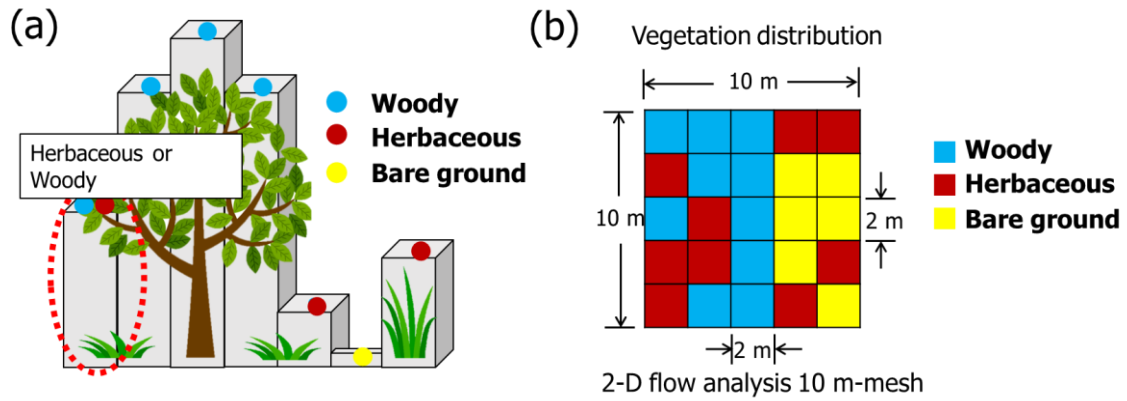

Figure 3.7 (a) Concept of vegetation distribution focused on a 2-D model and (b) example of vegetation distribution in the 10 m mesh of 2-D flood flow analysis.

Table 3.2 Criteria developed for 2-D land cover classification (LCC) using ALB data

LCC	**Number of laser points within 2-D cell of 10 m × 10 m area n_l**	**Vegetation height l (cm)**
Bare ground and Underwater areas	0–4	$l \leq 30$
Herbaceous plants	5–12	$l > 30$
Woody vegetation or Bamboo grove*	13–	$l > 30$

* Bamboo is not distinguished from woody vegetation using the n_l and l parameters of ALB data. In this case, vertical structure of ALB point clouds and high spatial resolution aerial images were considered to differentiate between those species (Figure 3.8).

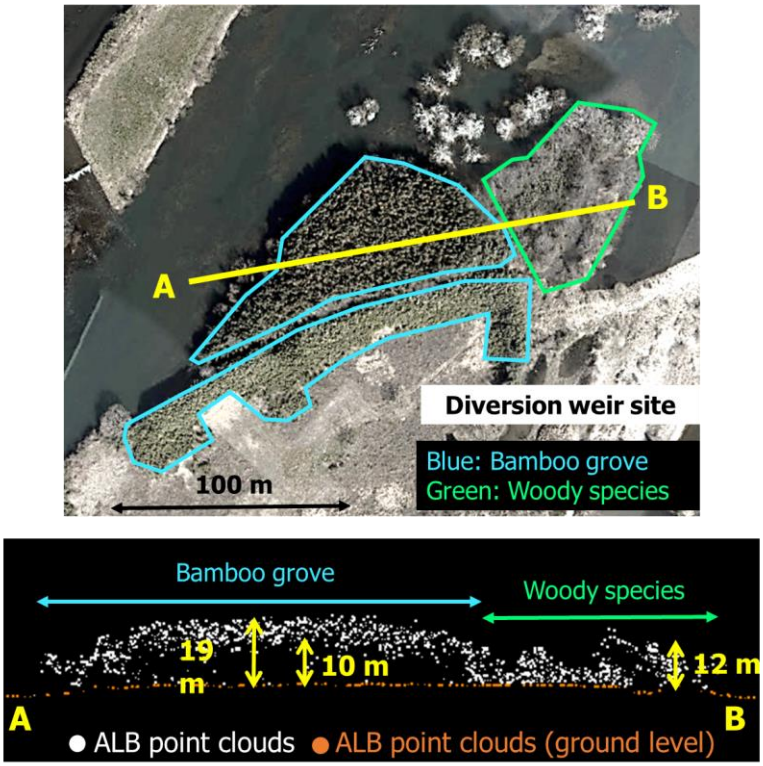

Figure 3.8 Vertical structure of ALB point clouds extracted around the diversion weir to distinguish between woody and bamboo species. Top, aerial image; bottom, point clouds along A–B line.

Consequently, using this model might reduce the reproducibility of vegetation data. The vegetation distribution was produced herein using initially processed voxel-based ALB data with a square grid of 2 m mesh (Figure 3.6). The calculation grid width used in the 2-D flood flow analysis of this study is about 10 m for practical use. Therefore, vegetation information (vegetation height, vegetation species, etc.) from the nearest ALB-based 2 m mesh was inserted into each of the 25 grid cells of the mesh used for the flow analysis (Figure 3.7b). In this case, the vegetation resistance was calculated by considering the ratio of the number of grid cells occupied by each type of vegetation to the total number of cells in the mesh (25). Some examples are

the ratio of herbaceous vegetation to the mesh = 9/25 (Figure 3.7b). The model used to calculate flow resistance assumes all vegetation as cylindrical. Furthermore, the vegetation height of each vegetation species in the 10 m mesh was calculated by taking the average value of each vegetation species in the divided mesh. In contrast, the 3-D vegetation distribution scheme (Figure 3.9a) includes not only multiple vegetation information in the vertical direction but also its spatial distribution.

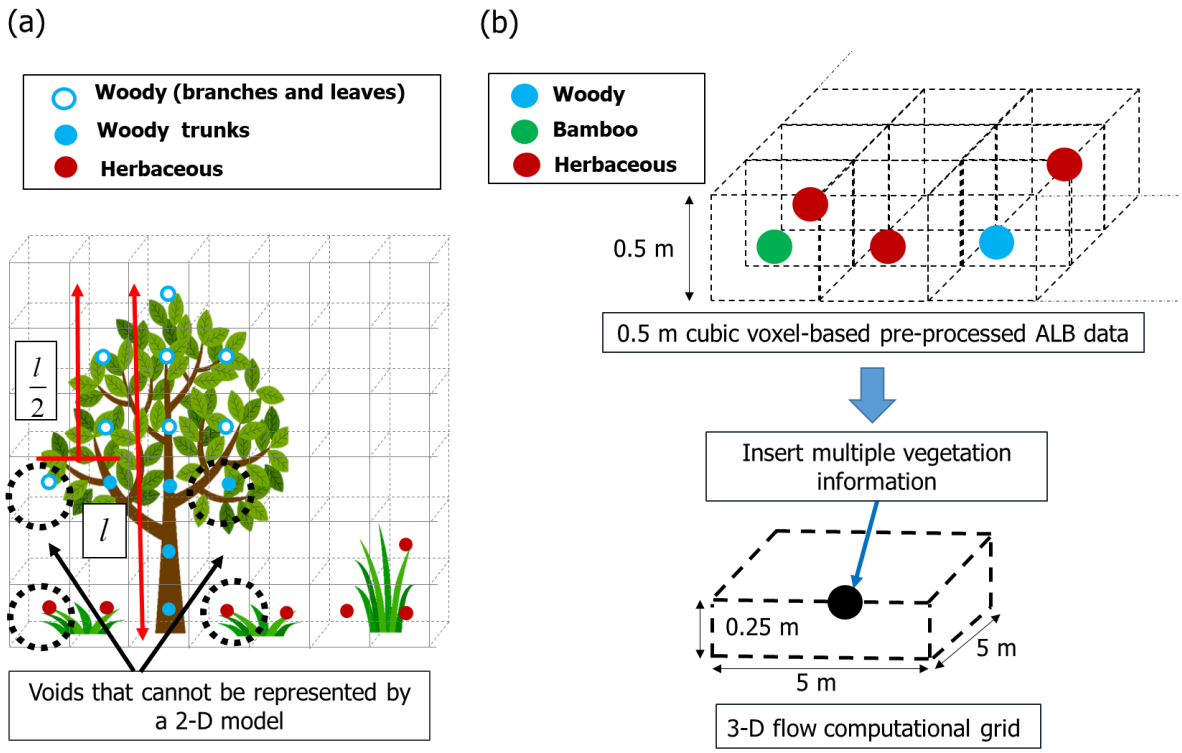

Figure 3.9 (a) Concept of vegetation distribution emphasizing a 3-D model and (b) vegetation distribution centered on a 3-D flow computational grid.

Fundamentally, the present study used 2-D LCC data, which are presented later in Figure 3.13a. The pre-processed ALB data with a single vegetation point on a 0.5 m cube were used to generate vegetation distribution data by dropping them onto a 3-D flow computational grid (5 m × 5 m × 0.25 m) applied for the current study, as

shown in Figure 3.9b. The main difference between this model and the 2-D model is that the trunks and branches of trees were newly classified and then their resistance were considered. In this case, the vertical mesh of 3-D analysis was used to reproduce the vegetation distribution more closely. Finally, the vertical resistance changes at the same horizontal x and y points were produced (black-dotted circle; Figure 3.9a) and the void between the canopy and the grass on the ground surface were identified (Figure 3.9a). Using void data, it was possible to identify the existence of herbaceous plants under the branches of woody species.

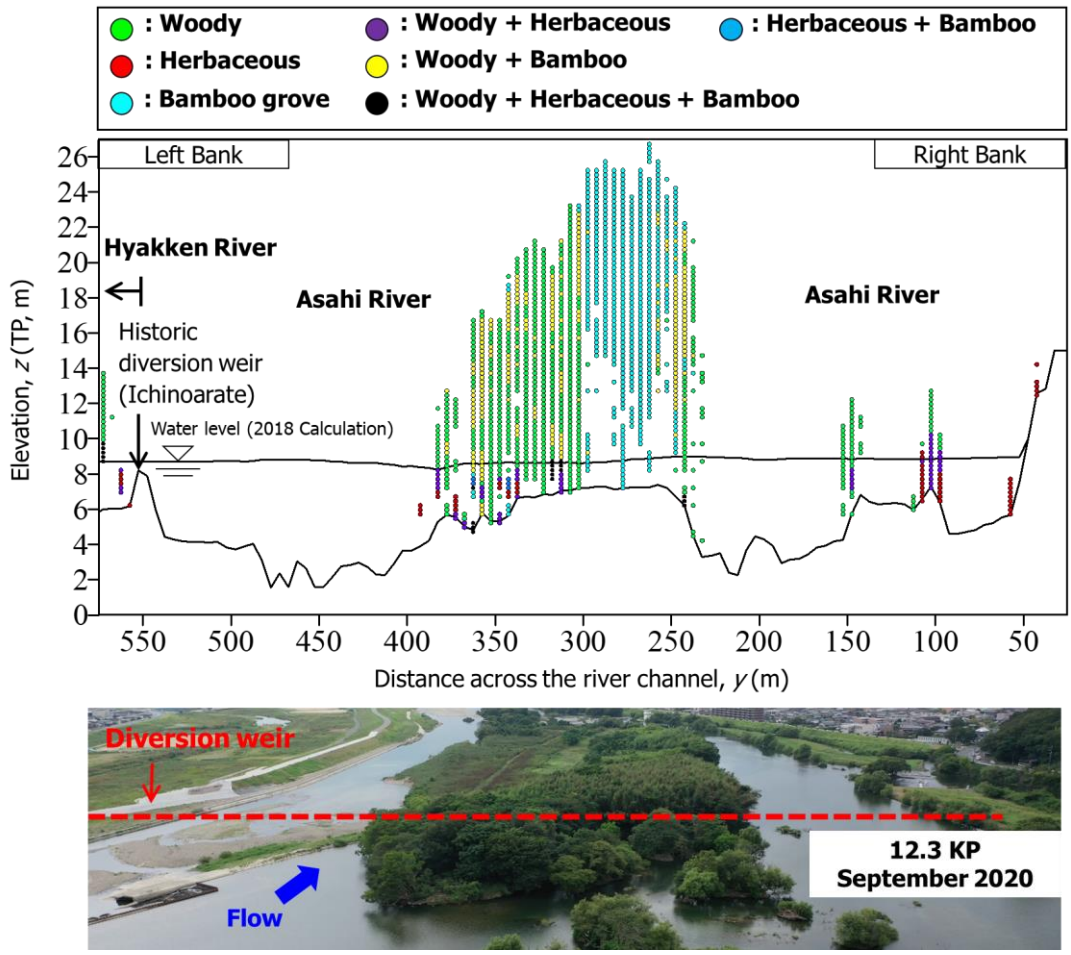

Figure 3.10 3-D distribution of vegetation data (2017 ALB) along the Asahi River around 12.3 KP section.

Figure 3.10 portrays the 3-D distribution of vegetation data established for the Asahi River cross-section around the diversion weir side. Herein, Tokyo Peil (TP) is the datum used throughout this study, signifying the average sea level of Tokyo Bay in Japan. It was observed that the ground cover attributes differ vertically. It was also observed that the void between the branches and leaves, as well as the herbaceous vegetation on the ground surface, can be reproduced. For this study, vegetation elements at more than 3 m above the ground surface were treated as woody plants because the ALB data sometimes identified woody plants' leaves such as herbaceous plants. The vegetation resistance was modeled in proportion to the flow velocity square using the drag coefficient to differentiate woody vegetation (trunk region), herbaceous plants, and bamboo forests. The drag forces representing flow resistance due to the distributed vegetation in the targeted area have already been detailed in equation (3), as shown in section 3.3.2. Furthermore, the flow resistance to the tree's leafy branches was modeled as a porous body with enormous voids. Under these conditions, the coefficient of inertial force in this analysis was set to 0 for simplicity (Li et al., 2006). However, determining the leafy parts of individual trees from ALB data is difficult. Consequently, the study assumed that the leafy parts to be at least half the trees' height ($h/2$; Figure 3.9a). In this case, the study did not define one vegetation height (h) for each tree, although the height was estimated considering the DSM minus DTM data at each horizontal x and y point. Furthermore, for flow resistance parameterization, this study included consideration of density for the targeted vegetation species, as described later in section 3.4.4.

3.4.3 Flooding in 2020 and 2018

3.4.3.1 Flood hydrograph

Two hydraulic stations operate in the targeted domain for the water levels observation: Mino station (11.7 KP) at the main Asahi River and Nakahara station (12.2 KP) near the distributary Hyakken River (Figure 3.4b). During the lower Asahi River flood in mid-July 2020, the river's discharge at Shimomaki Station (19 KP), which is upstream beyond the current target domain, was calculated using the *H–Q* relation. In contrast, for the July 2018 event, the study used discharge values estimated from flow simulation results at the upstream site rather than the empirical relation. It is noteworthy that no confluence of large tributaries exists from 19 KP to 13 KP (upper end of the computational domain). Figure 3.11 shows the observed water levels and estimated discharges for both events.

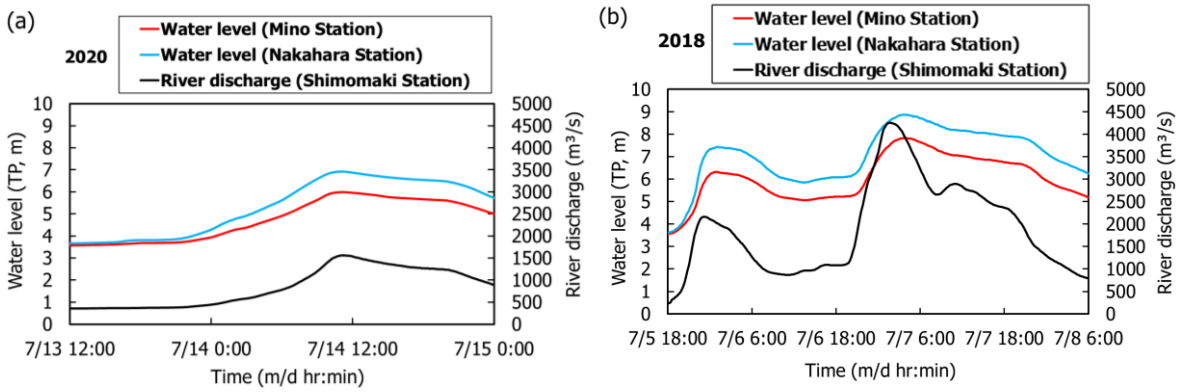

Figure 3.11 Observed water level and estimated discharge during Asahi River flooding in (a) 2020 and (b) 2018.

The recorded data were treated as the boundary conditions for the numerical simulations conducted in this study. For the 2020 flood in the Asahi River, a maximum discharge of about 1,561 m^3/s was recorded at 11:20 on 14 July, with only one peak

(Figure 3.11a). By contrast, in the 2018 flood, a peak discharge of approximately 4,251 m^3/s was reported at 1:40 on 7 July, with the two peaks highlighted in the hydrograph (Figure 3.11b). The 2018 event produced record stages and had a 40-year return interval based on the hydrologic record. Despite that historical context, such intense flooding might be occurring because of severe climate changes in recent years.

3.4.3.2 Flooding effects on vegetation and riverbed changes

Figure 3.12 depicts the states of the fixed historic diversion weir at the Asahi River's bifurcation point during the targeted floods, as photographed by drone and closed-circuit television (CCTV) cameras.

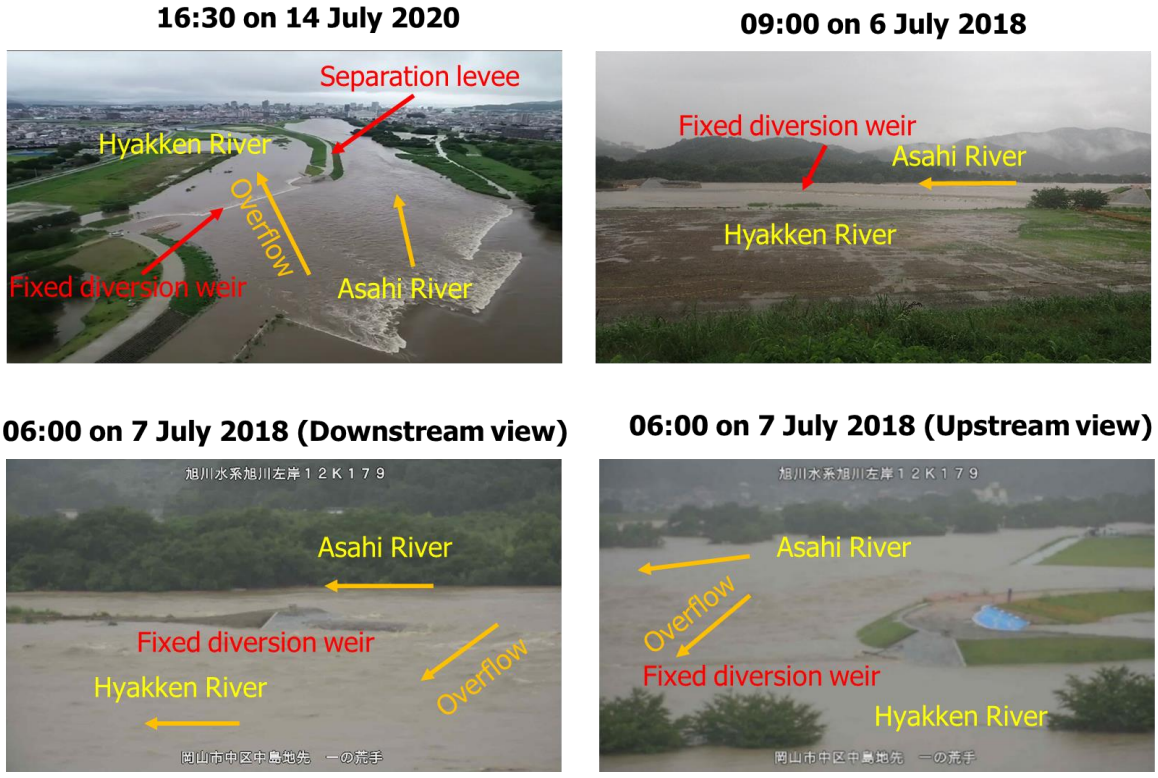

Figure 3.12 States of the diversion area during the 2020 and 2018 floods on the left bank of the Asahi River at about 12.2 KP.

Figure 3.13a portrays the 2-D LCC obtained according to the methodology already presented in Table 3.2, using the processed 2017 ALB dataset extracted for the study region.

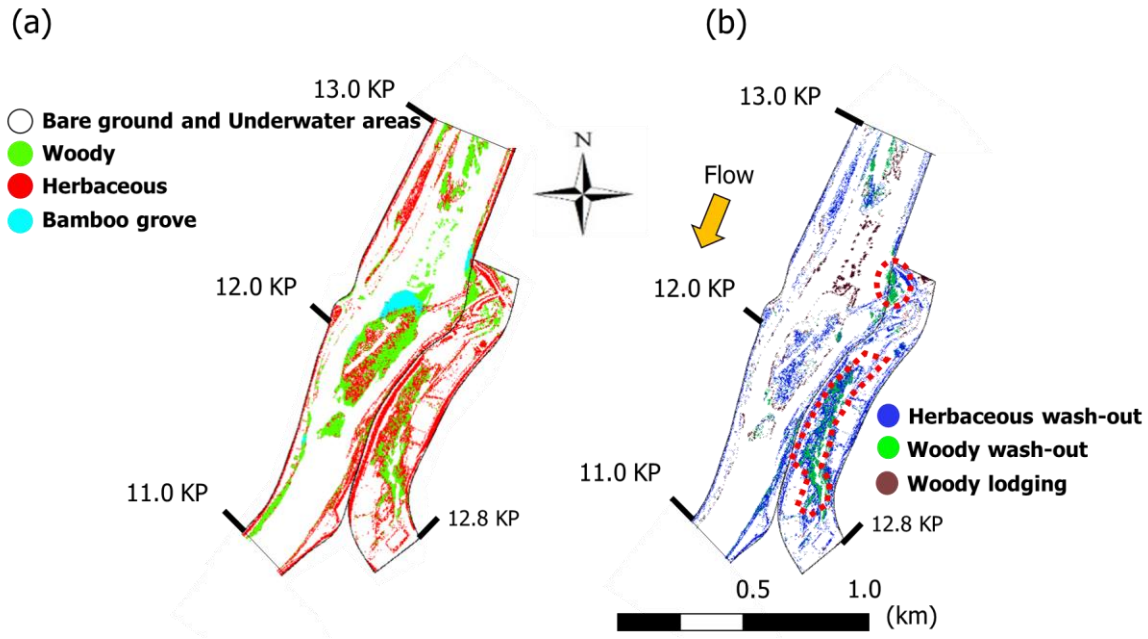

Figure 3.13 (a) Land cover classification before 2018 flooding and (b) changes in vegetation conditions because of 2018 flooding.

Using ALB-derived attributes (i.e., number of laser points within 2-D cell and vegetation heights; Figure 3.6), it was evident that bamboo is not distinguished from woody vegetation (Yoshida et al., 2020a). In this case, vertical structure of ALB point clouds and high spatial resolution aerial images were considered to differentiate between those species (Figure 3.8). However, this classification depicts vegetation species on gravel bars and floodplains before the 2018 event, demonstrating that the mapping was reasonably identical to the corresponding high-resolution aerial image (Figure 3.14a). Furthermore, Figure 3.13b presents changes in vegetation conditions as a result of flooding in 2018, as estimated based on vegetation heights derived from two ALB datasets before and after the flooding event. The mapping of

vegetation changes revealed that the targeted 2018 flood washed out and lodged some of the woody vegetation, but the bamboo grove remained unchanged. A detailed examination of aerial images obtained before and after the flood revealed that the changes visible in the red-dotted area in Figure 3.13b were not caused by the recent flood, because the wash-out of the trees in that region was attributable to artificial construction work conducted immediately before the 2018 flooding as part of the river improvement project (Fujikane et al., 2016).

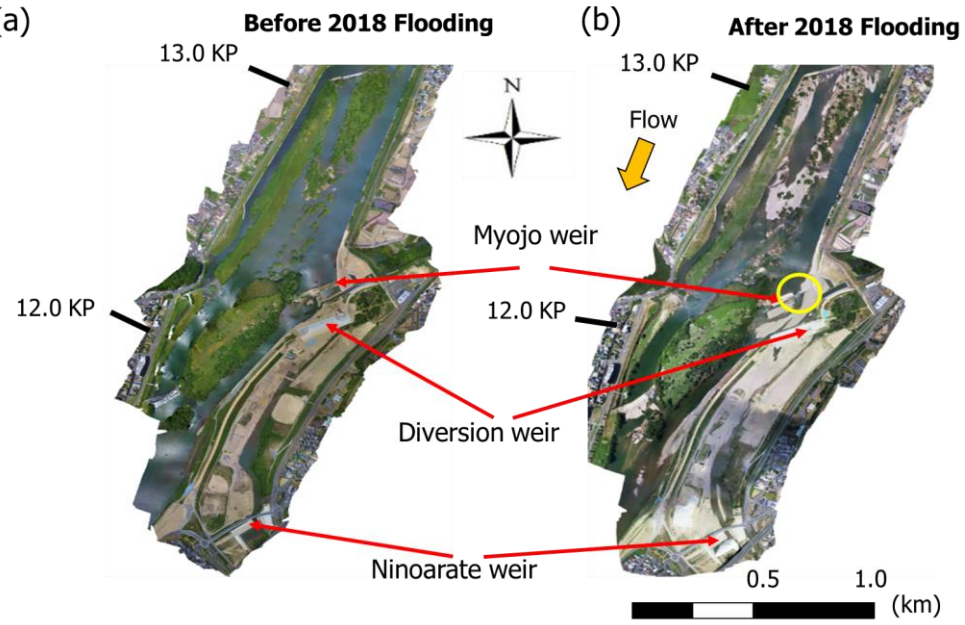

Figure 3.14 Drone-captured aerial images of the targeted region: (a) before 2018 flooding (May 22, 2018) and (b) after 2018 flooding (July 20, 2018)).

Figure 3.15(a) depicts a 3-D view of the riverbed elevation mapping using the existing ALB dataset extracted before the 2018 flood. Furthermore, Figure 3.15(b) demonstrates the bed deformation retrieved using the difference in the LiDAR survey results. Records of peak water levels observed by the Asahi River office and river

improvement project planning (Fujikane et al., 2016) confirmed that the elevation of the riverbed, particularly in areas encircled by the black-dotted line in this figure, was altered by human-induced construction work, irrespective of the flood. Results showed that the bed deposition of approximately 1 m was noticeable around the downstream of the multipurpose fixed weirs, locally designated as *'Myojo weir'* and '*Sanchobi weir*' (Figure 3.15b).

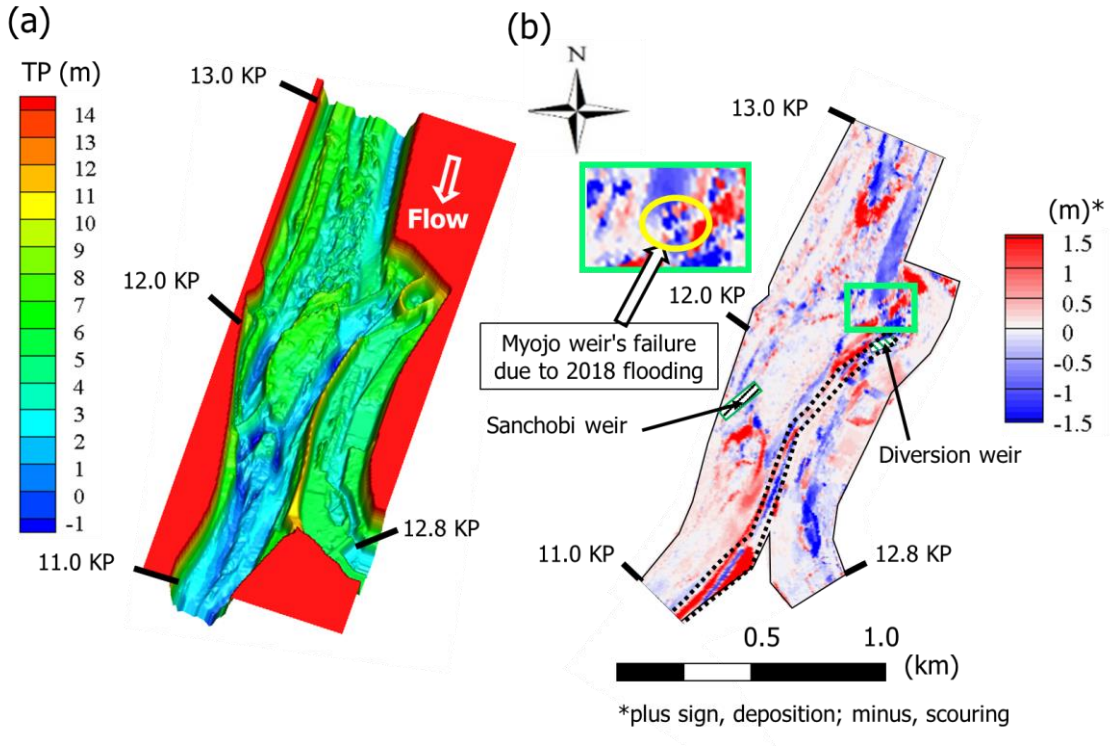

Figure 3.15 (a) 3-D bathymetric contour maps using ALB data extracted before 2018 flooding and (b) riverbed deformation because of 2018 flooding.

The yellow-circle eroded area inside the green-marked region (Figure 3.15b) shows parts of the *'Myojo weir'* that were damaged because of the 2018 flood. The eroded part was also visible in drone-captured aerial photographs after the flooding (Figure 3.14b). Furthermore, marked riverbed changes were evident at the upstream reach of the main Asahi River at around 13.0 KP (Figure 3.15b). The riverbed's deformation

around the targeted bifurcation point was caused partly by sand accumulation in front of the diversion area during the flood. Moreover, because no ALB measurement was taken after the small flood in 2020, this study did not demonstrate any change in vegetation or river bed conditions for the particular flooding. However, during such minor flooding, the riverbed elevation and vegetation conditions that cause flow resistance remain nearly unchanged (Islam et al., 2022).

3.4.3.3 Image-based data acquisition and STIV analysis

For both river monitoring and facility regulation during a normal water level, multiple CCTV cameras have been placed in the Asahi River. Some CCTV cameras were operated effectively at the lower Asahi River during the 2018 flooding. However, primarily in the targeted reach of this study, one CCTV camera was frequently operated at 12.8 KP (locally known as the '*Ninoarate*' area) to track flood flows and rising water levels. During the smaller 2020 flood, the river flow was monitored using another CCTV camera around the diversion section at about 12.2 KP.

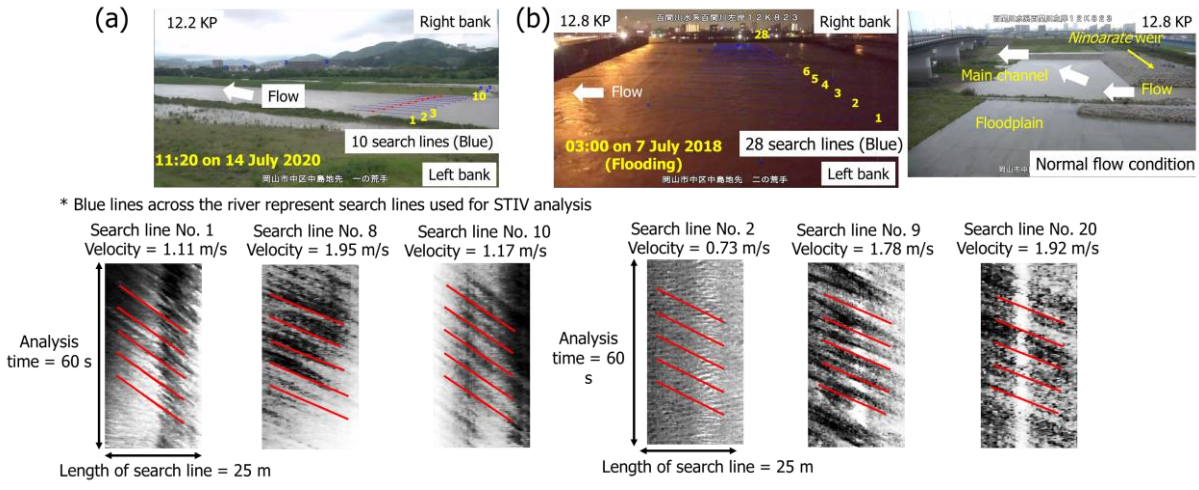

Figure 3.16 Sampled images for STIV analysis and their corresponding space-time images (STIs) at different cross-sectional locations: (a) around the diversion weir's downstream side (12.2 KP) in Hyakken River during 2020 flood, and (b) *Ninoarate*

area (12.8 KP) in Hyakken River during 2018 flood. * Blue lines across the river represent search lines used for STIV analysis.

Figure 3.16 portrays sample CCTV images captured during the 2020 and 2018 floods. Herein, to perform STIV analysis, the recorded sample images were superimposed with blue search lines across the river. Table 3.3 reports the main specifications of the CCTV camera and the STIV analysis conducted for the current study. By employing deep-learning-based commercial software (Hydro-STIV; Hydro Technology Institute Co., Ltd., Japan), the longitudinal surface flow velocities on specified search lines were computed automatically for the sampled images during the overall analysis period of 60 s.

Table 3.3 Specifications of CCTV camera and STIV analysis used in this study

CCTV camera	**Spatial resolution of the camera image (pixels)**	**1920 × 1080**
	Time interval for each image (Hz)	30 (normal mode) 3 (night mode)
STIV analysis	Software for STIV	Hydro-STIV
	Searching line length (m)	25
	Analysis period (s)	60

Figure 3.16 elucidates the space-time images (STIs) at different cross-sectional locations for the respective sampled photographs captured during flooding events. Each STI had such a line pattern that was angled towards the lower right corner. The average slope of the line patterns is shown by the red line, which was drawn automatically by the STIV software. The STIs for the 2020 flooding (Figure 3.16a) revealed that their gradient and sharpness were smooth when compared to results for the 2018 flooding (Figure 3.16b). Consequently, estimation of surface flow velocities in 2018 might be affected by noise, caused by low-quality sampled images

because of a lack of night lighting and raindrops on the camera lens.

3.4.4 Numerical conditions for flood flow simulations

The present study used the 3-D and 2-D (Yoshida et al., 2020a) numerical models described above for flood flow simulations. The 2-D flow modeling approach is based on a conservative boundary-fitted coordinate system. The governing equations were discretised in a staggered mesh using the finite volume method. To compute the time development of the flow variables explicitly, the second-order Adams–Bashforth scheme was used. In contrast, the second-order central scheme was used to discretise spatial derivatives, except for advection terms, which were computed using the first-order upwind scheme. In addition, for the 2-D modeling, the eddy viscosity coefficient was estimated by depth-averaging a simple empirical parabolic distribution. Table 3.4 presents the numerical conditions applied for the 3-D computation of the targeted 2018 and 2020 flood flows over the domain examined for this study. For flood flow analyses, the targeted period was 36 hours, from 12:00 on 13 July to 0:00 on 15 July in 2020, and from 18:00 on 6 July to 6:00 on 8 July in 2018. Numerical computations were performed for both fixed-bed and current vegetation distribution using the existing ALB datasets acquired in 2017 and 2019. Although large bed deformation was observed in the targeted domain after the 2018 flooding (Figure 3.15b), for simplicity, the model did not consider transient changes in bed elevation. Additionally, the washed-out vegetation condition was not included in the numerical calculations because mainly herbaceous species were washed out by the flood waters (Figure 3.13b), which presumably did not affect the flow simulation to any marked degree.

Table 3.4 Analytical conditions for flood flow simulations

Discrete interval	2-D	Time step	Δt = 0.02 s
		Grid size	$\Delta x = \Delta y$ = 10.0 m (Typical)
	3-D	Time step	Δt = 0.05 s
		Grid size	$\Delta x = \Delta y$ = 5.0m, Δz = 0.25 m
Vegetation	Woody (branch and leaf) void ratio, γ_v		0.7 (Constant value)
	Density, λ (m)	Woody (trunk)*	Tree height below 5 m: 0.023 more than 5 m: 0.013
		Bamboo grove**	0.286
		Herbaceous**	0.031
	Drag coefficient, C_D		1.0
Manning's roughness coefficient, *n* ($1/m^{1/3}s$)**			Main channel: 0.028 Floodplains: 0.026
Downstream Water Level	2020 Flood	At peak flow rate*** Q = 1,561 m^3/s	Asahi River (11.0 KP): 5.232 m Hyakken River (12.8 KP): 5.960 m
	2018 Flood	At peak flow rate Q = 4,251 m^3/s	Asahi River 11.0 KP: 7.180 m Hyakken River 12.8 KP: 8.190 m
		STIV measurement time Q = 4,146 m^3/s	Asahi River 11.0 KP: 7.141 m Hyakken River 12.8 KP: 8.158 m

*Yoshida et al. (2018); **Maeno et al. (2005); ***STIV measurements were taken around the peak flow rate during the 2020 flooding

In the flood flow simulations, Manning's coefficient values for the bed roughness of the main channel and floodplains were assigned respectively as 0.028 and 0.026 $m^{-1/3}/s$ (Maeno et al., 2005; Yoshida et al., 2020a). However, the current study did not distinguish between the riverbed and the targeted weirs by roughness. Because porosity (γ_v) varies with vegetation species and floodplain conditions, a constant

value of 0.7 for the trees (branches and leaves) (Table 3.4) was used after checking the sensitivity of flow analysis through preliminary examination with γ_V of 0.6–0.8. The density values assigned herein (Table 3.4), particularly for woody and bamboo species, were reasonably confirmed in comparison to fieldwork estimates conducted by Yoshida et al. (2020a). In addition, average density was estimated by taking into account the spatially explicit vegetation distribution data in each computational mesh of the flood flow analyses (Figures 3.7b and 3.9b). Using ALB data, the proportion of each vegetation type presented in equation (11) was calculated.

$$\lambda_a = \alpha\lambda_h + \beta\lambda_w + \gamma\lambda_b,\ \alpha + \beta + \gamma = 1 \qquad (11)$$

In which, λ_a is the average vegetation density in each numerical mesh for flow resistance estimation; α, β and γ denote the ALB-derived proportion of herbaceous, woody and bamboo species, respectively, in each flow computational mesh; and λ_h, λ_w and λ_b represent constant density value assigned to herbaceous, woody and bamboo species, respectively. Those fixed values of densities were assigned by the earlier study of Maeno et al. (2005).

Based on earlier studies of flow resistance attributable to the riparian vegetation, the C_D value was inferred for three categories: 1.0 (Stoesser et al., 2003), 1.2 (Rameshwaran & Shiono, 2007), and 1.5 (Wilson et al., 2006). However, the computation results' variation considering different coefficient values is minimal for vegetation established in the targeted river reach (Yoshida et al., 2020a). Consequently, the value of 1.0 was assigned as a drag coefficient. Finally, the stream resistance was estimated based on the mixture distribution of the three targeted vegetation types in each numerical mesh.

3.5 Application

3.5.1 Longitudinal profile of water levels

Figure 3.17 presents a comparison of the left-bank-side and right-bank-side observed water levels profiles with the values simulated using the 3-D and 2-D models at peak flood stage in 2020 and 2018.

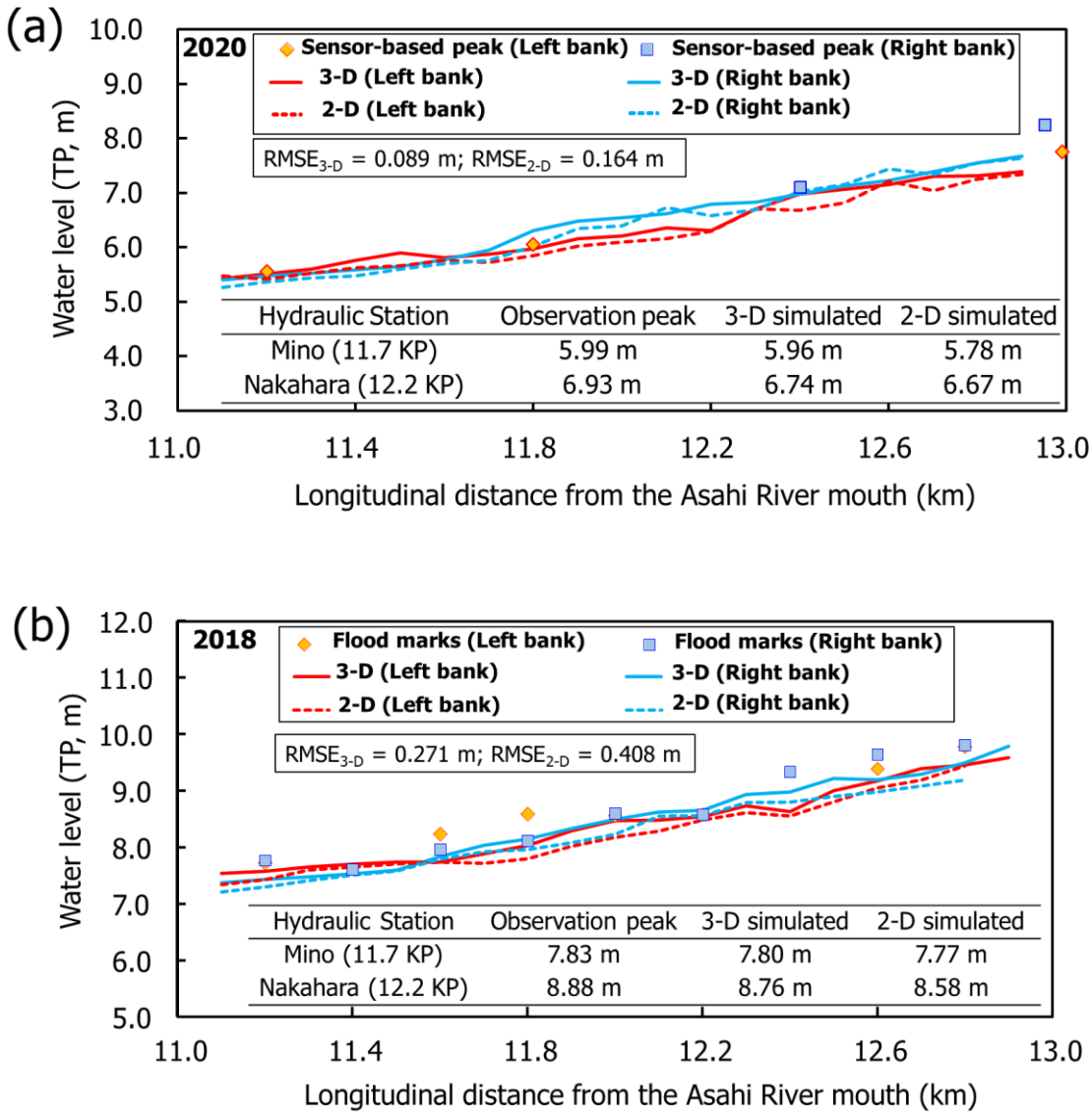

Figure 3.17 Observed and simulated water levels along the targeted reaches of the Asahi River at the time of the peak water-stage for flooding in (a) 2020 and (b) 2018. RMSE represents root-mean-square error.

As reference data, sensor-based (S&DL mini EC meter, 4821; OYO Corp., Japan) peak water levels at specific KP points are shown for the minor 2020 flooding (Figure 3.17a), whereas flood marks at both river banks are included for the more intense 2018 flooding (Figure 3.17b). During the 2020 flooding, the sensors recorded the water level every ten minutes. Both model simulations were reasonably consistent with the observed water levels (Figure 3.17a). This suggests that the 3-D model will perform acceptably at lower discharges.

In contrast, in the 2018 case with a higher flow, the 2-D simulated water level was approximately 0.5 m lower than the observed level upstream from 12.4 KP in the diversion area, but the recorded water levels were reproduced in both models downstream from 12.2 KP (Figure 3.17b). Although the results of the two simulations agreed well for both cases, root-mean-square error values estimated with respect to observed data (sensor/flood marks and water levels recorded at hydraulic gauging stations) show that the 3-D estimates slightly outperformed the 2-D results. Furthermore, from the case with excessive flooding, results showed that the 2-D simulated water level was a maximum of 0.30 m lower than the observed peak at the Nakahara hydraulic station, whereas the 3-D result was 0.12 m less than the observed. The gauging station at Nakahara is close to the targeted diversion weir. Therefore, such a significant relative difference was observed. However, the targeted weirs' shape and roughness coefficient can result in better water level reproduction, particularly for the 2018 flood modeling. In addition, the models' performance might have been influenced by the use of fixed λ values (Table 3.4) based on earlier research findings (Maeno et al., 2005; Yoshida et al., 2020a) because the present study did not locally survey densities of targeted vegetation species. Figure 3.18

presents a 2-D distribution of vegetation in underwater areas during peak flooding in 2020 and 2018, demonstrating that woody vegetation submergence conditions predominated in the 2018 flood event compared to 2020. Such a vegetation distribution, including leaves and branches, in the meshes of the flow computational domain facilitates accurate estimation of flow resistance, which can affect water level simulation.

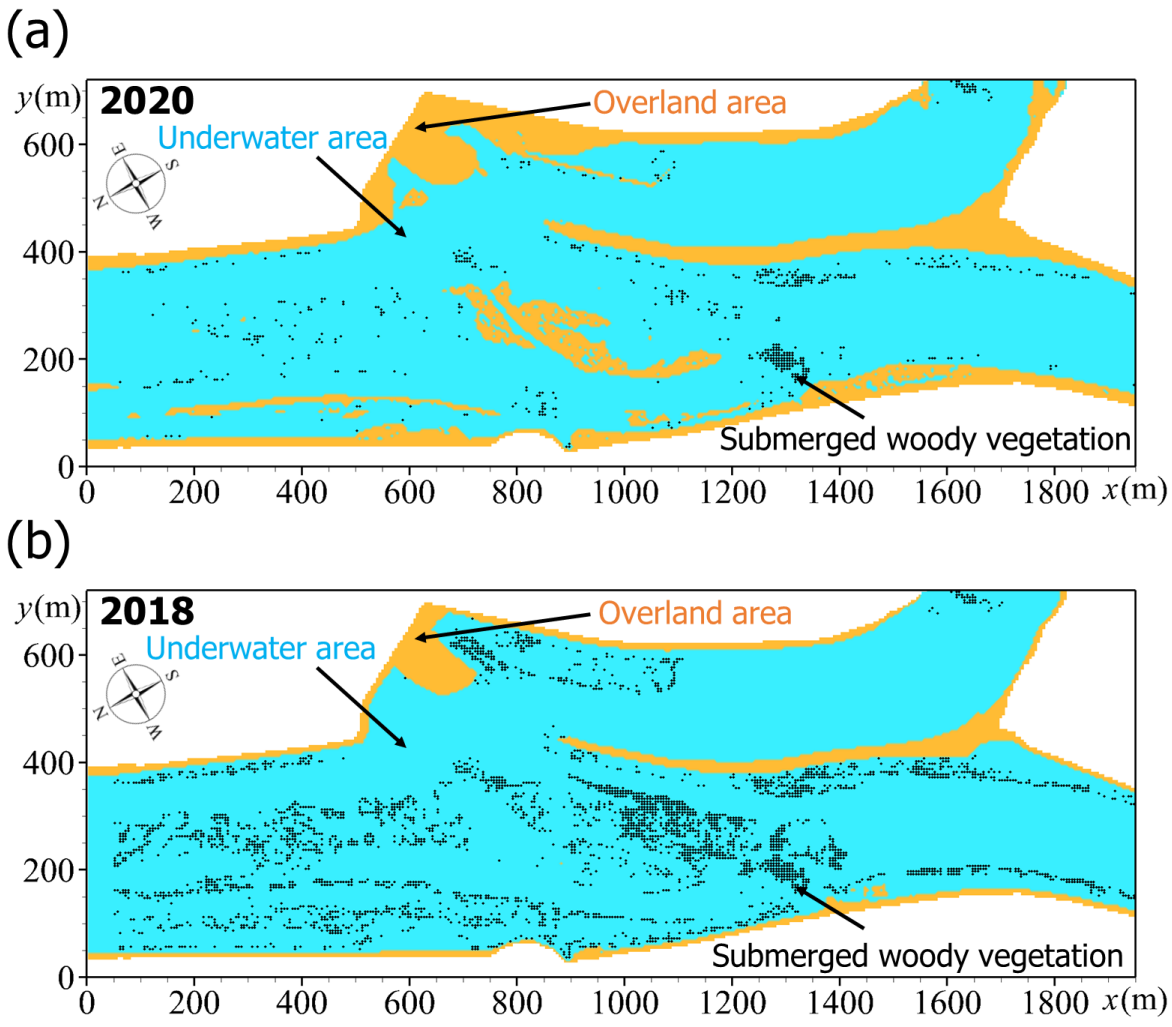

Figure 3.18 2-D distribution of submerged woody vegetation during peak stage of flooding in (a) 2020 and (b) 2018.

3.5.2 Depth-averaged flow fields and STIV comparisons

The analytical boundary of the Hyakken River was slightly different between the two

model simulations (Figure 3.19), but the change in flow regime caused by the diversion weir was not captured in 2-D modeling.

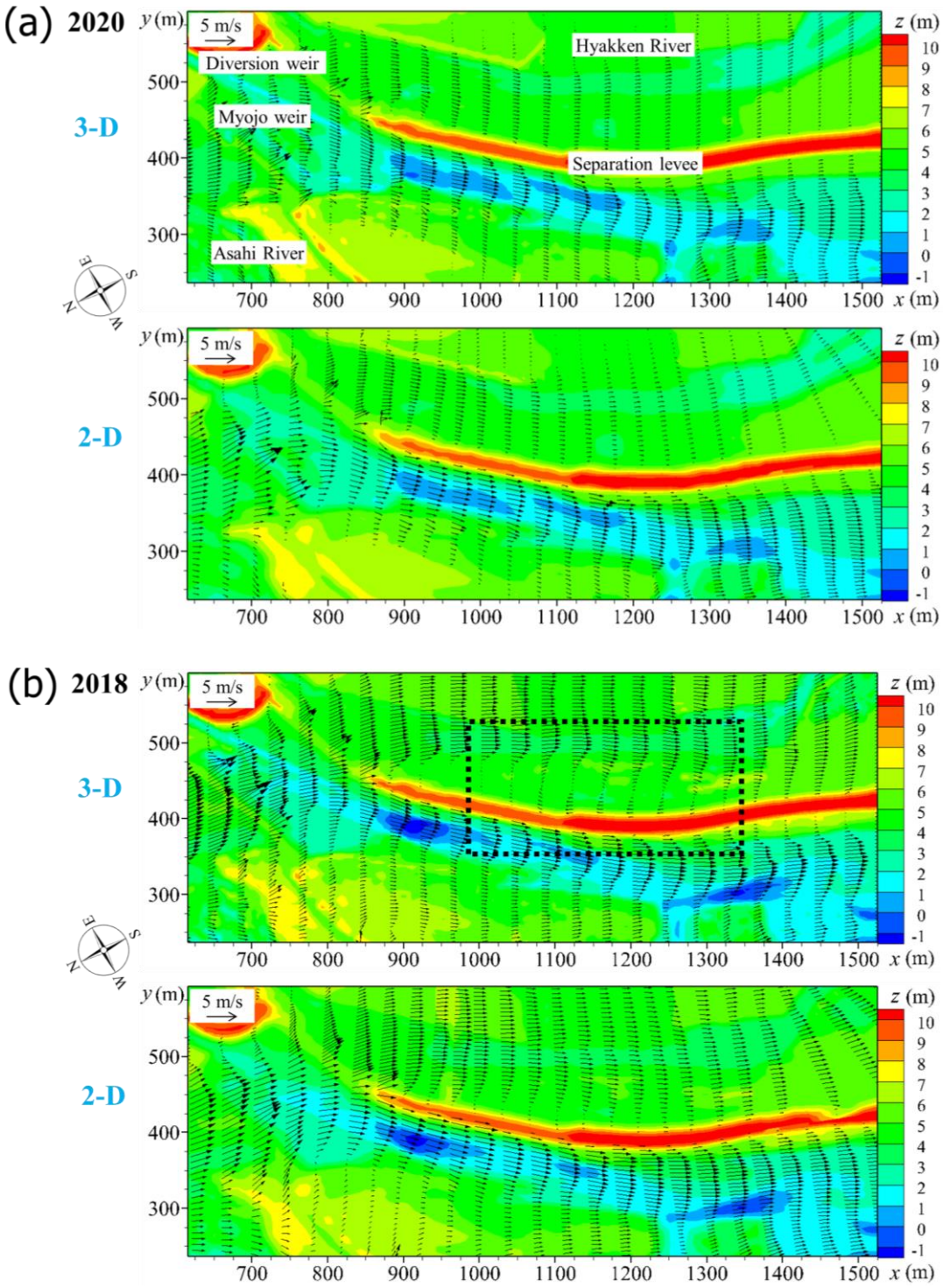

Figure 3.19 Depth-averaged flow velocity vectors at peak flooding in (a) 2020 and (b) 2018. Targeted section is depicted in Figure 3.4b.

Figure 3.19 depicts the depth-averaged flow velocity vectors for peak flooding in 2020 and 2018 using both models. For the 2020 case, the depth-averaged flow velocity vectors were remarkably similar in both models (Figure 3.19a), indicating the validity of the new 3-D model for shallow-water flow conditions. In contrast, for the high discharge case, 3-D simulation revealed a distinct separation vortex on the diversion side of the Hyakken River (black-dotted rectangle part; Figure 3.19b, top). The 2-D model could not reproduce such a flow regime (Figure 3.19b, bottom). This variation can be attributed to differences in the 3-D and 2-D coordinate systems, the estimation methods of eddy viscosity coefficient, and different discretisation methods for advection terms used in 3-D modeling.

Furthermore, Figure 3.20 presents a comparison of the cross-sectional distribution of surface velocity estimated using the STIV analysis (Figure 3.16) with the numerical results of flow velocities using the 3-D and 2-D models for both floods. Herein, the 2-D simulation result only showed the depth-averaged velocity distribution, whereas the proposed 3-D model additionally examined other surface and near-bed flow velocities. For the 2020 (Figure 3.20a) and 2018 (Figure 3.20b) flooding cases, respectively, one black line was added for the cross-sectional fixed bed elevation using 2019 and 2017 ALB data. Based on 3-D modeling, another grey-coloured line represents the water surface level in both cases. For the 2018 case (Figure 3.20b), the study confirmed the model-based water level as consistent with the surface level, shown in the CCTV image. Furthermore, for minor flooding in 2020 (Figure 3.20a), the 3-D model agreed well with the image-based findings, although both model-derived flow velocities were almost identical to the STIV-based estimation, with a few exceptions near both bank sides.

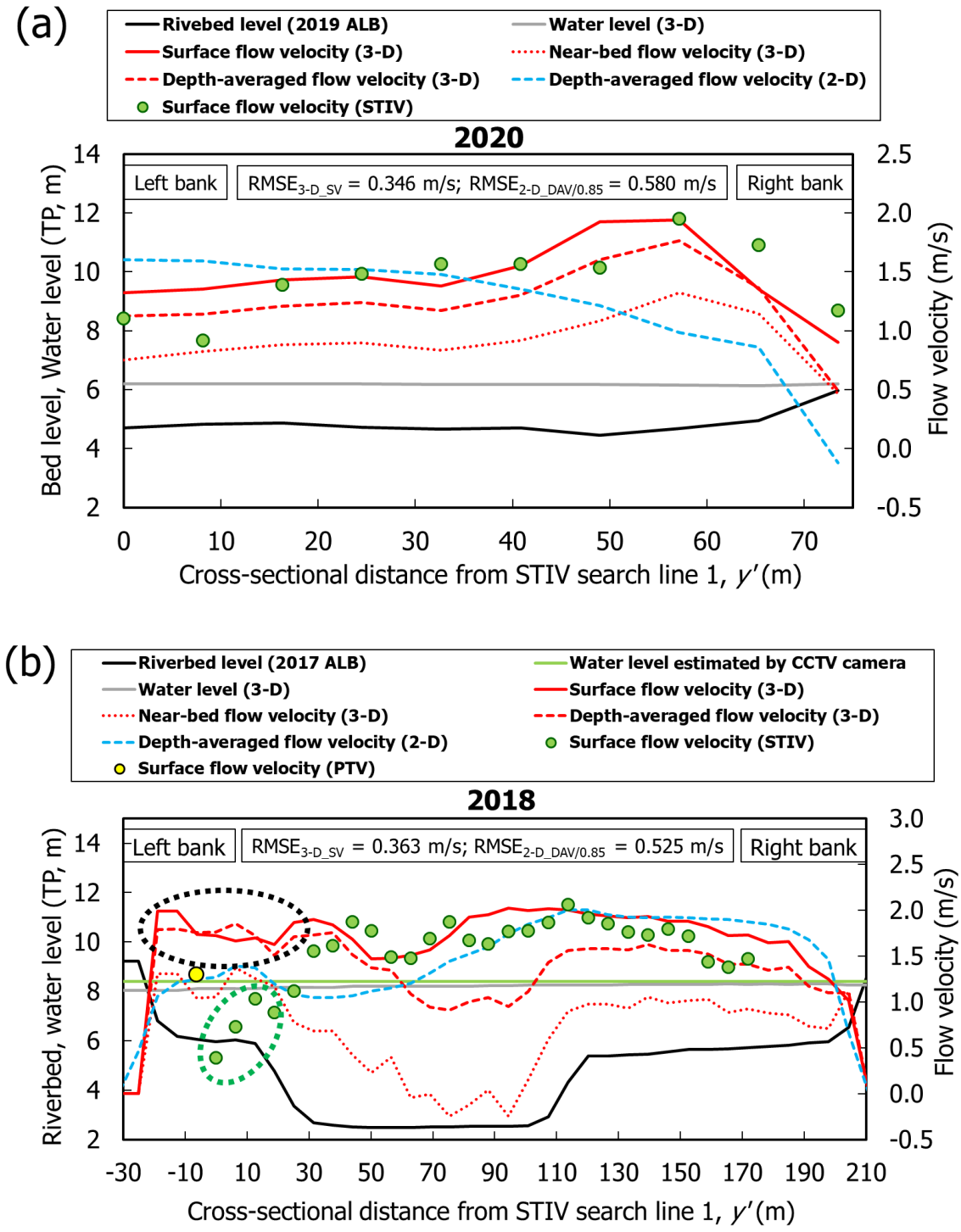

Figure 3.20 Cross-sectional distribution of flow velocities estimated using numerical simulations and STIV analysis (Figure 3.16): (a) 2020 flooding in the Hyakken River around the diversion weir's downstream side (12.2 KP) and (b) 2018 flooding in the Hyakken River at Ninoarate (12.8 KP). RMSEs were calculated with respect to STIV estimates. DAV, depth-averaged velocity; SV, surface velocity

In contrast, during the severe 2018 flooding, the STIV-derived surface flow velocity was not necessarily correct near the left-bank side (green-dotted enclosure; Figure 3.20b) because of transverse propagation of surface waves caused by a sudden change in bed elevation and water depth around the *Ninoarate* weir (Figure 3.16b). For such a flaw in STIV analysis, the surface flow velocity was estimated by particle tracking velocimetry (PTV) (Maas et al., 1993) approach, using floating objects such as individual driftwood, reasonably agreed with the model-based estimates. Furthermore, comparison of the imaging (STIV and PTV) estimation and the surface velocities simulated using 3-D model revealed that the simulated velocities on the left bank of the river were overestimated up to a cross-sectional distance of y' = 30 m (black-dotted enclosure; Figure 3.20b), but were nearly consistent towards the right-bank side, except for a few points. By contrast, for 2-D computation, the depth-averaged velocity was considerably lower on the river's left bank by the cross-sectional distance of y' = 70 m, and concentrated on the river's right side. However, in 2-D modeling, only depth-averaged velocities can be generated, which cannot be compared directly with STIV results or 3-D model-based findings, except for depth-averaged estimates. If the 2-D model-based results are converted to surface flow velocities by dividing by a typical velocity index of 0.85, then the results might overestimate the STIV-based surface velocities. Consequently, based on RMSE estimates (Figure 3.20), the 3-D simulated surface velocities are reasonably consistent with STIV estimates when compared to the 2-D numerical results.

3.5.3 Free-surface and near-bed flow fields

In addition, the 3-D model presents considerable advantages over the 2-D model in that it reveals the free-surface and near-bed flow fields. Figure 3.21 depicts a 3-D

horizontal flow field at the free-surface and near-bed surface ($\Delta z/2$ above the riverbed) for the targeted peak flooding cases around the diversion weir.

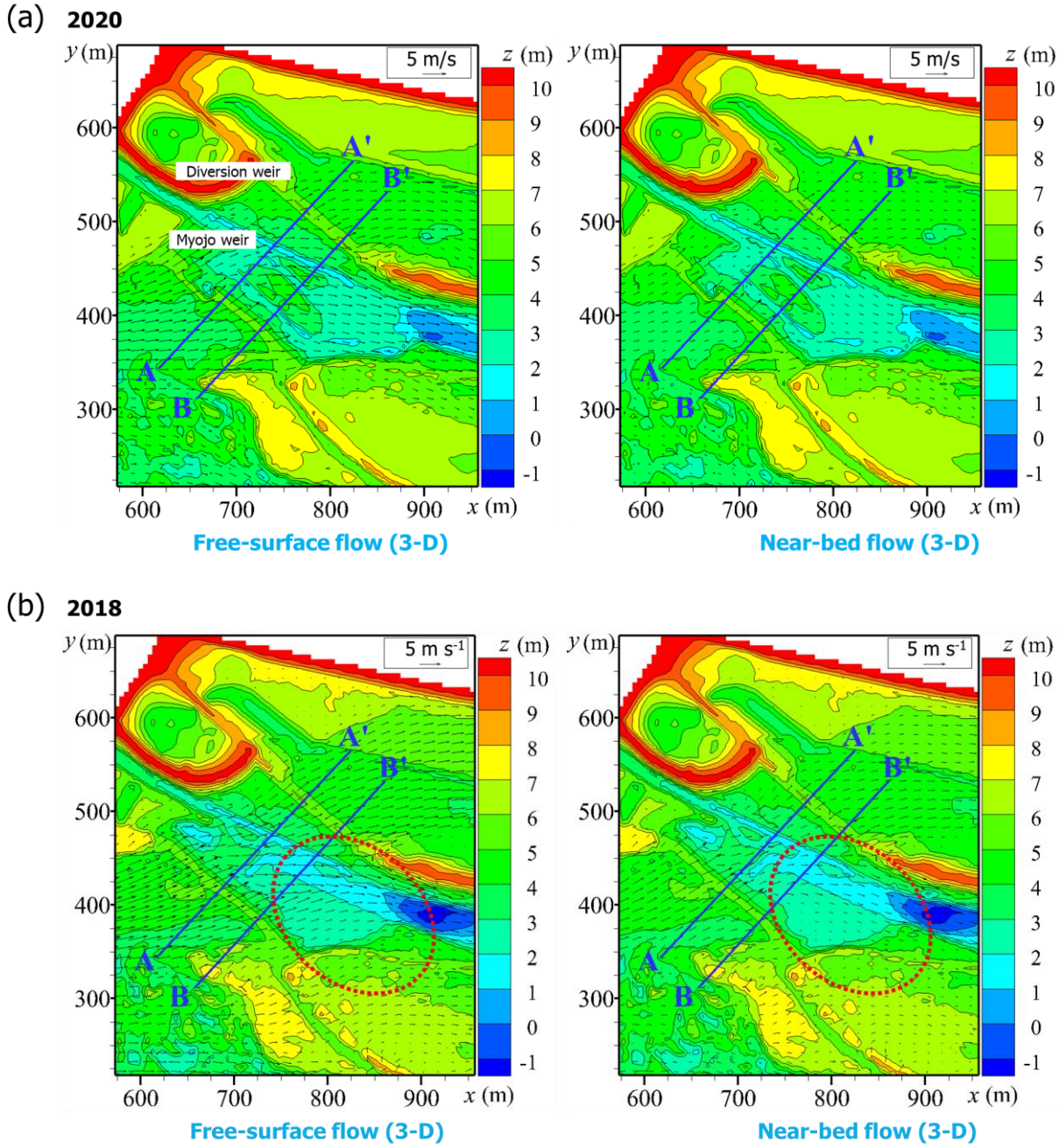

Figure 3.21 Horizontal flow fields of free-surface (left) and near-bed (right) flow using a 3-D model at peak flooding in (a) 2020 and (b) 2018. Targeted section is depicted in Figure 3.4b.

The results showed that the flow velocity, including its direction, differ considerably between the water surface and the bottom in the area surrounded by the red-dashed circle (Figure 3.21b).

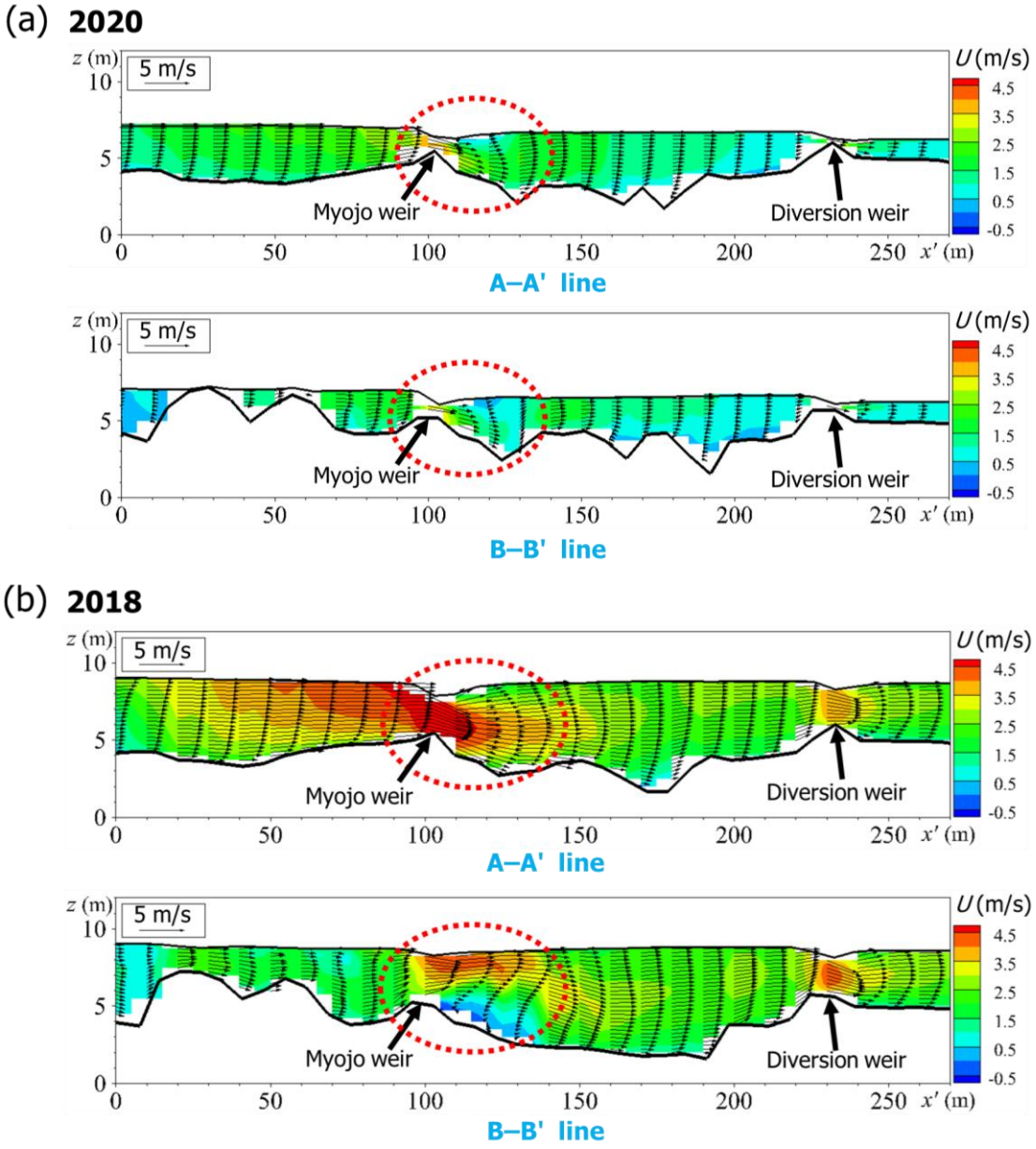

Figure 3.22 Vertical flow field during peak flooding in (a) 2020 and (b) 2018 using the 3-D model at the A–A' (top) and B–B' (bottom) sections depicted in Figure 3.21.

In addition, Figure 3.22 presents the vertical flow velocity vectors for the A-A' and B-

B' cross-sections (Figure 3.21) during both peak flooding events, revealing the formation of a 3-D flow regime with a mix of mainstream submergence and separation beneath the Myojo weir, as shown by the red-dotted circle. In general, when a flow forms a control section over a weir, flows of two types are known to occur downstream of the weir: "surface wave flow," by which the mainstream flows in waves near the water surface; and "plunging jet flow," by which the mainstream flows near the riverbed (Fritz & Hager, 1998). Particularly during the plunging jet flow, the strong current near the riverbed scours the area directly below the weir. Also, a risk exists of the weir collapsing. The A-A' cross-section in Figure 3.22(b) shows that the occurrence of submerged jet flow is simulated directly below the *Myojo* weir. This section coincides with the weir collapsed position in Figure 3.15(b). Therefore, the weir collapse during the 2018 flood might have been caused by such a submerged jet flow. The conventional 2-D model was unable to predict the 3-D flow regime around such structures.

Furthermore, Figure 3.23 shows that changing vegetation distribution had a significant impact on streamlines at both the free-surface and near-bed levels. Because of the higher flow resistance, streamlines around the C–C' section were separated into two paths in the cases of actual vegetation and only bamboo. In contrast, because of the lower resistance, streamlines were nearly parallel in the only woody case. Because of such effects on horizontal flow field distribution, the vertical flow field illustration (blue-dotted part; Figure 3.24) revealed that the flow velocity at the near-bed varied greatly with changing vegetation types. In contrast, such flow patterns with highlighted vegetation distribution cannot be apparent in 2-D modeling. The superiority of the proposed 3-D model was confirmed in this respect.

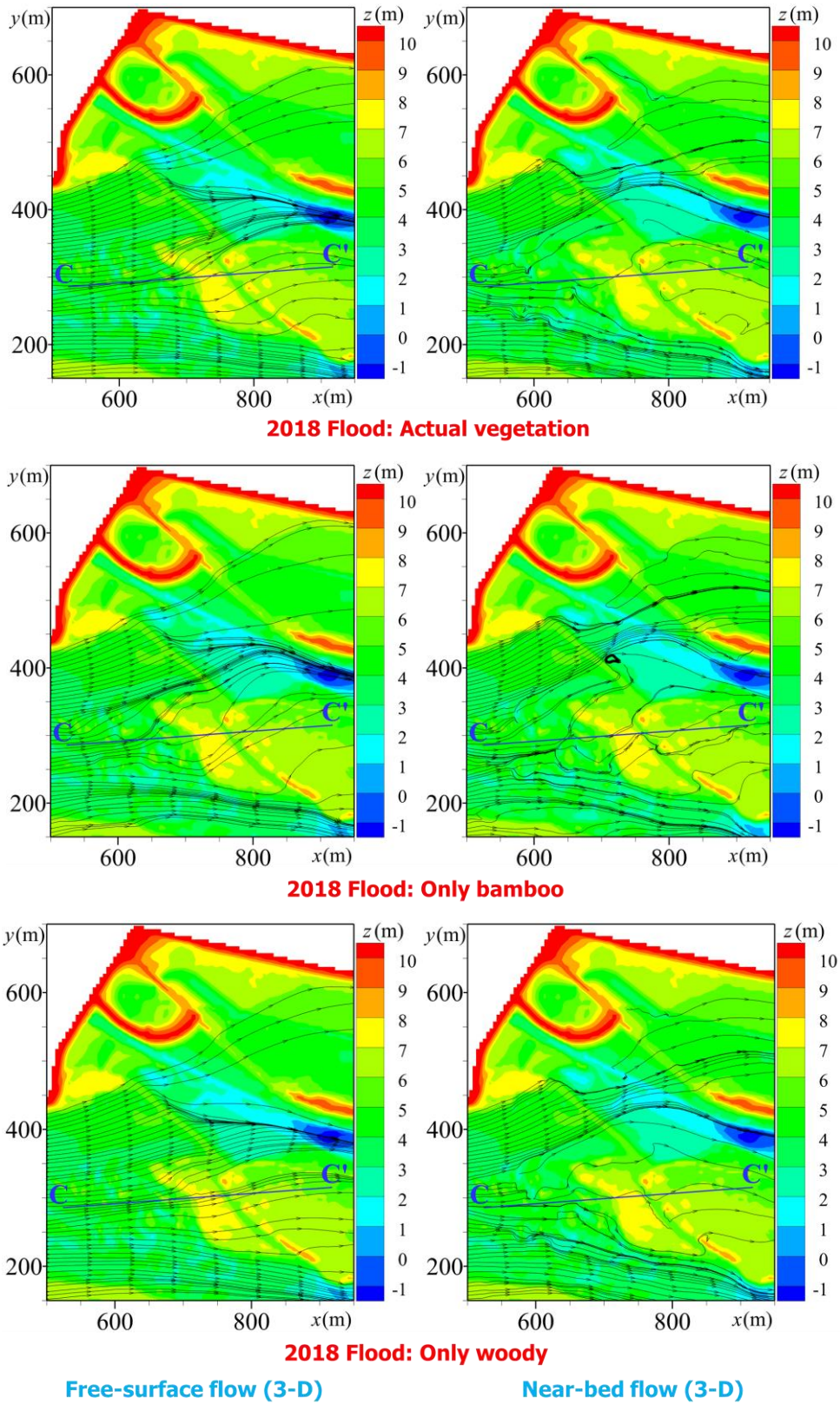

Figure 3.23 Horizontal streamlines around different vegetation types using 3-D model at peak flooding in 2018.

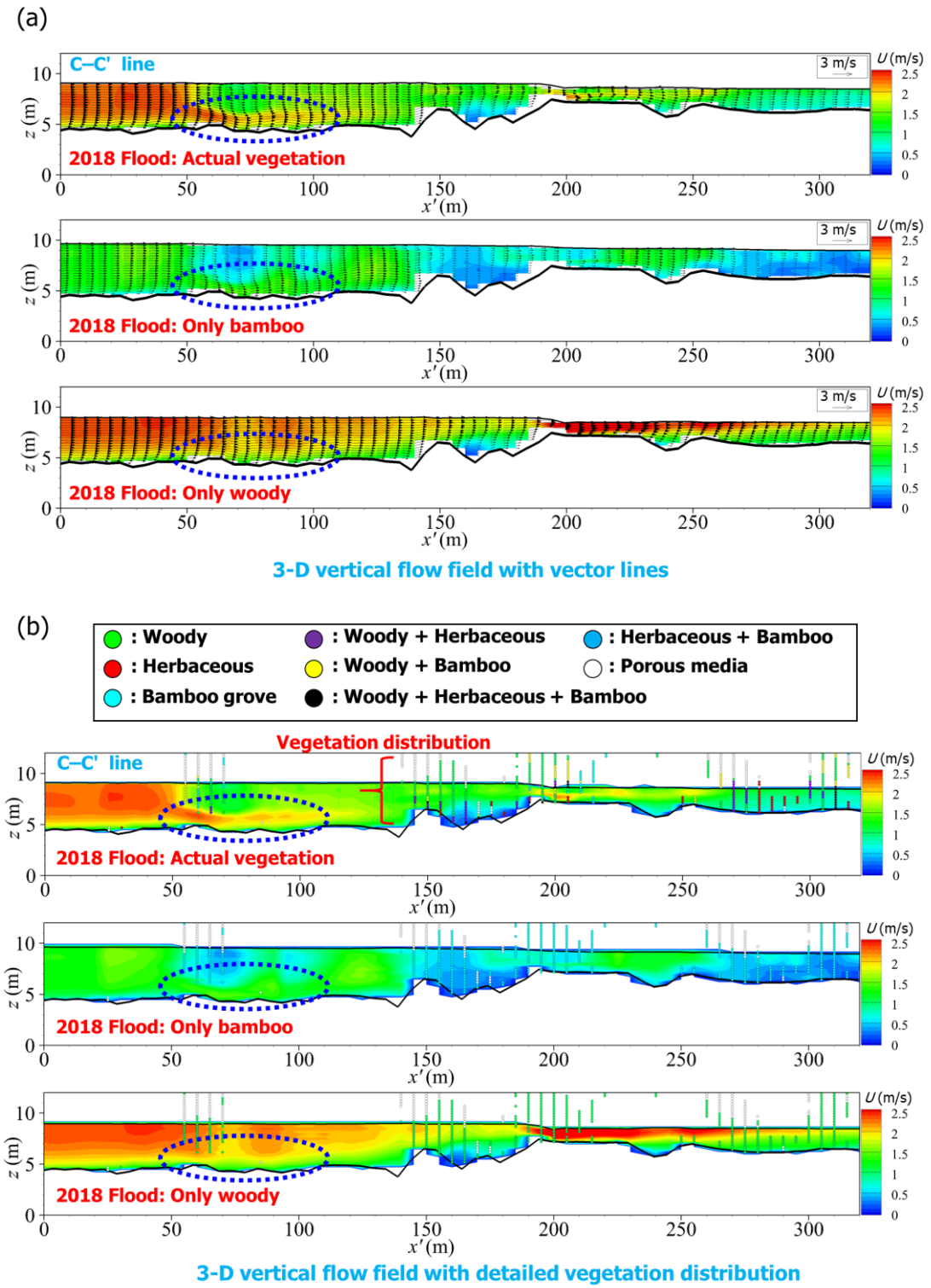

Figure 3.24 Vertical flow field around different vegetation types with (a) vector lines and (b) detailed vegetation distribution during peak flooding in 2018 using the 3-D model at the C–C' section depicted in Figure 3.23; color-circled points represent the targeted vegetation types.

3.5.4 Distributary discharge

The 3-D and 2-D numerical simulations examined the diversion discharge to the distributary Hyakken River under various flow rate conditions. The computational conditions are the same as those presented in Table 3.4. The analysis flow rate conditions are presented in Table 3.5. Herein, to analyse effects of the failure of the *Myojo* weir (Figure 3.15b) on the distributary flow, the topographic conditions were examined numerically using the current ALB datasets.

Table 3.5 Diversion discharges for the Hyakken River simulated using flow models under various analysis conditions

Before diversion Flow, Q (m^3/s)	**Water level in Asahi River at 11.0 KP (m)**	**Water level in Hyakken River at 12.8 KP (m)**	**3-D Diversion flow rate (m^3/s)**		**2-D Diversion flow rate (m^3/s)**	
			2017 ALB	2019 ALB	2017 ALB	2019 ALB
1,000	4.822	5.355	8	16	30	36
1,561*	5.232	5.960	–	195	–	237
2,000	5.552	6.402	341	340	353	352
3,000	6.282	7.314	668	750	704	760
4,251**	7.180	8.190	1,214	1,262	1,203	1,308
5,000	7.676	8.682	1,552	1,601	1,505	1,641
5,800	8.205	9.117	1,865	2,007	1,869	2,001

*****Peak discharge in 2020 flooding**;** **Peak discharge in 2018 flooding

Figure 3.25 depicts the comparison of the distributary discharge analyzed using 3-D and 2-D models for various flow conditions and targeted peak floods, along with the planned discharge flowing through the targeted domain during flooding, as designated by the Asahi River office. Results demonstrated that the flow rate differences increased by a few per cent after the *Myojo* weir was damaged and after

the riverbed deformed during the 2018 flooding, but no marked change was found from that before the weir's failure.

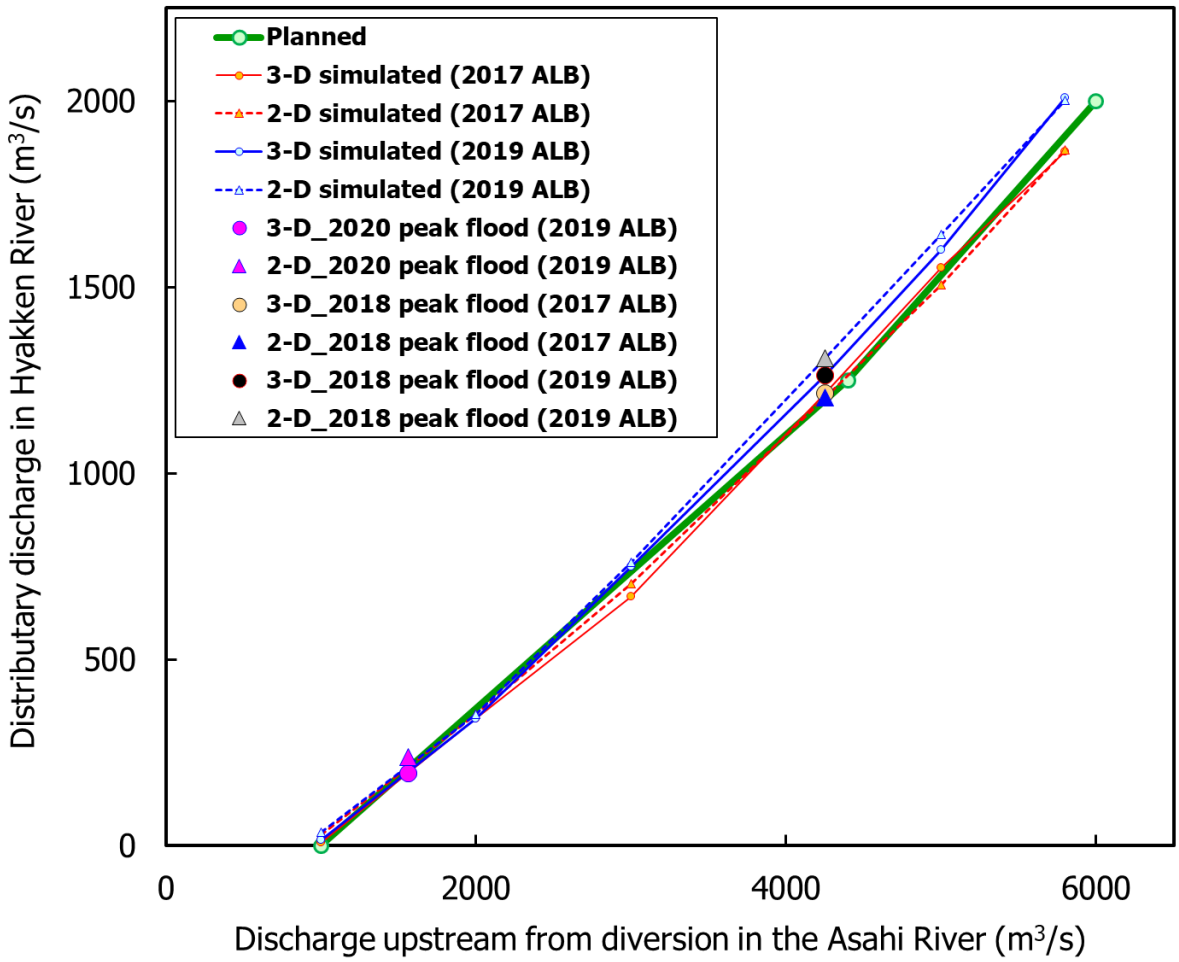

Figure 3.25 Comparison of simulated distributary discharges for various flow conditions and peak floods in 2020 and 2018 (Table 3.5) with planned (as designated by the Asahi River office) values.

In addition, both the 3-D and 2-D model-based findings showed good agreement with the planned flow distribution, thereby confirming the validity of the 3-D model. Figure 3.25 also compares the planned values with the diversion discharge to the distributary Hyakken River for the targeted peak floods in 2020 and 2018, as

calculated using the new 3-D and conventional 2-D flow models under the same computation conditions (Table 3.4) and individual ALB datasets. Although the results of the two models agreed reasonably well in both targeted flooding cases, the 3-D simulation was closer to the reference planned discharge values when the weir and topographic conditions before and after flooding were taken into account. Overall, the diversion can occur as expected under the current vegetation scenario.

3.6 Conclusions and Future Research Directions

For this study, a 3-D flood flow model with k–ε parameterization of turbulence was constructed based on a porous model considering the vegetation distribution in the targeted river reaches. Accuracy of the proposed model was tested using field measurements, STIV data, and existing depth-averaged flow model-based results. Using ALB data, a 3-D vegetation distribution model related to flow resistance was developed for the targeted domain. For minor flooding, the 3-D model agreed well with field observations and 2-D hydrodynamic model-based findings. In contrast, the 3-D model reproduced the flow regime better than the existing 2-D model at higher flows. The current simulation also reproduced the vertical flow distribution, as well as free surface and near-bed flow fields around the targeted hydraulic structures. Furthermore, flow rate analysis conducted with changing flow conditions revealed that the 3-D model agreed well with the planned flow rate when compared to 2-D model results. Despite the conclusions presented above, the 3-D model used for this study did not account for the wash-out and lodging conditions of the vegetation or for the riverbed deformation. Therefore, future research related to the current study must include vegetation dynamics and topographical change analysis during flooding in the proposed 3-D flood modeling to better elucidate fluvial response. Furthermore,

although the point density of the current ALB data was reasonable for generating 3-D vegetation data, it would be preferable to use UAV-borne LiDAR data with a more detailed point density (Chapter 2; Islam et al., 2022) to ascertain the porosity and proportion of vegetation branches and leaves.

CHAPTER 4

Concluding Remarks

This research presents the first experimental evidence of the feasibility of remotely sensing riverbed deformation, submerged hydraulic structure, flow and riparian vegetation quantities using advanced UAV-based green LiDAR and deep learning-based imaging velocimetry, as well as highlighting some key facts for future studies. The efficacy of these methodologies was determined by comparing remotely sensed estimates to ground-truth measurements and hydrodynamic model-based results. Furthermore, when surface flow velocity estimates from AI-assisted STIV analysis were multiplied by the typical conversion factor of 0.85, they agreed reasonably (R^2 = 0.742–0.959) with estimated RMSEs of 0.048–0.247 m/s in comparison to both current meter measurements and depth-averaged model-derived calculations. The river discharges calculated using remotely sensed velocities and depths at multiple cross-sections were compared to benchmarked field and model estimates, demonstrating that the UAV-based approach produced reasonable quantity to verify upstream boundary discharge required in depth-averaged flow modeling. Therefore, using remotely sensed information to extract river flow as verification data in hydrodynamic–numerical modeling would be a distinctive technique. Using GLS-based data filtering algorithms, the study also classified land cover features with OA of 80%, and approximation of 0.5–1.5 m per year for vegetation growth that varies among species. Although the LiDAR and imaging systems used in this study accomplished their objectives, further development and testing of both sensors is required before these approaches can be widely used. To summarize, current remote sensing techniques can be regarded as cost-effective and well-proven tools for

characterizing hydraulic and floodplain vegetation attributes, which will be useful for streamflow simulation and desirable ecosystem management tasks.

This study also evaluates the performance of a newly constructed porous model-based (k–ε parameterization of turbulence) 3-D numerical modeling of floods in river corridor with complex vegetation quantified using airborne LiDAR imagery. The proposed model's accuracy was evaluated using field measurements, STIV data, and existing depth-averaged flow model-based results. Using ALB data, a 3-D vegetation distribution model related to flow resistance was developed for the targeted domain. The 3-D model agreed well with field observations and 2-D hydrodynamic model-based findings for minor flooding. At higher flows, however, the 3-D model reproduced the flow regime better than the existing 2-D model. The proposed model outperformed the traditional depth-averaged flow model by depicting the vertical flow distribution as well as free surface and near-bed flow fields around the targeted structure. The 3-D model estimates also revealed that differing vegetation distribution had a significant effect on streamlines at both the free-surface and near-bed levels. Furthermore, flow rate analysis was performed revealing that the diversion discharge designed using the proposed model is feasible with the current riverbed and vegetation conditions. The study also suggested that, while the point density of current airborne LiDAR data was adequate for generating 3-D vegetation data, using UAV-borne green LiDAR data with a more detailed point density would be preferable for determining the porosity and proportion of vegetation branches and leaves. To conclude, the current findings can help policymakers develop a balanced and rational scenario for flood control measures that take best vegetation management practices around river corridors into account.

Acknowledgements

It is the blessings of the creator (Allah SWT) who keep me healthy enough to complete my PhD study in Japan.

I would like to thank my supervisor, Associate Professor Dr. Keisuke YOSHIDA, Graduate School of Environmental and Life Science, Okayama University, Japan, for his kind and scholarly guidance throughout the PhD study. Talking with him was always enlightening and enjoyable.

I would also like to thank my another mentor, Professor Dr. Satoshi NISHIYAMA, Graduate School of Environmental and Life Science, Okayama University, Japan, for his insightful direction throughout my PhD research.

Thanks to Associate Professor Dr. Yuki KAJIKAWA, Graduate School of Engineering, Tottori University, Japan, for his valuable direction throughout the PhD research.

Thanks also to my academic co-supervisors, Professor Dr. Shiro MAENO and Associate Professor Dr. Ryosuke AKOH, Graduate School of Environmental and Life Science, Okayama University, Japan, for their suggestions throughout the course.

Special thanks to all members of the Hydraulic Engineering Laboratory, Graduate School of Environmental and Life Science, Okayama University, Japan, for their kind cooperation and for making my student life enjoyable.

Also, thanks to my family for being the best companions in Japan and for encouraging and supporting my scientific journey.

I would also like to thank the Chugoku Regional Development Bureau, Ministry of Land, Infrastructure, Transport, and Tourism, and Pasco Corporation, Japan

for providing the necessary data to complete this study.

I am especially grateful to the Japan Society for the Promotion of Science (JSPS; KAKENHI Grant No. 18K04370) and the Chugoku Kensetsu Kousaikai for partly contributing to the funding of my PhD research.

I would finally like to thank the Ministry of Education, Culture, Sports, Science and Technology (MEXT) for providing financial assistance to enable me to live properly and continue my studies in Japan.

References

Aberle, J., & Järvelä, J. (2013). Flow resistance of emergent rigid and flexible floodplain vegetation. *Journal of Hydraulic Research, 51*(1), 33-45. https://doi.org/10.1080/00221686.2012.754795

Anjum, N., Tanaka, N. (2020). Hydrodynamics of longitudinally discontinuous, vertically double layered and partially covered rigid vegetation patches in open channel flow. *River Research and Applications 36*(1), 115-127. https://doi.org/10.1002/rra.3546

Barker, J. R., Pasternack, G. B., Bratovich, P. M., Massa, D. A., Wyrick, J. R., & Johnson, T. R. (2018). Kayak drifter surface velocity observation for 2-D hydraulic model validation. *River Research and Applications*, *34*(2), 124-134. https://doi.org/10.1002/rra.3238

Bjerklie, D. M., Birkett, C. M., Jones, J. W., Carabajal, C., Rover, J. A., Fulton, J. W., & Garambois, P. A. (2018). Satellite remote sensing estimation of river discharge: Application to the Yukon River Alaska. *Journal of Hydrology*, *561*, 1000-1018. https://doi.org/10.1016/j.jhydrol.2018.04.005

Brito, M., Fernandes, J., & Leal, J. B. (2016). Porous media approach for RANS simulation of compound open-channel flows with submerged vegetated floodplains. *Environmental Fluid Mechanics*, *16*(6), 1247-1266. https://doi.org/10.1007/s10652-016-9481-0

Corenblit, D., Tabacchi, E., Steiger, J., & Gurnell, A. M. (2007). Reciprocal interactions and adjustments between fluvial landforms and vegetation dynamics in river corridors: a review of complementary approaches. *Earth-Science Reviews, 84*(1-2), 56-86. https://doi.org/10.1016/j.earscirev.2007.05.004

Delefortrie, S., Saey, T., De Pue, J., Van De Vijver, E., De Smedt, P., & Van Meirvenne, M. (2016). Evaluating corrections for a horizontal offset between sensor and position data for surveys on land. *Precision Agriculture, 17,* 349–364. https://doi.org/10.1007/s11119-015-9423-8

Dorn, M., Filwarny, J. O., & Wieser, M. (2017). Inertially-aided RTK based on tightly-coupled integration using low-cost GNSS receivers. In *2017 European Navigation Conference (ENC), IEEE,* pp. 186–197. https://doi.org/10.1109/EURONAV.2017.7954208

Fathi-Moghadam, M., Kashefipour, M., Ebrahimi, N., & Emamgholizadeh, S. (2011). Physical and numerical modeling of submerged vegetation roughness in rivers and flood plains. *Journal of Hydrologic Engineering*, *16*(11), 858-864. https://doi.org/10.1061/(ASCE)HE.1943-5584.0000381

Fischer-Antze, T., Stoesser, T., Bates, P., & Olsen, N. R. B. (2001). 3-D numerical modelling of open-channel flow with submerged vegetation. *Journal of Hydraulic Research*, *39*(3), 303-310. https://doi.org/10.1080/00221680109499833

Forzieri, G., Guarnieri, L., Vivoni, E. R., Castelli, F., & Preti, F. (2011). Spectral-ALS data fusion for different roughness parameterizations of forested floodplains. *River Research and Applications, 27*(7), 826-840. https://doi.org/10.1002/rra.1398

Fritz, H. M., & Hager, W. H. (1998). Hydraulics of embankment weirs. *Journal of Hydraulic Engineering*, *124*(9), 963-971. https://doi.org/10.1061/(ASCE)0733-9429(1998)124:9(963)

Fujikane, M., Chino, T., Maeno, S. (2016). Flood control plan for the Asahi River bifurcation point using a fixed weir constructed in the Edo period. *In Proceeding of IAHR-APD 2016, Sri Lanka*.

Fujita, I., Notoya, Y., Tani, K., & Tateguchi, S. (2019). Efficient and accurate estimation of water surface velocity in STIV. *Environmental Fluid Mechanics, 19*(5), 1363-1378. https://doi.org/10.1007/s10652-018-9651-3

Fujita, I., Watanabe, H., & Tsubaki, R. (2007). Development of a non-intrusive and efficient flow monitoring technique: The space-time image velocimetry (STIV). *International Journal of River Basin Management*, *5*(2), 105-114. https://doi.org/10.1080/15715124.2007.9635310

Fujita, I., Watanabe, K., Iguchi, M., & Hasegawa, M. (2020). Improvement of STIV technique using deep learning. *Journal of Japan Society of Civil Engineers, Ser. B1 (Hydraulic Engineering)*, *76*(2), I_991-I_996 (in Japanese with English abstract). https://doi.org/10.2208/jscejhe.76.2_I_991

Geerling, G. W., Labrador-Garcia, M., Clevers, J. G. P. W., Ragas, A. M. J., & Smits, A. J. M. (2007). Classification of floodplain vegetation by data fusion of spectral (CASI) and LiDAR data. *International Journal of Remote Sensing, 28*(19), 4263-4284. https://doi.org/10.1080/01431160701241720

Gordon, R. L. (1989). Acoustic measurement of river discharge. *journal of hydraulic Engineering*, *115*(7), 925-936. https://doi.org/10.1061/(ASCE)0733-9429(1989)115:7(925)

Gurnell, A. (2014). Plants as river system engineers. *Earth Surface Processes and Landforms, 39*(1), 4-25. https://doi.org/10.1002/esp.3397

Helsel, D. R.; Hirsch, R. M. (2002). Statistical Methods in Water Resources (Techniques of Water-Resources Investigations of the United States Geological Survey, Book 4, Hydrologic Analysis and Interpretation, Chapter A3). *U.S. Geological Survey*, 1-524. https://doi.org/10.3133/twri04A3

Hirt, C. W., & Sicilian, J. M. (1985). A Porosity Technique for the Definition Obstacle in Rectangular Cell Meshes, Flow Science, Inc. *Los Alamos, New Mexico,* 450-469.

Islam, M. T., Yoshida, K., Nishiyama, S., Sakai, K., & Tsuda, T. (2022). Characterizing vegetated rivers using novel unmanned aerial vehicle-borne topo-bathymetric green lidar: Seasonal applications and challenges. *River Research and Applications, 38*(1), 44-58. https://doi.org/10.1002/rra.3875

Kaeser, A. J., Litts, T. L., & Tracy, T. W. (2013). Using low-cost side-scan sonar for benthic mapping throughout the lower Flint River, Georgia, USA. *River Research and Applications*, *29*(5), 634-644. https://doi.org/10.1002/rra.2556

Kinzel, P. J., Legleiter, C. J., and Grams, P. E. (2021). Field evaluation of a compact, polarizing topo-bathymetric LiDAR across a range of river conditions. *River Research and Applications, 37*(4), 531-543. https://doi.org/10.1002/rra.3771

Kinzel, P. J., Wright, C. W., Nelson, J. M., & Burman, A. R. (2007). Evaluation of an experimental LiDAR for surveying a shallow, braided, sand-bedded river. *Journal of Hydraulic Engineering, 133*(7), 838-842. https://doi.org/10.1061/(ASCE)0733-9429(2007)133:7(838)

Kuhnle, R. A., Jia, Y. and Alonso, V. (2008). Measure and simulated flow near a submerged spur dike, *Journal of Hydraulic Engineering*, ASCE, 134(7), 916-924. https://doi.org/10.1061/(ASCE)0733-9429(2008)134:7(916)

Legleiter, C. J., & Kinzel, P. J. (2021). Improving Remotely Sensed River Bathymetry by Image-Averaging. *Water Resources Research*, *57*(3), e2020WR028795. https://doi.org/10.1029/2020WR028795

Legleiter, C. J., Kinzel, P. J., & Nelson, J. M. (2017). Remote measurement of river discharge using thermal particle image velocimetry (PIV) and various sources of

bathymetric information. *Journal of Hydrology*, *554*, 490-506. https://doi.org/10.1016/j.jhydrol.2017.09.004

Li, C. W., & Zeng, C. (2009). 3-D numerical modelling of flow divisions at open channel junctions with or without vegetation. *Advances in Water Resources*, *32*(1), 49-60. https://doi.org/10.1016/j.advwatres.2008.09.005

Li, Y., Liu, Y., & Teng, B. (2006). Porous effect parameter of thin permeable plates. *Coastal Engineering Journal*, *48*(04), 309-336. https://doi.org/10.1142/S0578563406001441

López, F., & García, M. (1998). Open-channel flow through simulated vegetation: Suspended sediment transport modeling. *Water resources research*, *34*(9), 2341-2352. https://doi.org/10.1029/98WR01922

Maas, H. G., Gruen, A., & Papantoniou, D. (1993). Particle tracking velocimetry in three-dimensional flows. *Experiments in fluids,* *15*(2), 133-146. https://doi.org/10.1007/BF00223406

Maeno, S., & Watanabe, S. (2008). Field experiment to restore a gravel bar and control growth of trees in the Asahi River. *International Journal of River Basin Management*, *6*(3), 225-232. https://doi.org/10.1080/15715124.2008.9635350

Maeno, S., Watanabe, A., & Fujitsuka, Y. (2005). Improvement of modeling of flow analysis using easily obtained vegetation characteristic. *Journal of Hydraulic, Coastal and Environmental Engineering, II-73*, 91-104 (in Japanese with English abstract). https://doi.org/10.2208/jscej.2005.803_91

Mandlburger, G., Hauer, C., Wieser, M., & Pfeifer, N. (2015). Topo-bathymetric LiDAR for monitoring river morphodynamics and instream habitats – A case study at the Pielach River. *Remote Sensing,* *7*(5), 6160-6195. https://doi.org/10.3390/rs70506160

Mandlburger, G., Pfennigbauer, M., Schwarz, R., Flöry, S., & Nussbaumer, L. (2020). Concept and performance evaluation of a novel UAV-borne topo-bathymetric LiDAR sensor. *Remote Sensing, 12*(6), 986. https://doi.org/10.3390/rs12060986

Mandlburger, G., Pfennigbauer, M., Wieser, M., Riegl, U., & Pfeifer, N. (2016). Evaluation of a novel UAV-borne topo-bathymetric laser profiler. *The International Archives of Photogrammetry, Remote Sensing and Spatial Information Sciences, 41,* 933. https://doi.org/10.5194/isprs-archives-XLI-B1-933-2016

Manners, R., Schmidt, J., & Wheaton, J. M. (2013). Multiscalar model for the determination of spatially explicit riparian vegetation roughness. *Journal of Geophysical Research: Earth Surface, 118*(1), 65-83. https://doi.org/10.1029/2011JF002188

Mano, K., Sakai, K., Tachibana, K., Sakita, K., & Nishiyama, S. (2020). The measurement accuracy and measurement characteristics of green LiDAR drone. *The International Archives of Photogrammetry, Remote Sensing and Spatial Information Sciences, 43*, 479-483. https://doi.org/10.5194/isprs-archives-XLIII-B1-2020-479-2020

Mason, D. C., Cobby, D. M., Horritt, M. S., & Bates, P. D. (2003). Floodplain friction parameterization in two-dimensional river flood models using vegetation heights derived from airborne scanning laser altimetry. *Hydrological Processes, 17*(9), 1711-1732. https://doi.org/10.1002/hyp.1270

Ministry of the Environment, Ministry of Education, Culture, Sports, Science and Technology, Ministry of Agriculture, Forestry and Fisheries, Ministry of Land, Infrastructure, Transport and Tourism, Japan Meteorological Agency. (2018). *Synthesis report on observations, projections and impact assessments of climate*

change, 2018: Climate change in Japan and its impacts. https://www.env.go.jp/earth/tekiou/pamph2018_full_Eng.pdf

Mooney, H.A., Cleland, E.E. (2001). The evolutionary impact of invasive species. *Proceedings of the National Academy of Sciences 98*(10), 5446-5451. https://doi.org/10.1073/pnas.091093398

Mueller, D. S., Wagner, C. R., Rehmel, M. S., Oberg, K. A., & Rainville, F. (2013). Measuring discharge with acoustic Doppler current profilers from a moving boat. *U.S. Geological Survey Techniques and Methods, A22,* 95. https://doi.org/10.3133/tm3A22

Nepf, H. M. (2012a). Flow and transport in regions with aquatic vegetation. *Annual review of fluid mechanics, 44*, 123-142. https://doi.org/10.1146/annurev-fluid-120710-101048

Nepf, H. M. (2012b). Hydrodynamics of vegetated channels. *Journal of Hydraulic Research*, *50*(3), 262-279. https://doi.org/10.1080/00221686.2012.696559

Rameshwaran, P., & Shiono, K. (2007). Quasi two-dimensional model for straight overbank flows through emergent. *Journal of Hydraulic Research, 45*(3), 302-315. https://doi.org/10.1080/00221686.2007.9521765

Rantz, S. E., & Others, A. (1982). Measurement and Computation of Streamflow: Volume 1. Measurement of Stage and Discharge. *U.S. Geological Survey Water-Supply Paper, 2175,* 1-284. https://doi.org/10.3133/wsp2175

Rickenmann, D., and Recking, A. (2011). Evaluation of flow resistance in gravel-bed rivers through a large field data set. *Water Resources Research, 47*(W07538), 1-22. https://doi.org/10.1029/2010WR009793

Rodi, W. (Ed.). (2000). Turbulence Models and Their Application in Hydraulics*: A state-of-the-art review* (3rd ed.). Routledge, London. https://doi.org/10.1201/9780203734896

Schiermeier, Q. (2011). Increased flood risk linked to global warming: likelihood of extreme rainfall may have been doubled by rising greenhouse-gas levels. *Nature, 470*(7334), 316-317. https://doi.org/10.1038/470316a

Shu, C. W. (2003). High-order finite difference and finite volume WENO schemes and discontinuous Galerkin methods for CFD. *International Journal of Computational Fluid Dynamics*, *17*(2), 107-118. https://doi.org/10.1080/1061856031000104851

Stoesser, T., Kim, S. J., & Diplas, P. (2010). Turbulent flow through idealised emergent vegetation. *Journal of Hydraulic Engineering, 136*(12), 1003-1017. https://doi.org/10.1061/(ASCE)HY.1943-7900.0000153

Stoesser, T., Wilson, C. A. M. E., Bates, P. D., & Dittrich, A. (2003). Application of a 3-D numerical model to a river with vegetated floodplains. *Journal of Hydroinformatics, 5*(2), 99-112. https://doi.org/10.2166/hydro.2003.0008

Stone, B. M., & Shen, H. T. (2002). Hydraulic resistance of flow in channels with cylindrical roughness. *Journal of hydraulic engineering*, *128*(5), 500-506. https://doi.org/10.1061/(ASCE)0733-9429(2002)128:5(500)

Story, M., & Congalton, R. G. (1986). Accuracy assessment: a user's perspective. *Photogrammetric Engineering and remote sensing*, *52*(3), 397-399.

Straatsma, M. W., & Baptist, M. J. (2008). Floodplain roughness parameterisation using airborne laser scanning and spectral remote sensing. *Remote Sensing of Environment*, *112*(3), 1062-1080. https://doi.org/10.1016/j.rse.2007.07.012

Straatsma, M. W., & Middelkoop, H. (2006). Airborne laser scanning as a tool for lowland floodplain vegetation monitoring. *Hydrobiologia*, *565*(1), 87-103. https://doi.org/10.1007/s10750-005-1907-5

Straatsma, M. W., Warmink, J. J., & Middelkoop, H. (2008). Two novel methods for field measurements of hydrodynamic density of floodplain vegetation using terrestrial laser scanning and digital parallel photography. *International Journal of Remote Sensing,* *29*(5), 1595-1617. https://doi.org/10.1080/01431160701736455

Tauro, F., Porfiri, M., & Grimaldi, S. (2016). Surface flow measurements from drones. *Journal of Hydrology*, *540*, 240-245. https://doi.org/10.1016/j.jhydrol.2016.06.012

TDOT GREEN. (2020). Product website and spec sheet of TDOT GREEN. Retrieved from https://amuse-oneself.com/en/service/tdotgreen

Toda, Y., Ikeda, S., Kumagai, K., & Asano, T. (2005). Effects of flood flow on flood plain soil and riparian vegetation in a gravel river. *Journal of Hydraulic Engineering,* *131*, 950-960. https://doi.org/10.1061/(ASCE)0733-9429(2005)131:11(950)

Ushijima, S., & Nezu, I. (2002). Computational method for free-surface flows on collocated grid with moving curvilinear coordinates. *Doboku Gakkai Ronbunshu,* *698*, 11-19 (in Japanese with English abstract). https://doi.org/10.2208/jscej.2002.698_11

Watanabe, S., Maeno, S., Shirai, H., & Fujiwara, M. (2006). Expansion mechanism of Salicaceous species and its management technique in the Asahi River. *Doboku Gakkai Ronbunshuu, B,* *62*(3), 238-250. https://doi.org/10.2208/jscejb.62.238

Wei, K., Ouyang, C., Duan, H., Li, Y., Chen, M., Ma, J., ... & Zhou, S. (2020). Reflections on the catastrophic 2020 Yangtze River Basin flooding in southern China. *The Innovation,* *1*(2), 100038. https://doi.org/10.1016/j.xinn.2020.100038

Westaway, R. M., Lane, S. N., & Hicks, D. M. (2000). The development of an automated correction procedure for digital photogrammetry for the study of wide, shallow, gravel-bed rivers. *Earth Surface Processes and Landforms: The Journal of the British Geomorphological Research Group*, *25*(2), 209-226. https://doi.org/10.1002/(SICI)1096-9837(200002)25:2<209::AID-ESP84>3.0.CO;2-Z

Wieser, M., Hollaus, M., Mandlburger, G., Glira, P., Pfeifer, N. (2016). ULS LiDAR supported analyses of laser beam penetration from different ALS systems into vegetation. *ISPRS Annals of Photogrammetry, Remote Sensing & Spatial Information Sciences 3*(3). https://doi.org/10.5194/isprsannals-III-3-233-2016

Wilson, C. A. M. E., Yagci, O., Rauch, H. P., & Olsen, N. R. B. (2006). 3-D numerical modelling of a willow vegetated river/floodplain system. *Journal of Hydrology, 327*(1-2), 13-21. https://doi.org/10.1016/j.jhydrol.2005.11.027

Wu, F. C., Shen, H. W., & Chou, Y. J. (1999). Variation of roughness coefficients for unsubmerged and submerged vegetation. *Journal of hydraulic Engineering, 125*(9), 934-942. https://doi.org/10.1061/(ASCE)0733-9429(1999)125:9(934)

Yakhot V., Orszag S. A., Thangam S., Gatski T. B., & Speziale C. G. (1992). Development of turbulence models for shear flows by a double expansion technique. *Physics of Fluids A: Fluid Dynamics,* *4*(7), 1510-1520. https://doi.org/10.1063/1.858424

Yoshida, K., Maeno, S. (2014). Inverse estimation of distributed roughness coefficients in vegetated flooded rivers, *Journal of Hydraulic Research, 52*(6), 811–823. https://doi.org/10.1080/00221686.2014.932854

Yoshida, K., Maeno, S., Mano, K., Iwaki, T., Ogawa, S., and Akoh, R. (2017). Determination method for vegetation species distribution in rivers using airborne laser bathymetry. *Journal Japan Society of Civil Engineers, Ser. A2 (Applied Mechanics), 73 (2)*, I_607-I_618 (in Japanese with English abstract). https://doi.org/10.2208/jscejam.73.I_607

Yoshida, K., Maeno, S., Ogawa, S., Iseki, S., & Akoh, R. (2018). Estimation of Vegetation Density of Trees Using ALB Point Cloud Data. *Journal of Japan Society of Civil Engineers, Ser. B1 (Hydraulic Engineering)*, *74*(4), I_547-I_552 (in Japanese with English abstract). https://doi.org/10.2208/jscejhe.74.I_547

Yoshida, K., Maeno, S., Ogawa, S., Mano, K., & Nigo, S. (2020a). Estimation of distributed flow resistance in vegetated rivers using airborne topo-bathymetric LiDAR and its application to risk management tasks for Asahi River flooding. *Journal of Flood Risk Management, 13*(1), e12584. https://doi.org/10.1111/jfr3.12584

Yoshida, K., Nagata, K., Maeno, S., Mano, K., Nigo, S., Nishiyama, S., & Islam, M. T. (2021). Flood risk assessment in vegetated lower Asahi River of Okayama Prefecture in Japan using airborne topo-bathymetric LiDAR and depth-averaged flow model. *Journal of Hydro-environment Research*, *39*, 39-59. https://doi.org/10.1016/j.jher.2021.06.005

Yoshida, K., Nigo, S., Maeno, S., & Mano, K. (2020b). Verification of STIV analysis of flood discharge at Nakano Observatory in the Ota River by flow analysis using ALB data. In *22nd Congress of the International Association for Hydro-*

Environment Engineering and Research – Asia Pacific Division: Creating Resilience to Water-Related Challenges, IAHR-APD 2020.

Zhu, L., Subas, C., Tachibana, K., & Shimamura, H. (2015). Methodology development on full-waveform aerial LiDAR data analysis. *Journal of the Japan Society of Photogrammetry and Remote Sensing, 54*(1), 4-19 (in Japanese with English abstract). https://doi.org/10.4287/jsprs.54.44